Quantifying Biophysical Heterogeneity by Single Cell Microfluidic Impedance Cytometry

---

A

Dissertation

Presented to

the faculty of the School of Engineering and Applied Science

University of Virginia

---

in partial fulfillment

of the requirements for the degree

Doctor of Philosophy

by

Armita Salahi

May 2022

APPROVAL SHEET

This

Dissertation

is submitted in partial fulfillment of the requirements
for the degree of

Doctor of Philosophy

Author: Armita Salahi

Advisor: Nathan Swami

Advisor:

Committee Member: Gustavo Kunde Rohde

Committee Member: Todd W. Bauer

Committee Member: Mohammad Fallahi-Sichani

Committee Member: Federica Caselli

Committee Member:

Committee Member:

Accepted for the School of Engineering and Applied Science:

Jennifer L. West, School of Engineering and Applied Science

May 2022

To my lovely husband, Ali

for his endless support

Acknowledgment

First, I would like to give my sincere appreciation to my adviser, Dr. Nathan Swami. I want to thank him for his patience, insights, guidance, and for encouraging my research and allowing me to grow as a research scientist throughout the last few years. I could not have imagined this accomplishment without his tremendous support.

My sincere thanks go to the members of my dissertation committee: Dr. Gustavo Kunde Rohde, Dr. Todd W. Bauer, Dr. Mohammad Fallahi-Sichani, and Dr. Federica Caselli for their thoughtful comments toward improving my work.

I owe many thanks to the current and former members of my research group who shared their knowledge with me and without their help, none of this work would have been possible: Dr. Carlos Honrado, Dr. John Moore, Aditya Rane, XuHai Huang, Karina Torres, Dr. Ali Rohani, Dr. Walter Varhue, Dr. John McGrath, and Dr. Vahid Farmehini and anyone else whom I did not mention.

I also want to thank the members of the Bauer lab and the Jin lab who helped me with various aspects of my research during my Ph.D.

I cherish this opportunity to thank the dearest people in my life, without whom I wouldn't be here today. First, I would like to express my sincere thanks and love to my mom and dad, who were always there for me when I needed them. And last but not least, my lovely husband, Ali, who always has faith in me and encourages me to reach my dreams.

Abstract

Heterogeneity in biophysical properties, which is inherent to the functional and structural organization of biosystems, presents challenges to cell biologists and clinicians seeking to associate biological function and disease with particular markers. Current methods to quantify heterogeneity focus on biochemical properties, as quantified by single-cell flow cytometry after fluorescent staining for their characteristic cell surface proteins or by label-free Raman spectral methods. Cellular biophysical metrics, on the other hand, have often been restricted to size-based differences that do not provide sufficient functional information on the biosystem. Frequency-resolved impedance cytometry in microfluidic systems is emerging as a tool for multiparametric and high-throughput biophysical stratification of phenotypes in a label-free manner. However, there is a need to standardize the metrics for enabling facile recognition and automated fitting to quantify subpopulations in heterogeneous biological samples. This will be explored per the following aims.

Chapter 1: Modified red blood cells as model particles with modulated electrophysiology:

The application of red blood cells (RBCs) as multimodal standardized particles with systematically modulated subcellular electrophysiology and fluorescence is presented in this chapter. Different modified RBC types were identified at single-cell sensitivity based on phenomenological impedance metrics and fitted to single-shell dielectric models to compute biophysical information. In this manner, single-cell impedance data from unknown RBC types can be mapped versus modeled RBC types for facile determination of subcellular biophysical information.

Chapter 2: Machine learning based methods for automating quantification of subpopulations:

Using drug-treated pancreatic cancer cells from tumor xenografts of differing gemcitabine sensitivity, we identified biophysical metrics from single-cell impedance cytometry to quantify subpopulations at the early apoptotic versus late apoptotic and necrotic states, by using machine learning to train for recognition of each phenotype. Such automated biophysical classification to follow the progression of apoptotic phenotypes can be used to modulate cancer cell death and advance longitudinal analysis to discern drug-resistant phenotypes.

Chapter 3: Supervised learning to distinguish drug-induced transformations of pancreatic cancer cells versus the associated fibroblasts in the tumor microenvironment

In this chapter we develop a novel supervised machine learning (ML) approach that utilizes the multiple impedance metrics obtained from single-cell cytometry conducted at several simultaneously applied frequencies to distinguish the biophysical properties of co-cultured viable cancer cells and CAFs, in absence and in presence of drug treatment. By employing supervised ML and the measured impendence data, we build models to classify the drug resistant subpopulation within longitudinal studies and isolate them for downstream molecular analysis.

Table of Contents

Introduction

Impedance cytometry

Cellular systems exhibit heterogeneity following treatment. Single-cell analysis tools are needed to measure these changes, in order to catch subpopulations that may not be captured by bulk measurement of proteins or nucleic acids commonly used for characterization. Commercial methods for single cell analysis are typically limited to flow cytometry, which uses lasers to excite fluorophores that have been tagged to the protein or nucleic acid of interest. However, characterization of internal structures requires membrane permeabilization and fixation (killing the cell), and antibody binding to surface receptor proteins typically used in characterization can cause cell signaling that biases fate potential. This becomes especially important if cells are to be kept alive and to be used for transplant or downstream analysis.

In order to address these challenges, we use impedance cytometry. In impedance cytometry, electrical properties of each cell are measured under AC fields at several superimposed frequencies, as a high throughput tool (300-500 cells/s) for single-cell analysis of electrophysiology phenotypes (**Figure 1.1**).

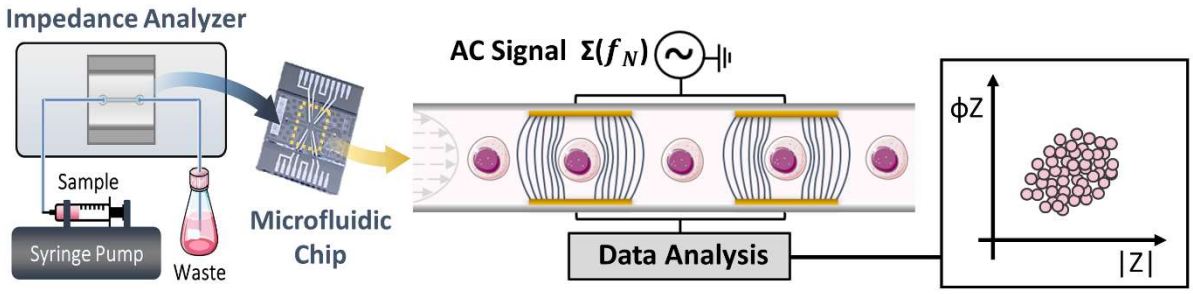

Figure 1.1: *Schematics of impedance cytometer device*

Impedance cytometry measures the field screening property of each passing cell based on the amount of blocked current (denoted as impedance magnitude: |Z|) and its time delay due to reactive components (denoted as impedance phase: ϕZ). These signals can be used to probe different biophysical characteristics of the cell depending on the applied frequency, with determine cell volume or electrical diameter dominating in the 0.1-1 MHz range, membrane capacitance dominating in the 1-10 MHz range, and interior conductivity dominating in the 10-50 MHz range (**Figure 1.2**). At low frequencies (sub-MHz), the applied electrical field is screened around the cell and the impedance signal we receive is based volume. At higher frequencies, the membrane

becomes polarized, so there is more electrical field penetrating the membrane causing its impedance to drop. At high frequencies, the membrane has been short circuited, the capacitor is now open, allowing the field to penetrate to the interior of the cell and obtain information regarding cytoplasm conductivity and interior complexity. By applying several frequencies simultaneously and measuring the resulting impedance signal, we are able to identify, characterize and separate cells, based on their subcellular biophysical properties, without the use of labels.

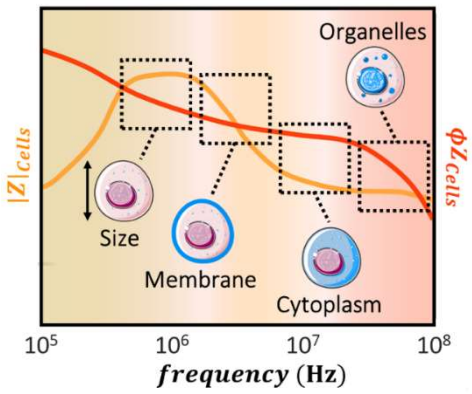

Figure 1.2: *Frequency ranges at which different parts of the cell are probed with impedance cytometry*

Shell modelling for biological particles

For the case with particles suspended in a dielectric medium, dielectric spectroscopy can be used to measure the dielectric properties of the suspension [1]. This mixture of particle and medium can be approximated to that of a single dispersion using Maxwell's mixture theory (MMT) [2]. MMT can be used to combine the dielectric properties of all parts into an overall complex permittivity of the mixture ($\tilde{\varepsilon}_{mix}$). For the case of a cell in suspending medium, MMT-based, multi-shell models can be used to retrieve the dielectric properties of the cell [3-5]. While most cells have an intricate internal structure, surrounded by a membrane, a simpler approximation can be used where a single-shell model is applicable (**Figure 1.3**). In this model, there are two dispersions, corresponding to each of the existing interfaces (medium-membrane and membrane-interior).

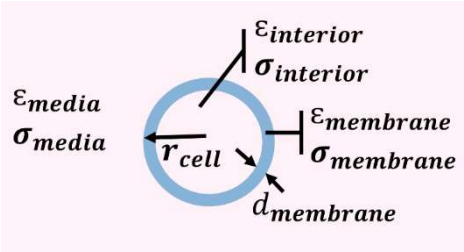

***Figure 1.3**: Representation of an equivalent single shell model for RBCs in a suspending medium*

For spherical particles dispersed in a suspending medium with a volume fraction φ (volume ratio of the cell volume to the detection volume), the complex impedance of the mixture is:

$$\tilde{\varepsilon}_{mix} = \tilde{\varepsilon}_{med}\left(\frac{1+2\,\varphi\,\tilde{f}_{CM}}{1-\varphi\,\tilde{f}_{CM}}\right) \quad (1)$$

Where $\tilde{\varepsilon}_{med}$ is the complex permittivity of medium and $\tilde{\varepsilon}$ is the general complex permittivity is given by:

$$\tilde{\varepsilon} = \varepsilon_0\varepsilon - j\frac{\sigma}{\omega} \quad (2)$$

With ε the permittivity, ε_0 is the constant vacuum permittivity (8.85×10^{-12} F m^{-1}), σ the conductivity, $j^2 = -1$, and ω the angular frequency along the frequency spectrum measured. For a single-shell model, the Clausius−Mossotti factor ($\tilde{f}_{CM}$) of the cell in the mixture is given by:

$$\tilde{f}_{CM} = \frac{\tilde{\varepsilon}_{cell} - \tilde{\varepsilon}_{med}}{\tilde{\varepsilon}_{cell} + 2\tilde{\varepsilon}_{med}} \quad (3)$$

The complex permittivity of the cell, $\tilde{\varepsilon}_{cell}$, in a single shell model can be calculated as:

$$\tilde{\varepsilon}_{cell} = \tilde{\varepsilon}_{membrane}\,\frac{\gamma^3 + 2\left(\frac{\tilde{\varepsilon}_{interior} - \tilde{\varepsilon}_{membrane}}{\tilde{\varepsilon}_{interior} + 2\tilde{\varepsilon}_{membrane}}\right)}{\gamma^3 - \left(\frac{\tilde{\varepsilon}_{interior} - \tilde{\varepsilon}_{membrane}}{\tilde{\varepsilon}_{interior} + 2\tilde{\varepsilon}_{membrane}}\right)} \quad (4)$$

With,

$$\gamma = \frac{r_{cell}}{r_{cell} - d_{membrane}} \quad (5)$$

Where r_{cell} is the radius of the cell and $d_{membrane}$ is the thickness of the cell membrane. With the calculation of the complex permittivity of the mixture ($\tilde{\varepsilon}_{mix}$), it is then possible to arrive at the impedance of the mixture ($\tilde{Z}_{mix}$):

$$\tilde{Z}_{mix} = \frac{1}{j\omega\,\tilde{\varepsilon}_{mix}\,G} \quad (6)$$

Here G is the geometric constant of the system, and it depends on the dimensions of the measurement volume, including electrode width and spacing [6]. Since the electric field is nonuniform, G cannot be determined precisely.

The impedance of a cell is determined from the differential current (I_{diff}) as it passes between the measurement electrode pair. This current is related to the impedance of the mixture (cell plus medium) [6]:

$$I_{diff} = \frac{V_{appl}\,\tilde{S}(\omega)}{\tilde{Z}_{med}} - \frac{V_{appl}\,\tilde{S}(\omega)}{\tilde{Z}_{mix}} = j\omega G\, V_{appl}\,\tilde{S}(\omega)(\tilde{\varepsilon}_{med} - \tilde{\varepsilon}_{mix}) \quad (7)$$

Where V_{appl} is the applied voltage, S̃(ω) is complex transfer function, $\tilde{Z}_{med}$ and $\tilde{Z}_{mix}$ denote the impedances associated with medium-filled channel and channel with a suspended cell, respectively.

Since experimental impedance data was normalized against the polystyrene beads, differential current for a bead is also computed based on eqs.7 So, the normalized current is given by:

$$\frac{I_{diff(Cell)}}{I_{diff(Bead)}} = \frac{j\omega G\, V_{appl}\,\tilde{S}(\omega)(\tilde{\varepsilon}_{med} - \tilde{\varepsilon}_{mix(Cell)})}{j\omega G\, V_{appl}\,\tilde{S}(\omega)(\tilde{\varepsilon}_{med} - \tilde{\varepsilon}_{mix(Bead)})} = \frac{\tilde{\varepsilon}_{med} - \tilde{\varepsilon}_{mix(Cell)}}{\tilde{\varepsilon}_{med} - \tilde{\varepsilon}_{mix(Bead)}} \quad (8)$$

Substituting eqs.1 in eqs.8:

$$\frac{I_{diff(Cell)}}{I_{diff(Bead)}} = \frac{\tilde{\varepsilon}_{med}\,(1 - \frac{1+2\,\varphi_{Cell}\,\tilde{f}_{CM(Cell)}}{1-\varphi_{Cell}\,\tilde{f}_{CM(Cell)}})}{\tilde{\varepsilon}_{med}\,(1 - \frac{1+2\,\varphi_{Bead}\,\tilde{f}_{CM(Bead)}}{1-\varphi_{Bead}\,\tilde{f}_{CM(Bead)}})} = \frac{\varphi_{Cell}\,\tilde{f}_{CM(Cell)}\,(1 - \varphi_{Bead}\,\tilde{f}_{CM(Bead)})}{\varphi_{Bead}\,\tilde{f}_{CM(Bead)}\,(1 - \varphi_{Cell}\,\tilde{f}_{CM(Cell)})} \quad (9)$$

Eqs.9 for small volume fraction ($\varphi < 0.01$) simplifies to [6]:

$$\frac{I_{diff(Cell)}}{I_{diff(Bead)}} = \frac{\varphi_{Cell}\,\tilde{f}_{CM(Cell)}}{\varphi_{Bead}\,\tilde{f}_{CM(Bead)}} \quad (10)$$

Assuming the cell is spherical:

$$\frac{I_{diff(Cell)}}{I_{diff(Bead)}} = \frac{\tilde{f}_{CM(Cell)}}{\tilde{f}_{CM(Bead)}}\left(\frac{r_{Cell}}{r_{Bead}}\right)^3 \quad (11)$$

The Real and Imaginary parts of the eqs.11 are calculated, and respectively their corresponding relaxation curves are generated. The optimal fit between Real and Imaginary parts of the experimental and the model-derived spectra can be found by using a pattern search function. The algorithm uses a starting point vector, containing the starting values for each parameter, plus two boundary vectors, defining the maximum and minimum values for each parameter, to generate iterations of dielectrophoretic spectra. The optimal fit is determined by finding which parameters generate a modelled-derived spectrum that has the minimal difference between experimental data

and model. The fitting process ended when the local difference between the data and model was smaller than a predefined tolerance value, with an R^2 value evaluating the goodness of fit.

The estimated properties are used to calculate the membrane capacitance ($C_{membrane}$) using:

$$C_{membrane} = \frac{\tilde{\varepsilon}_{membrane}}{d_{membrane}} \quad (12)$$

Machine learning

Traditionally impedance cytometry data analysis is based on a manual gating approach. However, this process becomes tedious and can lead to user-related variations. Also, manual gating is almost impossible for heterogeneous samples. In these samples, due to the multi-dimensional (multi-feature) nature of data, it is not possible for the individuals to gate and separate the various cell groups from each other. However, machine learning seems to be a great tool to solve these problems and improve the impedance cytometry data analysis.

Machine learning (ML) is the study of algorithms that enable systems to learn and improve from experience (existing data) without being explicitly programmed. These algorithms find the relationships within the datasets and use them to make predictions about the new and unseen data points. Supervised and unsupervised learning are two approaches in ML, each aiming to solve different problems.

In supervised learning, we provide the labeled data sets (input-output pairs) and the model learns the relationships between inputs and outputs by minimizing the prediction error by comparing the predictions and the given labels. Classification (prediction of categorical variables) and regression (prediction of continuous variables) are two main categories of supervised learning. Examples of supervised learning models: Decision Tree, Support Vector Machines (SVM), K-Nearest Neighbor (KNN), and Naive Bayes.

In contrast, in unsupervised learning, we do not have labels. In these problems, the models aim to find structure and hidden patterns in the data without human intervention. Unsupervised learning models are utilized for three main tasks: clustering, association, and dimensionality reduction. Examples of unsupervised learning models: K-Means Clustering, Gaussian Mixture Models (GMMs), and Principal Component Analysis (PCA).

Dielectrophoresis

Dielectrophoresis (DEP) is another microfluidic technique that can characterize and separate cells based on their electrophysiology phenotype. DEP is the translation of polarized cells within a spatially non-uniform electric field [7-9]. If a cell is more polarizable than its surrounding medium, it will be attracted to the higher field regions (positive DEP or pDEP), and if it is less polarizable than the suspending medium, it will be pushed away from high filed points (negative DEP or nDEP). **Figure 1.4** depicts a typical biological particle DEP spectrum. At low frequencies (sub 100kHz), the cell membrane shields the electric field, so the particle becomes less polarizable than the medium, and consequently, it experiences negative DEP (nDEP). As the frequency increases, the membrane starts to polarize and as a result, the particle starts to experience positive DEP (pDEP). There is a certain frequency that has practical importance. The crossover frequency at which negative DEP transitions to positive DEP is essential for performing separations between two cell types in microfluidic systems, as they move in different directions. The cytoplasm conductivity dominates the DEP response at higher frequencies (1 MHz). In the DEP spectrum, another crossover frequency is evident that happens at much higher frequencies. However, this frequency usually does not have practical importance since most commercial AC generators are not able to achieve enough power to stimulate cells close to their second crossover frequency.

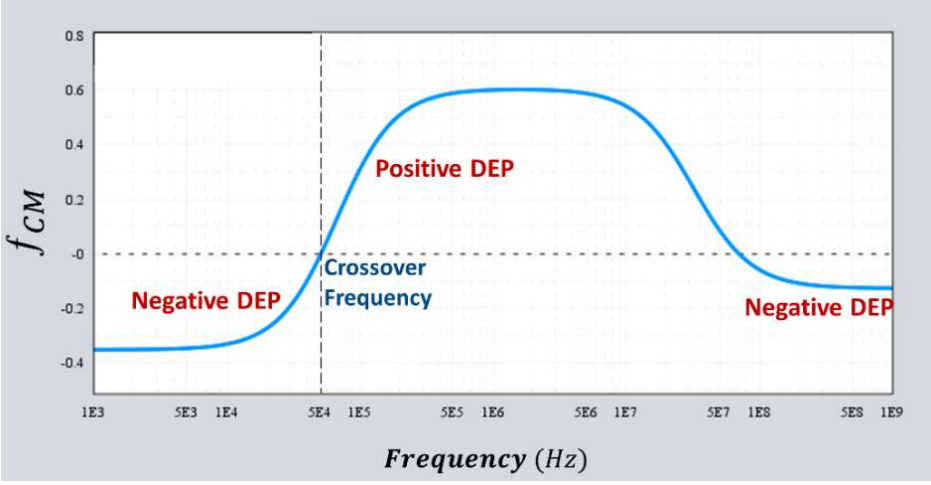

***Figure 1.4**: Example DEP spectrum for a biological particle*

DEP force on a particle defines by the following equation (**Figure 1.5**). The level and direction of DEP force is dependent on the media permittivity, the particle size, its polarizability relative to the media, and the non-linear electric field gradient.

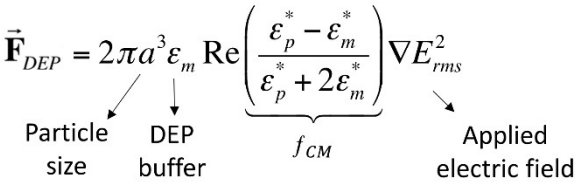

Figure 1.5*: Equation for dielectrophoretic force*

Chapter 1: Modified red blood cells as model particles with modulated electrophysiology

Biophysical cellular information at single-cell sensitivity is becoming increasingly important within analytical and separation platforms that associate cell phenotype with markers of disease, infection, and immunity. Frequency-modulated electrically driven microfluidic measurement and separation systems offer the ability to sensitively identify single cells based on biophysical information, such as their size and shape, as well as their subcellular membrane morphology and cytoplasmic organization. However, there is a lack of reliable and reproducible model particles with well-tuned subcellular electrical phenotypes that can be used as standards to benchmark the electrophysiology of unknown cell types or to benchmark dielectrophoretic separation metrics of novel device strategies. Herein, the application of red blood cells (RBCs) as multimodal standardized particles with systematically modulated subcellular electrophysiology and fluorescence is presented. Using glutaraldehyde fixation to vary membrane capacitance and by membrane resealing after electrolyte penetration from the media to vary interior cytoplasmic conductivity and fluorescence, each modified RBC type can be identified at single-cell sensitivity based on phenomenological impedance metrics and fitted to single-shell dielectric models to compute biophysical information. In this manner, single-cell impedance data from unknown RBC types can be mapped versus these model RBC types for facile determination of subcellular biophysical information and their dielectrophoretic separation conditions, without the need for time-consuming algorithms that often require unknown fitting parameters. Such internal standards for biophysical cytometry can advance in-line phenotypic recognition strategies.

Introduction

The phenotypic heterogeneity displayed by cellular systems [10] has motivated the need for robust platforms for single-cell analysis and separation [11], to enable disease diagnostics based on cellular markers [12] and to control cellular compositions for transplant applications. While fluorescently stained cell surface markers that provide identifying biochemical information on each cell type are widely adopted for this purpose [13], there is an increasing recognition that complementary biophysical information is essential to identify subpopulations associated with key functions [14]. Specifically, methods for reliable multiparametric biophysical identification of cellular subpopulations, without the need to label or lyse them, can enable longitudinal temporal studies that are often not possible using fluorescently stained surface markers. Microfluidic single-cell electrical measurements by impedance-based flow cytometry [15, 16], and electrically driven separations by dielectrophoresis [17] (DEP) are able to sensitively quantify the cellular biophysical information at high sample throughput (300−500 cells/s) and utilize this through frequency-modulation to distinguish cellular subpopulations. While impedance magnitude at low frequencies (<0.5 MHz) provides highly sensitive size information on each measured cell, the polarization of cell membrane at successively higher frequencies (1−10 MHz) provides information on membrane capacitance, and polarization of the interior at even higher frequencies (>10 MHz) can provide valuable information on cytoplasmic contents [18], including the nucleus size [19]. In this manner, impedance cytometry has been used to quantify subpopulations from heterogeneous samples, including infected red blood cells [20], activation of various leukocyte subtypes [21, 22], tumorigenicity of pancreatic cancer cell types [23], drug sensitivity of cancer cells [24], bacterial germination from spores [25], apoptotic bodies generated by drug-sensitive cancer cells [26], and to monitor the cell density of spheroids [27]. Also, dielectrophoresis has been applied to isolate cells of a particular phenotype from heterogeneous samples [28], including circulating tumor cells [29, 30], stem cell progenitors [31], cells based on mitochondrial phenotype [32], bacterial strain discrimination [33, 34], and isolate secreted exosomes [35, 36]. However, while standard particles with known signal characteristics are used in flow cytometry and fluorescently activated cell sorting for benchmarking each measured cell and to trigger sorting, similar tools are lacking for dielectrophoresis and impedance cytometry.

Currently, in impedance cytometry, polystyrene beads of well-controlled sizes are used to benchmark the impedance magnitude at low frequencies (<0.5 MHz) for enabling accurate determination of cell size [37]. However, such plastic beads bear little resemblance to living cells that possess a high capacitance plasma membrane of varying composition and morphology, and a conductive interior that reflects the cytoplasmic organization. Hence, polystyrene beads that are opaque to the electric field at higher frequencies cannot be used for benchmarking of cell membrane capacitance and cytoplasmic conductivity. On the other hand, yeast cells are often used to validate novel cytometry [38] and separation platforms [39], but they are not well-suited to function as standard particles due to their wide range of size and shape distributions. Standardized coflowing particles of well-tuned subcellular phenotypes can enable benchmarking of electrical physiology (henceforth, electrophysiology) of unknown cell types during impedance cytometry and provide systems with a well-defined DEP frequency response for facile assessment of separation metrics (collection efficiency and separation purity) within novel microfluidic device designs. To address this vision, in chip chapter we explore the modification of red blood cells (RBCs) to create standard particles with modulated subcellular properties (i.e., membrane capacitance and interior cytoplasmic conductivity), that can also be identified by their fluorescence level.

RBCs or erythrocytes are the predominant cell type in blood [40], with the function of carrying oxygen to tissues and carbon dioxide away from tissues. Their functional outcomes are strongly linked to their biophysical properties, such as the relationship of cellular dielectric properties to oxygen carrying capacity [41], glucose homeostasis [42], and age [43, 44] or that of their cellular biomechanical properties to oxygen transport [45], infection [46] and disease [47]. Hence, their modification to create standardized coflowing particles during impedance cytometry or dielectrophoretic separation can lead to facile stratification of subcellular electrophysiology of disease-modified RBC phenotypes.

The availability of coflowing standard particles for impedance cytometry and dielectrophoresis can enable accurate comparison of data sets across sample types, device platforms and machine learning assisted phenotypic recognition models, leading to a more holistic workflow for biophysical phenotyping [48]. In the field of biomechanical cytometry, for instance, wide divergences in the measured cell stiffness on identical cells by different techniques [49] led to an interest in reference particles with well-characterized mechanical properties to calibrate the

elastic modulus of cells across cytometry platforms [50]. Analogously, we explore methods to modulate the RBC membrane capacitance by altering glutaraldehyde fixation to create fixed RBCs and to modulate cytoplasmic conductivity by penetrating RBCs with buffers of varying conductivity and fluorescence [51] prior to membrane resealing to create ghost RBCs. While prior work has reported on creating fixed [52] and ghost RBCs [6], our innovation is the systematic modulation of the subcellular electrical physiology, as validated by impedance metrics from single-cell cytometry, and the generation of multimodal standard particles for coupling fluorescence based identification to cell distinction based on cytoplasmic conductivity. To enable their application as standard coflowing particles in impedance cytometry and dielectrophoretic separation devices, we illustrate how single-cell impedance data from unknown cell types can be compared to those from a progression of modified RBC types with known subcellular physiology. As a result, the DEP crossover frequency and relative dielectric property differences for unknown cell types can be determined, without the need for time-consuming algorithms that often require unknown fitting parameters and off-line computation. In this manner, we seek to advance the vision of internal standards for biophysical cytometry and for in-line phenotypic recognition [53].

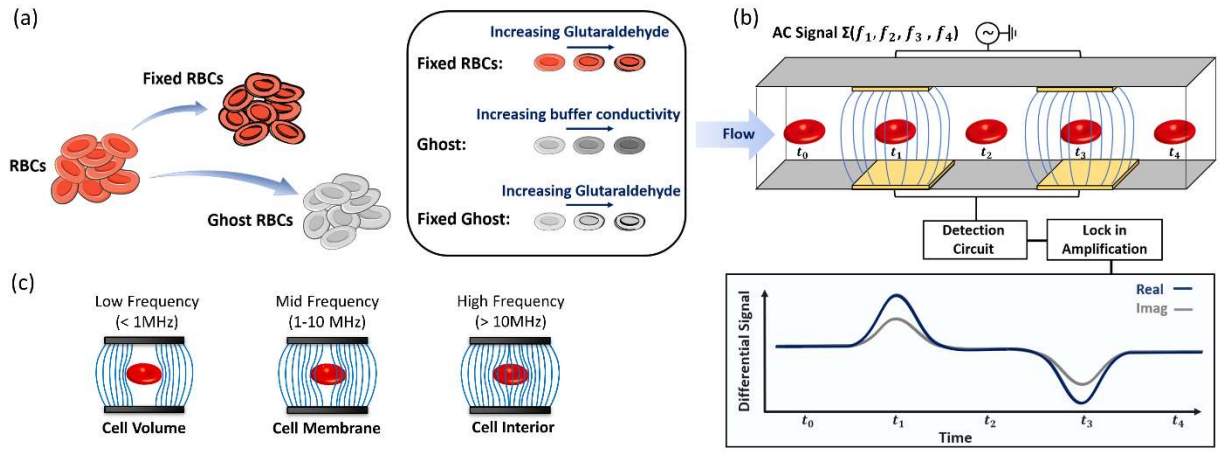

Figure 2.1: *Schematic of (a) RBC modification to prepare fixed, ghost, and fixed ghost RBCs and (b) their impedance detection. RBCs in 1× PBS flow through a microchannel with two sets of facing top-bottom detection electrodes. AC signals are applied at simultaneously differing frequencies to the top electrodes and the respective differential current at the bottom electrodes is used to determine single-cell impedance signals. (c) Depending on frequency of the applied AC signal, cellular biophysical properties corresponding to different cell components interacting with the AC field can be measured.*

Materials and Methods

RBC Sample Preparation

Human red blood cells (RBCs) from multiple batches of blood type A+ (Valley Biomedical, Winchester, VA) were suspended in RPMI 1640 HEPES (Sigma-Aldrich, St. Louis, MO) after supplementing with 0.5% Albumax II Lipid-Rich BSA (Sigma) and 50 mg/L hypoxanthine (Thermo Fisher Scientific) for storage and dilution, as needed (1.13×10^8 cells/mL). The control sample of unmodified healthy RBCs was prepared by washing diluted RBCs in 1× PBS, three times. The fixed RBC samples were prepared by washing diluted unmodified RBCs in 1× PBS, three times, and resuspending the packed cells in 1 mL of 1× PBS, mixed with 0.01%, 0.1%, or 1% glutaraldehyde (Sigma), followed by incubation at room temperature for an hour. Samples were then centrifuged at 400 g for 5 min, and the cell pellet was resuspended in 1 mL of 1× PBS for measurement. For preparing ghost RBCs, the diluted unmodified RBCs were washed three times in 1× PBS. Then, one volume of packed RBC was incubated with 4 volumes of hypotonic buffer, composed of 0.1× PBS in the fridge at 4 °C for 30 min to obtain RBC ghosts. The ghost cells were centrifuged at 1400 g for 10 min and washed three times with 0.1× PBS, until the supernatant was colorless, with a light pink cell pellet [54]. The ghost RBCs were then resuspended in different buffers of differing conductivities (1.57, 1.91, and 2.12 S/m), followed by room temperature incubation for 4 h, so that the cell membrane can reseal after the buffer penetration. The samples were centrifuged at 1400 g for 10 min and the cell pellet was resuspended in the respective buffers. After resealing, the ghost RBCs (i.e., filled with respective buffer) were fixed with 0.1% glutaraldehyde, by incubation in their respective buffer at room temperature for 1 h. After centrifuging at 1400 g for 10 min, the cell pellet was resuspended in 1× PBS (1.57 S/m). For fixed ghost samples, the resealed ghost RBCs were fixed with glutaraldehyde, by incubation at room temperature for an hour. Then, the cell pellet after centrifuging at 1400 g for 10 min was resuspended in 1× PBS (1.57 S/m) for analysis.

Impedance Cytometry

For impedance cytometry, cells were measured in 1x PBS buffer after dilution to $\sim 2 \times 10^5$ cells/mL, with coflowing 10 μm sized polystyrene beads (Sigma) at $\sim 1.2 \times 10^5$ beads/mL. A syringe pump was used to introduce the respective sample into a microfluidic chip (fabrication per

prior report [14]) with a detection region 30 μm (width) × 30 μm (height) and the measurement was carried out using an impedance analyzer (Amphasys AG, Switzerland), per **Figure 2.1**. Four simultaneous frequencies were used: 0.5, 2, and 30 MHz, and a probe frequency that is swept in the 2 to 20 MHz range. Acquisition settings were optimized for signal-to-noise based on levels of signal modulation, amplification, and demodulation of the trigger voltage level. Processed signal data were stored as impedance magnitude and phase, exported as CSV files, and processed with custom code written in Python.

Impedance Data Processing and Statistical Analysis

The impedance phase and magnitude for RBCs were normalized based on division to those obtained for polystyrene beads to account for any temporal variations during the measurement and to enable quantitative comparison between different populations and/ or experiments. The analysis of experimental data starts by plotting the phase ($\phi Z_{30\ MHz}$) versus the magnitude ($|Z|_{30\ MHz}$) in a scatter plot (**Figure 2.2a**). In this example, the two populations, polystyrene beads and red blood cells (RBCs), are clearly identifiable, so that the bead population can be gated. Then the impedance phase and magnitude were normalized against the impedance response of the beads by dividing the impedance data by the mean impedance of beads. After the normalization, beads would have a mean magnitude of 1 and a mean phase of 0 (**Figure 2.2b**). Then in the normalized scatter plot of phase ($\phi Z_{30\ MHz}$)) versus the magnitude ($|Z|_{30\ MHz}$), the RBCs population were gated from reference beads and the normalized impedance for gated RBCs was analyzed at each frequency (0.5-30 MHz). Due to normalization, impedance phase is reported in arbitrary units (with respect to impedance phase of beads indexed at zero).

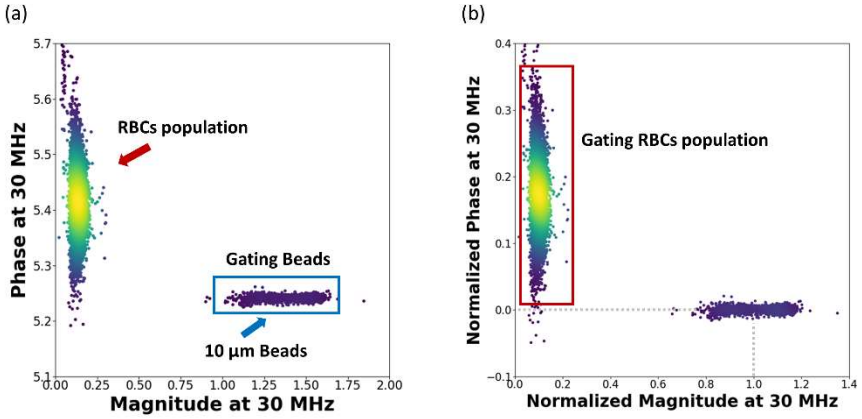

Figure 2.2: *(a) Scatter plot of impedance magnitude versus impedance phase at 30 MHz is used to normalize the data against the 10 μm beads. (b) after normalizing the data, a gate is then generated to include the cells. This gate is used for all the measurements at each prob frequencies.*

All statistical analyses were performed using a custom script in Python. Significance level was defined as $p < 0.05$. Comparisons between any two groups were done using a student's two-tailed t test, while comparisons between multiple groups were performed using a one-way ANOVA with a Tukey's multiple comparisons test. All results are representative of at least three repetitions, with error bars indicating standard deviation between sample triplicates.

Flow Cytometry

Resealing of ghost RBCs was tested with FITC−dextran (Fluorescein isothiocyanate−dextran, Sigma) with an average molecular weight of 40000. Different FITC− dextran concentrations (0.25, 0.5, and 1 mg/mL) were added to the ghost during resealing. The samples were then washed twice in 1× PBS. Following imaging, flow cytometry was performed using a CytoFLEX (Beckman Coulter) and analyzed using CytExpert (Beckman Coulter).

DEP Spectral Measurement

RBCs samples (normal and fixed [1%] RBCs) were centrifuged and resuspended in 8.8% sucrose water, with media conductivity of 400 μS/cm for DEP spectral measurements performed on the 3DEP analyzer (DepTech, Uckfield, U.K.) with a recording interval set to 30 s at 10 Vpp, with data collected over 20 points between 100 kHz and 30 MHz. In this 3DEP reader, the electric field is applied to gold-plated conducting electrode stripes inside the wall of each well, with the DEP response measured at 20 different frequencies applied individually within each well. The relative DEP force at each frequency is obtained by analyzing spatiotemporal variations in light intensity from particle scattering using particular bands in each of the 20 wells, after normalization to the background at zero field (time = 0). The maximum nDEP (negative DEP) force level for each cell line was used as the basis to normalize the measured DEP level for each cell type [32].

RESULTS AND DISCUSSION

Modulating Membrane Capacitance of RBCs

Glutaraldehyde is an agent that cross links proteins in the cell membrane and cytoplasm, which is often utilized to simulate the pathological state of RBCs [55]. Herein, we investigate the effect of the reduced ion mobility due to this treatment, on impedance metrics of single RBCs measured over large event numbers (~10000 per cell type). Presence of the lipid cell membrane typically causes biological cells to behave as insulators at low frequencies (<1 MHz), therefore, allowing for an estimation of cell volume. The electrical diameter is estimated based on the cube root of impedance magnitude at a frequency level of 0.5 MHz, which is just below that required for cell membrane-induced field dispersion: $\sqrt[3]{|Z|_{0.5\ MHz}}$. At increasing frequencies, the cells become increasingly conductive due to capacitive coupling across the membrane, until the stabilization of the electric field dispersion at a cutoff frequency, beyond which the field short-circuits the cell membrane (>10 MHz). Focusing our data analysis on this frequency range, wherein the membrane capacitance is responsible for field dispersion (1−10 MHz), we compute the so-called electrical opacity as the impedance magnitude at each probe frequency versus that at 0.5 MHz: $|Z|_{prob-freq}/|Z|_{0.5\ MHz}$. Since size-controlled insulating polystyrene beads continue to screen the electric field, even at successively higher frequencies, their electrical opacity remains constant at unity. In this manner, the electrical opacity can be used as a size-normalized impedance metric that varies inversely to the membrane capacitance for comparison versus beads of invariant opacity. Based on **Figure 2.3a**, while the respective RBC phenotypes cannot be distinguished solely based on their electrical diameter, due to the wide distributions for each cell type, their respective opacity distributions show systematic differences, especially at frequency levels of 5 MHz and beyond (**Figure 2.3b**; vs insulating beads normalized at unity opacity) The histograms (**Figure 2.3c**) and bar plots (**Figure 2.3d**) for opacity at 5 MHz indicate gradually increasing opacities (i.e., lower membrane capacitance) with fixation level, with significant differences (**Figure 2.3d**).

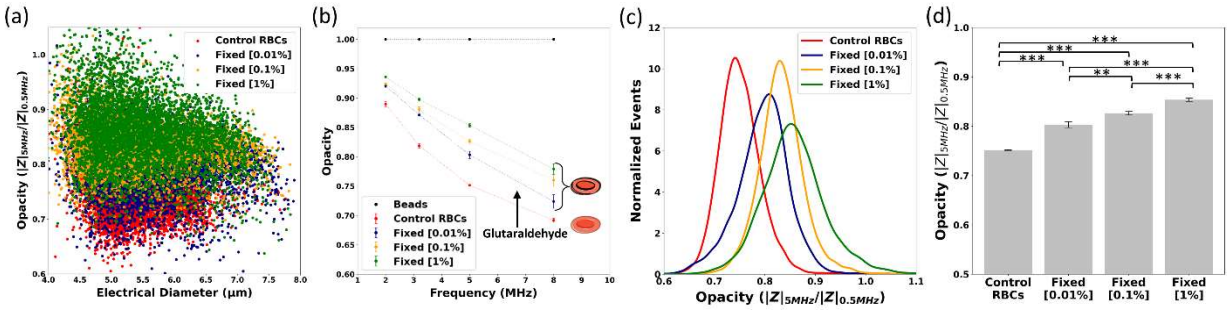

Figure 2.3: *Impedance data for unmodified RBCs (control) and for fixed RBCs, with different levels of glutaraldehyde fixation (0.01%, 0.1%, and 1%) represented as (a) a single-cell event scatter plot of electrical opacity ($|Z|_{5\ MHz}/|Z|_{0.5\ MHz}$) vs electrical diameter ($\sqrt[3]{|Z|_{0.5\ MHz}}$); (b) Frequency response of the electrical opacity in the 2−8 MHz range (points connected by lines to guide the reader); (c) Histogram distributions of electrical opacity ($|Z|_{5\ MHz}/|Z|_{0.5\ MHz}$) (based on 10000 events for each cell type); (d) Bar plot of electrical opacity ($|Z|_{5\ MHz}/|Z|_{0.5\ MHz}$) to indicate significance level of the differences (**p < 0.01 level; ***p < 0.001 level).*

It is noteworthy that based on the impedance metrics at higher frequencies (>10 MHz) that correspond to properties of the cell interior, there are no significant differences for the respective cell types (**Figure 2.4**). This confirms the ability to generate model particles with modulated membrane capacitance, but with minimal differences within the cell interior.

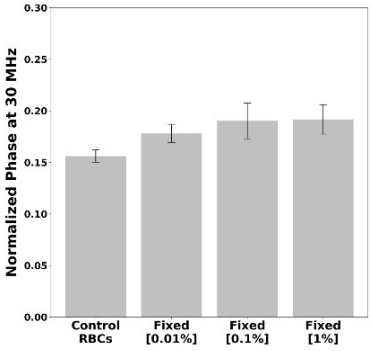

Figure 2.4: *Bar plot of mean phase at 30 MHz (ϕZ 30 MHz) for control RBCs and for fixed RBCs, with different levels of glutaraldehyde (0.01%, 0.1%, and 1%) shows no significant differences between the respective cell types.*

These modified RBCs are reliable model particles for quantifying functionality of novel DEP designs. In our recent work (**Figure 2.5**), the separation metrics of a novel design with a set of sequential field nonuniformities was validated using normal and fixed RBCs [28]. Fixed RBCs of

lower membrane capacitance exhibit higher crossover frequencies versus unmodified RBCs. Hence, by utilizing frequency ranges wherein unmodified RBCs exhibit pDEP (positive DEP or translation toward the high field) and fixed RBCs exhibit nDEP (negative DEP or translation away from the high field), the DEP separation was validated.

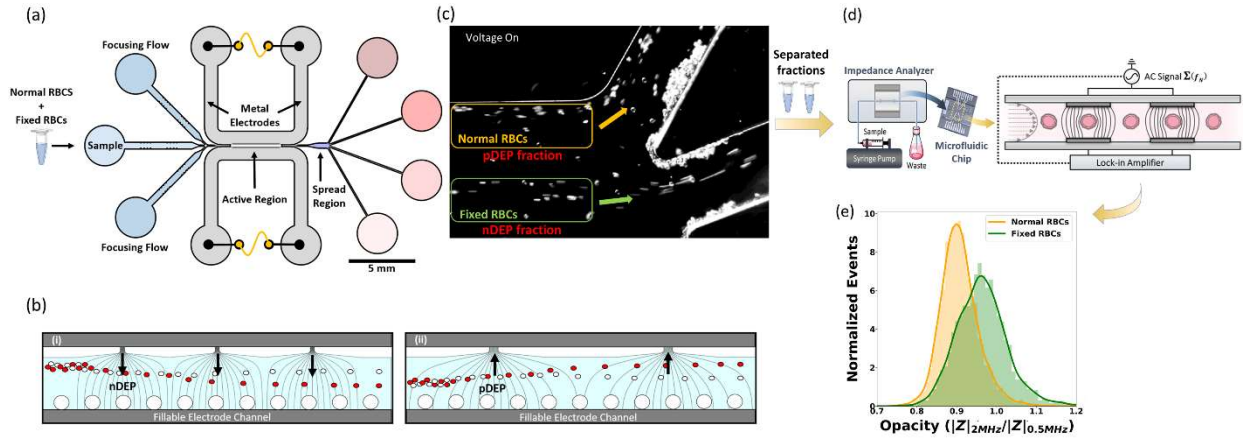

Figure 2.5: *(a) Schematic of microfluidic device with focusing flow on input sample to fix its position with respect to the sequential field non-uniformities for separation. (b) Field lines to cause particle deflection from initial focused position by: (i) negative DEP (nDEP) and (ii) positive DEP. (c) Imaged cell streamlines at the collection channels after DEP separation, shows a low membrane capacitance fraction (Fixed RBCs) exhibiting nDEP, and a high membrane capacitance fraction (control RBCs) exhibiting pDEP under 100 Vpp at 300 kHz, at a sample flow rate of 3.6 µl/min. (d) The separated fractions measured downstream by single-cell impedance cytometry (10000 events for each cell type), which is measured in (e) as distinctly higher opacity for the collected nDEP fraction (fixed RBCs) versus the pDEP fraction (normal RBCs)*

Modulating Interior Conductivity and Fluorescence

Considering ghost RBCs prepared by membrane resealing in media of differing conductivity, we expect no significant differences in membrane capacitance for well-sealed membranes but anticipate systematic differences in interior conductivity. The varying RC time constant (τ_{RC}) arising from an increase in interior conductivity is expected to upshift the frequency dispersion in impedance phase ($\phi(Z)$), while the impedance phase level would be systematically altered to be shifted further away from insulating beads that are normalized to $\phi(Z) = 0$.

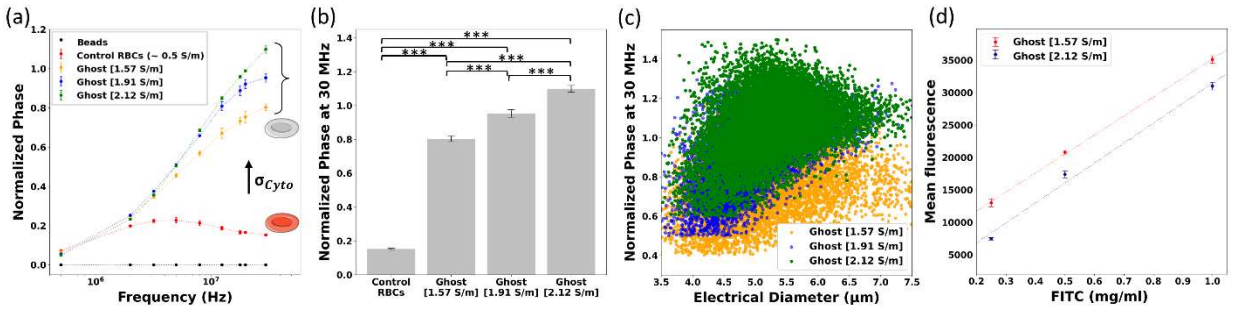

Figure 2.6: *Impedance data of ghost RBCs prepared by membrane resealing in media of differing conductivity (1.57, 1.91, and 2.12 S/m) and of differing levels of FITC−dextran (0.25, 0.5, and 1 mg/mL). (a) Frequency dispersion of the normalized impedance phase (ϕZ; points connected by lines to guide the reader); (b) Mean phase at 30 MHz (ϕ30MHz) indicates the significant differences (***p < 0.001) between the cell types; (c) Scatter plot of normalized impedance phase (30 MHz) vs electrical diameter; (d) Fluorescence of ghost RBCs after membrane resealing in buffers with differing conductivity (S/m) and FITC levels.*

In fact, this is apparent in **Figure 2.6a**, with the successively higher interior conductivity of each type of ghost RBC causing a phase dispersion that is shifted to progressively higher frequencies, while the impedance phase levels are also gradually increased to become shifted further away from that of the insulating beads. The single-event scatter plot of ϕ(Z) versus electrical diameter (**Figure 2.6c**) shows the successive alteration of ϕ(Z) at high frequency for each ghost RBC type. The averaged ϕ(Z) level for each ghost RBC type at 30 MHz, which reflects property alterations at the interior of each cell type, shows statistical significance of their distinction based on this impedance phase metric (**Figure 2.6b**). To assess effectiveness of the resealing protocol, the ghost RBCs were resealed in buffers of different conductivity that also include different FITC-dextran levels (0.25, 0.5, and 1 mg/mL), as confirmed by fluorescence images (**Figure 2.7**). The flow cytometry results (**Figure 2.6d**) confirm a similar level of FITC in the ghost RBCs, regardless of the buffer conductivity used to reseal. The small differences between the fluorescence level of the ghost RBC types are attributed to alterations in the kinetics of resealing for the ghost RBCs in 1.57 S/m versus in 2.12 S/m buffers. However, the mean fluorescence levels within each ghost RBC type can be linearly modulated based on the FITC level in the buffer during resealing. Hence, by adding differing levels of FITC into the respective penetrating conductive PBS media, each type of ghost RBC modification can be identified based on a fluorescence level that is correlated to the interior conductivity of the ghost RBC type. For

instance, ghost RBCs penetrated with media of 1.57 S/m conductivity can be differentiated from those penetrated with media of 2.12 S/m conductivity, simply by using a differing FITC level in the penetrating media (e.g., 0.5 mg/mL for the former and 1 mg/ mL for the latter). This ability to independently alter the fluorescence and interior conductivity levels for each ghost RBC type enables them to be used in tandem for distinctions based on their fluorescence or high frequency impedance phase (>10 MHz) or both. The fluorescence level of the FITC-penetrated RBCs is in the range of intensities from standard beads used in flow cytometry (**Figure 2.7c**). Furthermore, these FITC-penetrated ghost RBCs with a well-defined DEP frequency response that arises due to their interior conductivity can be utilized together with fluorescence imaging or cytometry for facile determination of DEP separation metrics within heterogeneous samples composed of different ghost RBC types. Such model cells could be utilized for optimization of microfluidic geometries and the resulting separation force fields (voltages, frequency, media conductivity, flow rate, etc.). In summary, ghost RBC modification by membrane resealing to modulate cytoplasm conductivity with minimal alteration in electrical diameter and membrane capacitance can be used to independently modulate their fluorescence level, thereby enabling multimodal identification and optimization of DEP separation strategies to aid in microfluidic device design.

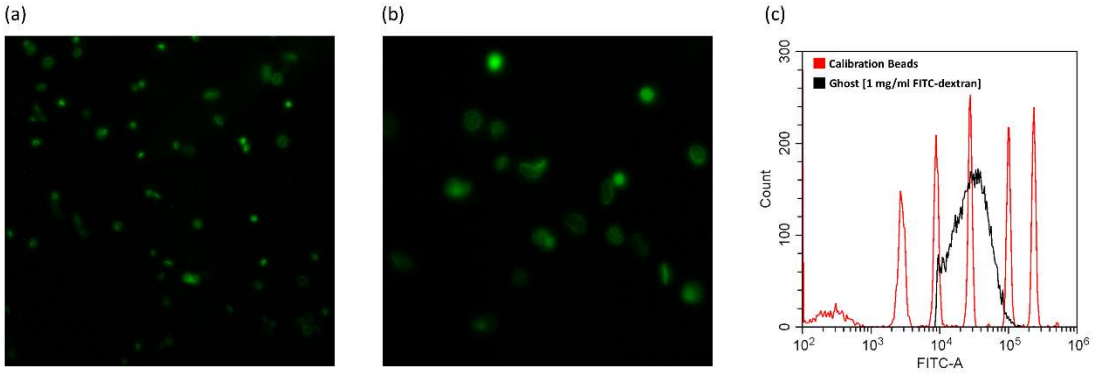

Figure 2.7: *(a) Fluorescent microscopy images (10x) of ghost RBCs resealed after penetration with 1.57 S/m buffer that includes 0.5 mg/ml levels of FITC-dextran. The images of the same sample are also shown at 40x (b). (c) The fluorescence level of fluorescein in ghosts RBCs [1 mg/ml FITC-dextran] is compared to the level of fluorescein in calibration beads used for flow cytometry.*

Modulation of Membrane and Cytoplasmic Properties

Finally, each ghost RBC type is fixed with differing levels of glutaraldehyde, so that the membrane capacitance can be varied for cells of differing interior conductivity. This is apparent from differing opacity levels (inverse of the membrane capacitance) for ghost RBCs that are first penetrated with 1.57 S/m PBS media and then fixed by differing levels of glutaraldehyde (**Figure 2.8a**), as per the significance plot (**Figure 2.8b**). Difference between fixed ghost (0.1%) and fixed RBC (0.1%) is apparent within the high frequency impedance phase response (>10 MHz in **Figure 2.8c**) that shows statistical significance (**Figure 2.8d**).

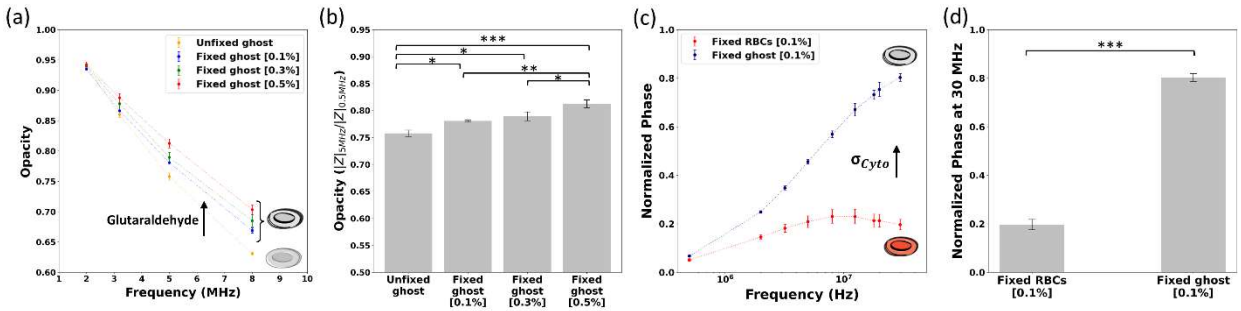

Figure 2.8: *RBCs with modulated membrane capacitance (a, b) and with modulated interior conductivity (c, d) measured based on frequency region for the impedance analysis of ghost RBCs after membrane resealing in buffer of media conductivity of 1.57 S/m and after fixing with different levels of glutaraldehyde (0.1%, 0.3%, and 0.5%). (a) Systematically differing frequency dispersions in opacity, with (b) statistically significant differences in* $|Z|_{5\ MHz}/|Z|_{0.5\ MHz}$. *(c) The interior conductivity of these fixed ghost RBCs vs similarly fixed RBCs without electrolyte penetration shows differences in frequency dispersion of normalized impedance phase at 30 MHz that show statistically significant differences (d). The statistical significance is indicated by *p < 0.05 level; **p < 0.01 level; ***p < 0.001 level (points on the frequency dispersion connected by lines to guide the reader).*

Benchmarking Unknown Phenotypes versus Modified RBCs of Known Dielectric Properties

The impedance spectra from each RBC type are fit to standard single-shell dielectric models [56] for the computation of their dielectric parameters (**Table 2.1**) of cell membrane capacitance and cytoplasmic conductivity, based on subcellular geometric parameters for RBCs obtained from

prior work (fixed membrane thickness 5 nm and fixed membrane conductivity $\leq 10^{-8}$ S/m) [20]. Cell radius estimation from the single shell model is ~ 2.6−2.7 μm for all modified RBCs.

Table 2.1: Dielectric parameters for each RBC-type based on fitting of their impedance spectra to a single-shell model*. (Model fitting parameters: RBC membrane thickness (d_{mem})= 5 nm, RBC membrane conductivity (σ_{mem}) = 1 × 10^{-8} S/m, RBCs cytoplasm permittivity (ε_{int}) = 80, Bead conductivity = 2.7 × 10^{-3} S/m, Bead permittivity = 2.5, Bead radius (r_{Bead}) = 5 μm, medium conductivity (σ_{medium}) = 1.6 S/m, medium permittivity (ε_{medium}) = 80)

Sample	Membrane capacitance ($C_{membrane}$) [mF/m^2]	Cytoplasm conductivity ($\sigma_{cytoplasm}$) [S/m]
Control RBCs	8.85 ± 0.23	0.5 ± 0.01
Fixed RBCs [0.01%]	5.66 ± 0.36	0.5 ± 0.03
Fixed RBCs [0.1%]	4.95 ± 0.14	0.5 ± 0.01
Fixed RBCs [1%]	4.07 ± 0.25	0.5 ± 0.03
Unfixed ghost (1.57 S/m)	8.85 ± 0.35	1.2 ±0.03
Fixed Ghost (1.91 S/m) [0.1%]	7.08 ± 0.22	1.4 ± 0.04
Fixed Ghost (2.12 S/m) [0.1%]	7.08 ± 0.35	1.6 ± 0.05
Fixed ghost [0.1%] (1.57 S/m)	7.08 ± 0.2	1.2 ± 0.06
Fixed ghost [0.3%] (1.57 S/m)	6.70 ±0.18	1.2 ± 0.02
Fixed ghost [0.5%] (1.57 S/m)	6.20 ± 0.25	1.2 ± 0.04

*The square bracket indicates the glutaraldehyde level for fixation and the rounded bracket indicates conductivity of the penetrating buffer prior to resealing.

As expected, in comparison to control RBCs that are unmodified, the RBCs that are fixed to successively higher levels show successively lower membrane capacitance and no alteration to their cytoplasmic conductivity. Similarly, ghost RBCs penetrated with successively more conductive media, prior to resealing, show successively higher interior conductivity in comparison to control RBCs that are unmodified. It is noteworthy that the interior conductivity of ghost RBCs gradually increases to become close to that of the penetrating media, with 1.57 S/m penetrating

media reaching an interior conductivity of 1.2 S/m, 1.9 S/m penetrating media reaching an interior conductivity of 1.4 S/m, and 2.12 S/m penetrating media reaching an interior conductivity of 1.6 S/m. The efficacy of the resealing process is confirmed based on their high membrane capacitance and low membrane conductivity values. The fixed ghost RBCs show alterations only in membrane capacitance, while maintaining their cytoplasmic conductivity level. Hence, not only are the phenomenological impedance metrics of each RBC type altered in characteristic manners, but their fitted inherent biophysical properties also span over a broad range. This relationship between the phenomenological and biophysical properties for each RBC type is shown in **Figure 2.9**, wherein the position of each RBC type is plotted with respect to solid lines that indicate varying membrane capacitance levels and the dashed lines that indicate varying cytoplasmic conductivity levels. Based on this, for an unknown RBC type (indicated as X in green font in **Figure 2.9a**), the impedance opacity at 5 MHz (=0.86) and the normalized impedance phase at 30 MHz (=0.2) that are obtained from the impedance spectra can be located on the map, so that the solid/dashed lines can be followed for determining the cytoplasm conductivity (~0.5 S/m) and membrane capacitance (~4.1 mF/m^2) values for the unknown RBC type (**Figure 2.9b**), without the need to fit its full impedance spectra. In fact, spectra from this unknown RBC type (control RBC fixed with 1% glutaraldehyde) fit by the shell model to a comparable cytoplasm conductivity (= 0.5 S/m) and membrane capacitance (=4.07 mF/m^2), indicating high accuracy of such a mapping approach.

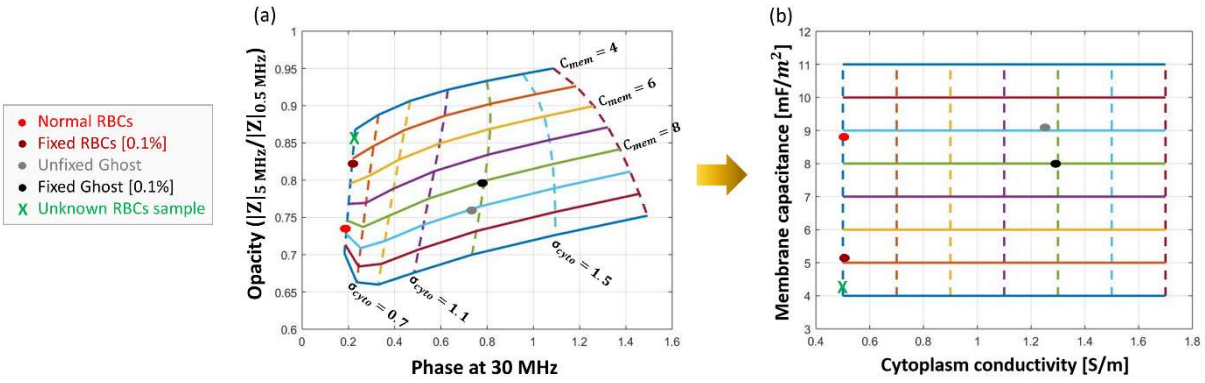

Figure 2.9: *Translating from phenomenological impedance metrics, such as the opacity vs phase contrast plot (a) to cellular biophysical properties of cytoplasm conductivity vs membrane capacitance (b), as obtained from shell-model fits is accomplished for unknown RBCs without the need to do a shell model fit. Instead, the impedance metrics for the unknown RBCs are mapped on the respective plot for the known modified RBCs, so that their biophysical properties can be*

determined by projection onto the colored solid lines that show contours of differing membrane capacitance values and colored dashed lines that show contours of differing cytoplasm conductivity, with each color indicating specific levels.

Fitting of impedance spectra to dielectric shell models usually requires certain fixed parameters (geometric properties like cell size and membrane thickness, for instance) and other "fitting" parameters (for instance: interior permittivity or membrane conductance) to go from phenomenological impedance metrics to biophysical properties. While these are known for model cells, like the modified RBC types in this work, the same is not the case for unknown RBC types. Hence, utilization of this approach (**Figure 2.9**) to go from the phenomenological parameters to biophysical properties for unknown cell types can be conducted by simply comparing their phenomenological metrics versus those of the model RBC types, with no need for arbitrary geometric properties or "fitting" parameters for these unknown cell types. The associated off-line computation time is also not needed, thereby allowing for in-line biophysical recognition. Furthermore, based on membrane capacitance values (C_{membrane}) determined from the map of **Figure 2.9**, the spread in crossover frequency ($f_{\text{crossover}}$) at a particular media conductivity (σ_{media}), for individual cells of a given hydrodynamic radius (r) can be calculated [57, 58]:

$$\left(f_{crossover} = \frac{\sqrt{2}\,\sigma_{media}}{2\pi r\, C_{membrane}}\right) \qquad (1)$$

For instance, the map suggests that the C_{membrane} for the unknown sample (1% fixed control RBC) is about 4.1 mF/m^2, while that for an unmodified sample of control RBCs is about 9 mF/m^2. Based on Eq. (1), The computed $f_{\text{crossover}}$ values of 813293 and 370500 Hz, respectively, agrees well for the respective RBC types with their validated levels determined using the 3DEP reader (**Figure 2.10**).

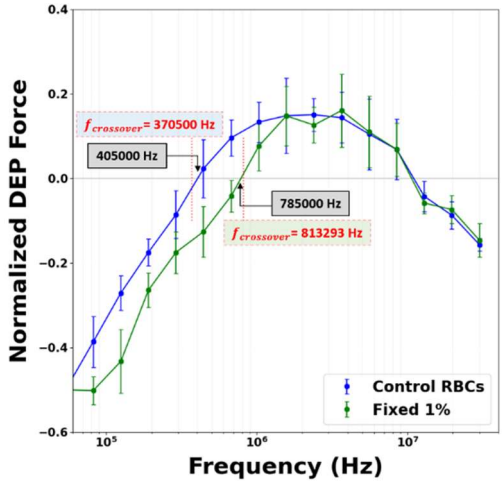

Figure 2.10: *DEP frequency spectra of normal RBCs versus fixed RBCs [1%] (unknown sample). DEP spectra were measured at media conductivity of 400 μS/cm in a 3DEP reader. The crossover frequency of DEP spectra compared with computed crossover frequency by Eq. (1) (dashed red line). For the normal RBCs the crossover frequency of the DEP spectra is 405000 Hz and the estimate crossover is 370500 Hz. For the fixed RBCs [1%] the crossover frequency of the DEP spectra is 785000 Hz and the estimate crossover is 813293 Hz.*

CONCLUSIONS

To address the need in impedance-based flow cytometry and in dielectrophoresis, for standard particles with well-modulated subcellular electrical physiology to benchmark unknown samples and to normalize for temporal device-level deviations, we present a class of modified RBC types. Glutaraldehyde fixation at varying levels is able to generate a class of fixed RBCs with well-modulated membrane capacitance, as measured by electrical opacity, but with no alterations to their interior conductivity. RBC membrane resealing after electrolyte penetration from the media to vary cytoplasmic conductivity inside each cell is able to generate ghost RBCs with well-modulated interior conductivity, as measured by normalized impedance phase, but with minimal alterations in membrane capacitance. Along similar lines, by penetrating the RBCs with differing FITC levels in the electrolyte prior to resealing, ghost RBCs with well-modulated fluorescence can be generated. Interestingly, the fluorescence and interior conductivity levels can be independently altered for each ghost RBC type so that the respective values can be correlated to identify translation of particular ghost RBC types in microfluidic devices. Such model ghost RBCs of differing interior conductivity levels that lead to well-defined DEP frequency responses can be

utilized together with fluorescence imaging or cytometry as coflowing cells within heterogeneous samples for facile determination of DEP separation metrics. Such model cells could be utilized for optimization of microfluidic geometries and the resulting separation force fields (voltages, frequency, media conductivity, flow rate, etc.). To illustrate the application of these model RBC types for the purpose of benchmarking unknown RBC types, we present a map that allows facile translation from phenomenological impedance metrics to inherent biophysical properties for each RBC type. In this manner, single-cell impedance data from unknown RBC types can be mapped versus these model RBC types for the facile determination of subcellular biophysical information and the spread of their dielectrophoretic crossover frequency, without the need for time-consuming algorithms that often require unknown fitting parameters. RBCs are the simplest model cell, and future work will investigate the extension of the approach to other cell types with a more complex internal structure. Such standards for biophysical cytometry can enable inline phenotypic recognition strategies.

Chapter 2: Automated biophysical classification of apoptotic pancreatic cancer cell subpopulations using machine learning

Dysregulation of apoptotic signaling in the immunosuppressive tumor microenvironment is linked to resistance of pancreatic cancer cells to cytotoxic therapies, leading to much interest in modulating cell death by distinguishing the progression of subpopulations under drug treatment towards early apoptotic, late apoptotic, and necrotic states. While flow cytometry after fluorescent staining can monitor apoptosis with single-cell sensitivity, the background of non-viable cells within non-immortalized pancreatic tumors from xenografts can confound distinction of the intensity of each apoptotic state. Using drug-treated pancreatic cancer cells from tumor xenografts of differing gemcitabine sensitivity, we identify biophysical metrics from single-cell impedance cytometry to quantify subpopulations at the early apoptotic versus late apoptotic and necrotic states, by using machine learning to train for recognition of each phenotype. Such automated biophysical classification to follow the progression of apoptotic phenotypes can be used to modulate cancer cell death and advance longitudinal analysis to discern drug resistant phenotypes.

Introduction

Programmed cell death by apoptosis [59] serves a key role in the homeostasis of tissues [60] and in cell clearance by phagocytes [61]. The dysregulation of apoptotic signaling is a hallmark of diseases, such as cancer [62]. Specifically in pancreatic cancer [63] that is attributed to pancreatic ductal adenocarcinoma or PDAC, which is the third leading cause of cancer death [64] and has a 5-year survival rate of less than 6% [65-67], molecular defects in apoptotic signaling cause resistance of cancer cells to cytotoxic therapies by reprogramming of the tumor microenvironment. Since an overwhelming majority of patients with PDAC (80%) have inoperable disease at presentation [68] and their median survival duration thereafter is only 3-7 months, chemotherapy is often the only option to control their disease and prolong survival. However, the highly fibrotic PDAC tumor microenvironment limits chemotherapy drug penetration [69], while efficacy of the drug is limited by mutations, stress responses and metabolic reprogramming in the cancer cells that lead to drug resistance. Given the limited time window for chemotherapy in PDAC and the broader inefficacy of translating pre-clinical studies [70, 71] to human trials [72] in cancer therapy, high sensitivity strategies for monitoring of cell phenotypes on physiologically relevant in vitro models or in vivo biopsies to discern drug-induced apoptotic responses are needed to complement current methods based on tumor volume imaging. However, this is limited by the absence of reliable genetic and transcriptional markers of drug sensitivity and resistance [73], which motivates us to consider biophysical markers [74, 75].

Drug-induced cell death by apoptosis and necrosis (including drug-regulated necroptosis), as well the onset of drug resistance, are associated with characteristic cellular biophysical features [76]. Apoptosis usually involves cell shrinkage, chromatin condensation and ruffling of the plasma membrane [77], eventually leading to break-up of the cell into apoptotic bodies that consist of plasma membrane bound cell organelles and nuclear materials, which are cleared by phagocytosis (**Figure 3.1A**). For apoptosis in PDAC [78], the cell receptor mediated extrinsic pathway is enhanced by intrinsic pathways based on mitochondrial membrane permeabilization to release its proteins, and on Ca^{2+} regulated alteration of the endoplasmic reticulum [63, 79]. Necrosis leads to swelling of organelles and disruption of plasma membrane (**Figure 3.1A**), but it can be triggered by stimuli shared with extrinsic apoptosis in presence of caspase inhibition [80, 81]. The morphological changes associated with drug resistance include the emergence of irregular cell

shape in pancreatic cancer [82], larger and irregular-shaped cells of high nucleus to cytoplasm ratio in breast cancer [83, 84], spindle-like shapes and diffusive plasma membrane shape [85] in colon cancer HCT8 cells, and elongated and irregular fibroblastoid morphology for drug-resistant ovarian cancer cells (ACRP) versus that of drug-sensitive cells (A2780) [86].

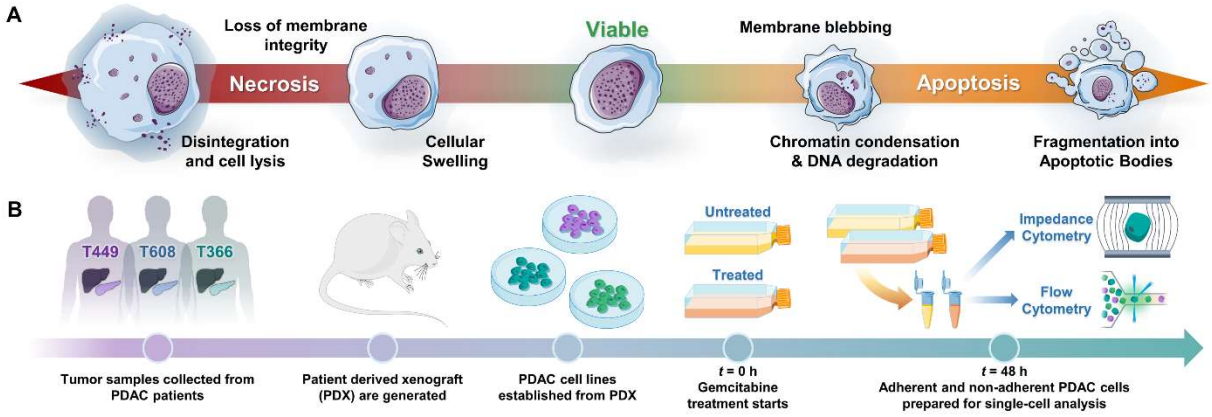

Figure 3.1: *A – Biophysical changes under apoptosis vs. necrosis. B – Schematic of experimental protocol to quantify progression of viable cells towards various stages of apoptotic and necrotic subpopulations by impedance cytometry of gemcitabine treated patient-derived PDAC cell types.*

Cell proliferation assays have traditionally guided in vitro drug sensitivity studies, but these cannot distinguish the cell death mechanism and they cannot be conducted with single-cell sensitivity to quantify the subpopulations in heterogeneous samples. Flow cytometry to quantify phosphatidylserine (PS) on the surface of cells by fluorescent staining with Annexin V (AV) can follow apoptosis with single-cell sensitivity [62], while loss of viability under necroptosis can be followed by staining of permeable cells with dyes such as propidium iodide (PI) or DAPI. However, with non-immortalized pancreatic tumors from patient-derived xenografts (PDXs), the high background of non-viable cells in the untreated sample can confound early distinction of drug sensitivity after treatment. Additionally, since AV can be highly expressed by apoptotic cells due to PS exposed on the membrane outer leaflet, as well as by cells with compromised plasma membranes by dye penetration to stain PS naturally present on the membrane inner leaflet, there is the need for other more specific apoptotic markers. Furthermore, given the importance of modulating tumor cell death to prevent an inflammation-driven immunosuppressive microenvironment that is conducive to tumor recurrence [87], there is much interest in techniques capable of distinguishing the progression of apoptotic states, which is not easily accomplished by

flow cytometry. Hence, we consider single-cell biophysical cytometry to explore the progression of cellular phenotypes from viable through to various apoptotic states (early to late), and onward to the necroptotic state.

Biophysical cytometry for label-free single cell analysis using electrical, mechanical, and imaging modalities can potentially complement the biochemical information on expression profiles of cell markers obtained from flow cytometry after fluorescent staining. However, biophysical cytometry has typically yielded data of low dimensionality and requires computationally intensive strategies to process data on low event numbers, which has limited its application [48]. Impedance cytometry [15, 16, 18] is an emerging non-invasive, sensitive, and high throughput (300 – 400 events/s) technique that can provide multiparametric biophysical information, based on disruptions to the magnitude and phase of alternating current flow by single cells or subcellular particles in a microchannel that is followed simultaneously over several frequencies in the 0.5 to 50 MHz range. In this manner, biophysical phenotypes associated with apoptosis or necroptosis, such as shrinkage or swelling can be discerned based on cellular electrical size at low frequency (~0.5 MHz), while membrane features, ruffles or permeabilization can be discerned based on membrane conductance and capacitance at mid-frequencies (2-10 MHz), and features in the cell interior due to the endoplasmic reticulum, mitochondria, or nucleus can be followed at high frequencies (≥10 MHz) based on the interior conductivity and nucleus to cell size ratio [19]. Using size-controlled co-flowing insulating beads for data normalization [6], impedance magnitude ($|Z|$) and phase (ϕZ) metrics can be quantified and compared across different biological samples over multiple frequencies, so that the dispersions can provide multiparametric information on cell phenotypes [25, 88]. Furthermore, the frequency spectra of single-cell impedance phenotypes can be fit to dielectric shell models to obtain a biophysical picture to identify each cell type in a heterogeneous sample and gauge the myriad subcellular alterations over a spectrum of drug-induced transformations [26]. Prior work on human lymphoma cells classified their drug-induced transformations within the viable, necrotic, and apoptotic categories [24], but subpopulations over the progression of apoptotic alterations were not quantified. Furthermore, quantification of the subpopulations was by manual gating strategies, which is limited by overlap of the respective data clusters, motivating the consideration of automated strategies for impedance data classification. Recent reports have explored automation of impedance-based phenotypic classification, including application of k-means algorithm-based clustering of subpopulations of

peripheral blood mononuclear cells [89], support vector machine (SVM) classifier to discriminate between live and dead T47D breast cancer cells [90], and SVM classifier applied to quantify eight groups of pollen grains [91], as well as neural networks to classify five different cell types [92]. However, these studies do not involve heterogeneous cellular systems composed of evolving subpopulations with closely related phenotypes, as observed in drug sensitivity studies with tumor cell types at different stages of apoptosis.

In this chapter, we seek to utilize biophysical metrics for quantifying the drug sensitive phenotypes of cancer cells over the progression of viable, early apoptotic, late apoptotic, and necrotic subpopulations, as obtained through impedance cytometry of pancreatic tumor PDXs under gemcitabine treatment. Specifically, based on positive controls for the respective subpopulations and their anticipated biophysical characteristics, we explore machine learning (ML) strategies to train for phenotypic recognition, so that automated classification of the impedance data clusters can occur from heterogeneous samples of these subpopulations. The ML methods for classification include unsupervised learning focused on sub-population clustering and supervised learning focused on classification and pattern prediction. In this manner, the hidden relationships between biophysical metrics, which cannot be easily determined with a standard 2- or 3-dimensional analysis, can be utilized at a hyperdimensional level to cluster and classify subpopulations in an automated manner. To validate our automated classification of impedance cytometry data, we compare against flow cytometry after staining for AV and Zombie Near-Infrared (ZNIR; a dye permeable to cells with compromised membranes) to quantify apoptotic and necrotic subpopulations, respectively, while utilizing PDXs with differing degrees of gemcitabine sensitivity to compare the relative proportions at the early apoptotic versus late apoptotic and necrotic stages (**Figure 3.1B**). While machine learning-based classification of impedance cytometry data clusters compares well against flow cytometry for quantification of apoptotic versus necrotic and live cell phenotypes, we infer that impedance cytometry is especially well suited towards discerning the relative intensity of onset of apoptosis, by distinguishing early from late apoptosis and necrosis. Given the importance of modulating cancer cell death for preventing an immunosuppressive tumor microenvironment and the need for label-free tools to repeatedly analyze the same sample to discern drug resistant phenotypes, we envision a key role for ML-based classification of impedance data clusters in following the progression of drug-induced apoptotic phenotypes based on biophysical metrics.

Materials and Methods

Patient-Derived Pancreatic Tumor Xenografts and Cells

PDAC tumor samples were generated from remnant human tumor surgical pathology specimens collected in collaboration with the University of Virginia Biorepository and Tissue Research Facility, and with the approval of the University of Virginia Institutional Review Board for Health Sciences Research following written informed consent from each patient. Tumors were propagated orthotopically on the pancreata of immunocompromised mice (**Figure 3.1B**). Tumor growth characteristics were measured, samples were collected for genotyping, and xenograft lines were established [93, 94]. Cells were transduced with firefly luciferase lentivirus (KeraFAST), selected using puromycin and maintained in RPMI 1640 (Thermo Fisher Scientific) with 10% FBS (Gemini Bioproducts) and 2 mM glutamine (complete medium), with fresh aliquots thawed, propagated, and used for experiments.

Cell Proliferation Assays, Hypotonic Treatments and Gemcitabine Treatments

For the proliferation assays, cells (~3×10^3) were plated in a 96-well plate in complete medium and allowed to attach overnight. Following one day of growth, the cell number was determined to initiate drug treatment and then replenished after 48 h, as needed for each experiment. PDAC cells were exposed to various doses (0.01 μg/mL, 0.1 μg/mL and 1 μg/mL) of gemcitabine (University of Virginia clinical pharmacy) for 24 h, 48 h and/or 96 h in complete medium, with control samples being kept under the same time periods. Upon harvest, the CyQUANT® cell proliferation assay (Invitrogen, ThermoFisher) was used to determine the relative cell number, using a plate reader (Biotek). Cells were also exposed to hypotonic and gemcitabine treatments for flow and impedance cytometry experiments, with untreated controls samples being kept for both experiment types. Hypotonic treatments were performed by removing the cell culture medium from culture wells and adding 1 mL of DI water. The exposure period of cells to DI water was varied (2 min, 20 min or 75 min) in order to generate different ratios of viability sub-populations. After this exposure period, DI water was removed from the wells and fresh complete medium was added. The cell cultures were then incubated and cultured for different time periods (20 min, 1 h, 4.5 h or 12 h), after which the cells were dissociated and processed for flow and impedance cytometry.

Gemcitabine treatments were performed by exposing cell cultures to 1 μg/mL of gemcitabine for 48 h in complete medium. Cells were prepared for flow and impedance cytometry.

Sample Preparation

Cell culture media, i.e., RPMI 1640 with 10% FBS and 2 mM glutamine (complete medium), Thermo Fisher Scientific, post either hypotonic and gemcitabine treatments, were first aspirated and stored, with the remaining adherent cells being washed in 1×PBS (Thermo Fisher) and exposed to 0.5% trypsin in 1×PBS for 5 min at 37 ˚C. In order to retrieve both the adherent and non-adherent cells fractions, both the aspirated cell culture medium and trypsinized cells were re-suspended into a total volume of 5 mL DMEM with 10% FBS and 1% pen-strep (Thermo Fisher) and centrifuged at 300 g for 10 min. This sample was then aspirated, the cell pellet (containing both adherent and non-adherent cells) was re-suspended in 1xPBS, 500 mM EDTA (Fisher Scientific), and 0.5% Bovine Serum Albumin (Sigma Aldrich) and filtered through a 100 μm cell strainer. Cells were then counted with a hemocytometer and ~300,000 cells from each sample were then analyzed for flow and impedance cytometry measurements concurrently.

Flow Cytometry

After sample preparation, samples were stained with Annexin V (Thermo Fisher Scientific) and Zombie NIRTM (or ZNIR; APC-A750, Biolegend) following the provider instructions, and immediately analyzed. Flow cytometry was carried out using a CytoFLEX flow cytometer (Beckman Coulter), with data being analyzed using CytExpress (Beckman Coulter). The cell population was first gated based on forward (FSC) versus side (SSC) scatter data, to gate events that were too small to be considered cells; and then gated based on SSC Area versus Height, to gate out doublets events. Data from the FITC and APC-A750 filters were then used to plot the expression of Annexin V and ZNIR, respectively, with cells being gated according to their viability status.

Impedance Cytometry

After sample preparation, reference polystyrene beads (7 μm; Sigma) were added to each sample at a concentration of ~1×10^5 mL^{-1} and the heterogeneous samples were passed through a microfluidic device (50 μm × 50 μm cross-section) at 50 μL/min for measurement using an impedance analyzer (Ampha Z32, Amphasys AG), using simultaneously applied AC signals at

0.5, 2, 18 and 30 MHz to electrodes patterned within the channel (with acquisition settings of modulation, amplification and demodulation levels of 4, 5 and 1, respectively). The impedance signal trains were processed in real time for thresholding to store the single cell data in the form of impedance magnitude (|Z|) and phase (ϕZ) at each applied frequency.

Statistical Analysis

Data was processed and analyzed using MATLAB (R2018b, MathWorks). Flow and impedance cytometry data was processed to perform comparisons across experimental conditions. For impedance cytometry, the impedance signal of individual cells was normalized against the frequency-independent impedance response of the reference polystyrene beads by dividing the impedance data by the mean impedance data of reference beads. Due to normalization, impedance phase is herein reported in arbitrary units. PDAC cell populations were gated using normalized impedance data at 30 MHz, thereby removing smaller debris and the reference beads from further analysis steps. Normalized impedance magnitude is used to compute the metric of electrical diameter, by calculating $\sqrt[3]{|Z|_{0.5\,MH}}$ (using the polystyrene beads for size reference), and the metric of magnitude opacity, by calculating $|Z|_{prob-fre} \Big/ |Z|_{0.5\,MHz}$. Statistical analyses were performed on processed flow and impedance cytometry datasets, with significance level being defined at $\alpha < 0.05$ for all cases. One-way ANOVA tests were performed to compare datasets based on treatment conditions and cell lines, i.e., assessing whether datasets from untreated and drug treated or from the different cell lines could be assumed to come from samples of the same mean, with the null hypothesis being rejected ($p \ll 0.05$). Thus, two sample Students' t-tests were performed to compare individual datasets to assess statistically significant differences between treatment conditions and viability sub-populations.

Machine Learning Strategies

Machine learning strategies were implemented using MATLAB (R2018b, MathWorks) functions and applications. For unsupervised clustering of viability sub-populations, the datasets from the various experimental conditions from hypotonic treatments were merged to obtain a single dataset with the four expected viability sub-populations (data from ϕZ at 0.5, 2 and 30 MHz). Due to the observed 2D Gaussian distributions of the apparent clusters, the Gaussian Mixture Model (GMM) was implemented using MATLAB's fitgmdist function. The function was set to

identify k = 4 sub-populations within the dataset, with the individual sub-populations being attributed a specific class. With each population being classified, a supervised classification algorithm was then trained using MATLAB's Classification Learner application. The dataset comprised of data from ϕZ at 0.5, 2, 18 and 30 MHz, electrical diameter and magnitude opacity, and 5-fold cross validation was used. Different algorithms available in the application library were tested, including linear discriminant, quadratic discriminant, decision tree, support vector machines (SVMs) and K-nearest neighbors (KNN). Confusion matrices for each algorithm were generated to assess the performance of each method. The accuracy of each algorithm was determined by calculating the ratio between the total number of true positives and negatives (i.e. the number of times the classifier accurately predicted the class of an event) and the total number of events. The optimal algorithm was a weighted KNN, with an accuracy of 98.4%, using K = 10 neighbors, the Euclidean distance, and a squared inverse for the distance weight. A weighted KNN typically performs better than a traditional KNN as it gives more weight to the events which are nearby and less weight to events farther away from the event being classified. Moreover, when compared to other, also high performing algorithms, such as SVMs, KNN is typically a much faster method, allowing for high accuracy while saving computation time and complexity. Using MATLAB trainClassifier function to recreate the optimal classification model, the weighted KNN algorithm was then implemented in the datasets from gemcitabine-treated PDAC samples for classification of the viability sub-populations.

Results

Inability to discern the progression of apoptotic states by flow cytometry

Patient-derived PDAC tumors MAD 14-449, 08-608 and 09-366, referred to herein as: T449, T608 and T366, respectively, were enlarged in mice as xenograft lines [93, 94], and form the subject of these studies. Gemcitabine is a common chemotherapeutic drug for PDAC that functions as an inhibitor of cellular DNA synthesis, leading to fragmentation of the DNA and the expression of apoptosis-related genes that induce the cell death by apoptosis [95]. Cell proliferation assays were used to screen the gemcitabine sensitivity to characterize the levels of cell death in each PDAC cell type (T449 PDX in **Figure 3.2A** and all other cell types in **Figure 3.3**) using a range of gemcitabine concentrations (0.01, 0.1 and 1 µg/mL) for three different exposure periods (24, 48 and 96 h), with each untreated control sample maintained in complete medium for the same

durations. The cell numbers were estimated using a DNA intercalating fluorescent dye to calculate the percentage of cell proliferation by comparing fluorescence of treated cell cultures with those from the untreated control cultures. In this manner, the variations in proliferation percentages permit a classification of the drug sensitivity of each cell type. For T449 and T608 PDXs, treatments at 0.1 or 1 µg /mL for 48 h are sufficient to sharply reduce the proliferation to ~0% or less, indicating their sensitivity to gemcitabine. Moreover, the decrease in cell proliferation for T608 PDXs after 24 h of gemcitabine treatment at 0.1 or 1 µg/mL levels, indicates that this cell type is the most sensitive of those in this study. In contrast, T366 PDXs are the most resistant cell type, with no perceptible decrease in cell proliferation below the ~50% mark, even after the longest drug exposure (96 h) at the highest concentration of this study (1 µg/mL).

The effect of gemcitabine on each PDAC cell type was measured by flow cytometry to classify apoptotic and necrotic populations, after staining cells with Annexin V (AV) to measure phosphatidylserine (PS) as an apoptotic marker [96] and with Zombie Near-Infrared (ZNIR) as a cell viability dye to measure membrane integrity and function. The observed subpopulations with fluorescence include (**Figure 3.2B**): AV-ZNIR- events that signify viable cells with an intact membrane and no apoptotic markers, AV+ZNIR- events that signify early apoptotic cells with an uncompromised membrane, and ZNIR+ events that signify non-viable cells with a permeabilized membrane. Based on this, the dose of gemcitabine treatment at 1 µg/mL for 48 h for each PDAC cell type is used to quantify the proportions within each of the three subpopulations (**Figure 3.2C-E**). Comparing the untreated control (Unt) and the gemcitabine treated (Gem) samples, the drug sensitive cell types (T449 and T608 PDXs) show a significant reduction (*$p<0.05$ and ***$p<0.001$, respectively) in the viable fraction (AV-ZNIR-). This occurs as the ratio of apoptotic cells (AV+ZNIR-) increases significantly (*$p<0.05$) for T449, and the ratio of non-viable cells (ZNIR+) also increases significantly for T449 and T608 (*$p<0.05$ and ****$p<0.0001$, respectively). For the drug resistant cell line (T366), there is no significant reduction ($p=0.0598$) in ratio of the viable subpopulation, with only a significant (*$p<0.05$) increase in the proportion of non-viable cells, likely due to a baseline level of drug sensitivity (apparent in the proliferation studies – **Figure 3.3**). In general, non-immortalized cells of low passage number that are derived from a primary patient for generating the xenograft renders them to be much more sensitive to in vitro culture conditions, thereby increasing loss of viability over the drug treatment time frame. However, based on the low level of AV+ZNIR- fractions in the control samples and the obvious change in ZNIR+ fractions

post-treatment, we can confirm that the onset of apoptosis can be studied after gemcitabine treatment at 1 µg/mL for 48 h. It is noteworthy that the ZNIR+ events in this flow cytometry protocol cannot specifically discern the cell proportions at the necrotic state versus those progressing from late-stage apoptosis, since AV is highly expressed by apoptotic cells (due to PS on the membrane outer leaflet) and by non-viable cells with compromised membranes (due to PS naturally present on the membrane inner leaflet). Hence, we consider biophysical cytometry methods to distinguish phenotypes over the progression of apoptotic states.

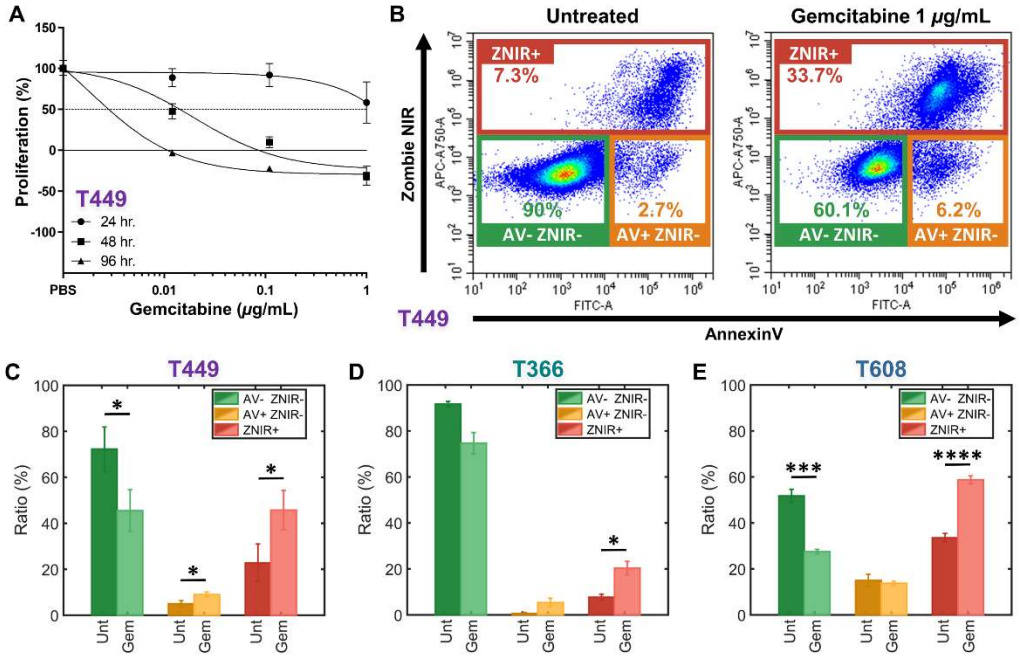

Figure 3.2: *A - Proliferation assays to screen drug sensitivity of PDAC cell types. Cell cultures were exposed to varying gemcitabine levels (0.01, 0.1, and 1 µg/mL) for: 24 h (circle), 48 h (square) and 96 h (triangle). Proliferation (%) is calculated as the relative proliferation under each treated condition compared with untreated for each exposure period and gemcitabine concentration. B – Flow cytometry density scatter plots of Annexin V (AV) versus Zombie Near-Infrared (ZNIR) for an untreated control and a gemcitabine treated T449 sample (1 µg/mL) for 48 h. Subpopulation ratios for gated AV-ZNIR- (viable cells), AV+ZNIR- (apoptotic cells) and ZNIR+ (non-viable cells) for PDAC types T449 (C), T366 (D) and T608 (E).*

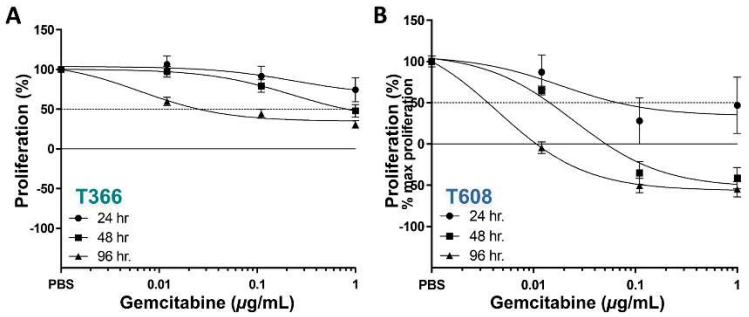

Figure 3.3: *Proliferation studies on PDAC cell lines: A – T366, and B – T608. Cell cultures were exposed to varying concentrations of gemcitabine (0.01, 0.1, and 1 μg/mL) for: 24 h (circle), 48 h (square) and 96 h (triangle). Proliferation (%) is calculated as the relative proliferation under each treated condition compared with untreated for each exposure period and gemcitabine concentration.*

Identifying the progression of apoptotic subpopulations using positive controls

The importance of modulating drug action on the tumor to prevent an immunosuppressive microenvironment highlights the need for tools to identify and quantify cellular subpopulations over the progression of apoptotic states and distinguish them versus their progression to the necrotic state [97, 98]. Specifically, we consider the sensitivity of impedance cytometry for detecting successive degrees of biophysical alterations associated with apoptosis [99, 100], that is characterized by cellular shrinkage, plasma membrane blebbing, the release of pro-apoptotic markers by the mitochondrion and the condensation of chromatin, and which gradually progresses to the loss of membrane integrity (also known as "secondary necrosis") in the absence of phagocytic clearance [101]; versus those alterations caused by necrosis [102], that is associated with cell swelling, loss of plasma membrane integrity, organelle swelling, lysosomal leakage and degradation of the DNA. To create "positive" controls for the respective apoptotic and necrotic subpopulations, we adapted the work from Selzner et al. [103] on a series of hypotonic treatments to control the progression of apoptotic states. Specifically, PDAC T449 cells were exposed to deionized (DI) water for a brief period to release ATP due to cell swelling and enable selective binding to ATP-P2 receptors, so that this purinergic signaling triggers apoptosis due to the activation of different pro-apoptotic proteins. Critically, the cells exposed to DI water must be returned to complete medium to allow a recovery period for triggering apoptosis. In this manner,

we explore the progression of apoptotic states obtained by exposing the respective cell cultures to DI water for different times, in combination with varying resting times in culture.

Flow cytometry measurements on the T449 PDXs exposed to the varying hypotonic conditions confirm generation of the respective subpopulations progressing from viable (AV-ZNIR- events in (i)) to apoptotic (AV+ZNIR- events in (ii-iv)) to necrotic states (ZNIR+ events in (v)) - **Figure 3.4A**. Compared to the predominantly viable cells of the untreated control (>95% AV-ZNIR- events; **Figure 3.4Ai**), cells exposed to hypotonic conditions for 2 min and cultured for 4.5 h (**Figure 3.4Aii**) exhibit high levels of AV staining, but without a great change in their ZNIR expression. In fact, the proportion of cells in the early apoptotic state (AV+ZNIR-) exhibits a sharp rise from just ~2.3% in the viable control to >50% after the hypotonic treatment. With the same 2 min hypotonic treatment that is maintained for a longer resting period in culture (12 h in **Figure 3.4Aiii**), the early apoptotic fraction is now reduced to ~21%, while the non-viable fraction (ZNIR+) increases from ~7% (**Figure 3.4Aii**) to ~27% (**Figure 3.4Aiii**). This suggests that the ZNIR+ events are likely associated with the continued progression of apoptosis, as expected for higher dose hypotonic treatments [103], rather than to cells in the necrotic state. Upon increasing the hypotonic exposure to 20 min, but with a shorter resting period (1 h), the proportion of ZNIR+ cells further increase to ~50%, with the ZNIR- cells presenting clear shifts towards high AV staining (**Figure 3.4Aiv**). Finally, upon exposure to a very long hypotonic treatment of 75 min (**Figure 3.4Av**), the great majority of cells (>97%) are found within the non-viable gate, indicating that most cells are rendered non-viable by necrosis under this severe treatment. Hence, we infer that PDAC cells will initiate apoptosis after a short hypotonic dose (AV+ZNIR- events) and that a severe hypotonic dose compromises the membrane (ZNIR+ events), but the intermediate hypotonic doses to advance progression of apoptosis presents the traditional hallmarks of both apoptosis (AV+ZNIR- events) and necrosis (ZNIR+ events). This limits the ability of flow cytometry to distinguish late apoptotic and necrotic cells for quantifying the subpopulations at different apoptotic states.

Multifrequency impedance cytometry of PDAC cells after the same hypotonic treatments was carried out to measure the biophysical phenotypes associated with the respective apoptotic subpopulations (**Figure 3.4B**). Since an intact lipid cell membrane screens the AC field at low frequencies in media of high conductivity (e.g., 1× PBS) to cause insulator-like behavior, the impedance magnitude and phase at 0.5 MHz ($|Z_{0.5\ MHz}|$ & $\phi Z_{0.5\ MHz}$) can be used to evaluate

alterations in cell size and membrane integrity [18]. With increasing frequencies, the capacitive coupling across the cell membrane renders cells to become more conductive, so that at a high enough frequency (e.g., 30 MHz), cell impedance is effectively dominated by the dielectric properties of the cell interior [18]. Hence, the impedance phase at 30 MHz ($\phi Z_{30\ MHz}$) can be used to evaluate alterations in electrical physiology of the cell interior. Using co-flowing polystyrene beads (7 μm), the impedance data of cells with conductive interior contents can be gated versus standard-sized beads with insulative contents for normalization to enable quantitative comparison across biological samples and their experimental conditions. Based on this, we analyze the events from individual cells using a plot of normalized impedance phase at low ($\phi Z_{0.5\ MHz}$) versus high ($\phi Z_{30\ MHz}$) frequency. In this plot, viable cells can be delineated by the region of high $\phi Z_{0.5\ MHz}$ and low $\phi Z_{30\ MHz}$ (**Figure 3.4Bi**), since the cells have an intact plasma membrane that shields the electric field from the cell interior. Following the first hypotonic treatment, a second cluster of events with a lower $\phi Z_{0.5\ MHz}$ and somewhat higher $\phi Z_{30\ MHz}$ versus the viable population is apparent (**Figure 3.4Bii**). We attribute this cluster to the early apoptotic subpopulation, as previously determined by flow cytometry in the AV+ZNIR- gate (**Figure 3.4Bii**). Characteristic biophysical traits of apoptotic cells, such as size shrinkage that reduces electric field screening would lower $\phi Z_{0.5\ MHz}$, as observed within this data cluster versus the viable population. Similarly, biophysical traits of the interior of apoptotic cells, such as Ca^{2+} regulated alterations to the endoplasmic reticulum or chromatin condensation to enhance the conductivity of the cell interior would increase $\phi Z_{30\ MHz}$, as observed within this data cluster versus the viable population. Following the second set of hypotonic treatments, an additional cluster of impedance events at even lower $\phi Z_{0.5\ MHz}$ and higher increasing $\phi Z_{30\ MHz}$ are apparent (**Figure 3.4Biii)**. Under the harsher hypotonic treatments, the event numbers in this cluster increase in correlation with decrease in the number of events in the apoptotic gate (**Figure 3.4Biii** to **Figure 3.4Biv** and **Figure 3.4Bv**), leading us to attribute cluster (with lowest $\phi Z_{0.5\ MHz}$ levels) to cells in the late apoptotic stage. This phenotype is likely associated with the disassembly process that is characterized by size reduction, shedding of apoptotic bodies, membrane morphology alterations and interior re-organization. A smaller size and compromised membrane (as part of "secondary necrosis") would explain the much lowered $\phi Z_{0.5\ MHz}$, while nuclear degradation, organelle fragmentation and a degree of intracellular ionic exchange with the highly conductive buffer could explain the increasing $\phi Z_{30\ MHz}$. After the harshest hypotonic treatments studied herein, another data cluster

emerges that is attributed to the necrotic subpopulation (**Figure 3.4Biv** and **Figure 3.4Bv**). The $\phi Z_{0.5\ MHz}$ level of this necrotic subpopulation is lower than that of viable cells, but higher than that of late apoptotic cells, while the $\phi Z_{30\ MHz}$ level is the highest amongst all the studied subpopulations. We suggest that cellular swelling in necrotic cells likely increases the $\phi Z_{0.5\ MHz}$ level for this subpopulation versus cells in the late apoptotic stage, with its permeabilized membrane reducing the $\phi Z_{0.5\ MHz}$ versus viable cells, while the higher $\phi Z_{30\ MHz}$ is associated with an increase in internal conductivity due to the uncontrolled intake of ions from the conductive buffer in the absence of cell clearance by phagocytosis.

Considering the differences between flow (**Figure 3.4Aiv**) and impedance (**Figure 3.4Biv**) cytometry after the 20 min hypotonic treatment, while flow cytometry indicates that ~17% of cells remain within the viable gate (AV-ZNIR-) and a majority of these cells exhibit a high level of AV staining that is almost indistinguishable from cells within the early apoptotic gate (AV+ZNIR-), impedance cytometry shows virtually no cells in the region associated with viable cells and a large cluster attributed to cells in the early apoptotic state. This suggests that the cells within the viable gate of the flow cytometry data (**Figure 3.4Aiv**) that are initiated into apoptosis based on a degree of AV expression, do not reach the threshold level of AV expression to locate the cells within the AV+ZNIR- gate. In contrast, for impedance cytometry, since the $\phi Z_{0.5\ MHz}$ level is sensitive to alterations in cell size and membrane conformation, it can be used to detect cells transitioning out from the viable state into the early apoptotic phenotype due to the respective hypotonic treatment. As a result, we anticipate divergences between the respective techniques in classifying subpopulations in the viable and early apoptotic gates. Furthermore, since impedance cytometry can differentiate cells in the late apoptotic versus necrotic states, as independent data clusters (**Figure 3.4Biv** and **Figure 3.4Bv**), whereas they occur as a single data cluster of non-viable cells in flow cytometry (ZNIR+; **Figure 3.4Aiv** and **Figure 3.4Av**), we anticipate divergences between their quantification of the respective subpopulations. In summary, through an appropriate choice of frequency and impedance metrics, biophysical properties can be used to detect the progression of viable cells into early and late apoptotic states, while distinguishing these subpopulations versus necrotic cells, but label-based flow cytometry methods that are reliant on the degree of PS staining for AV expression are not able to independently gate these phenotypes.

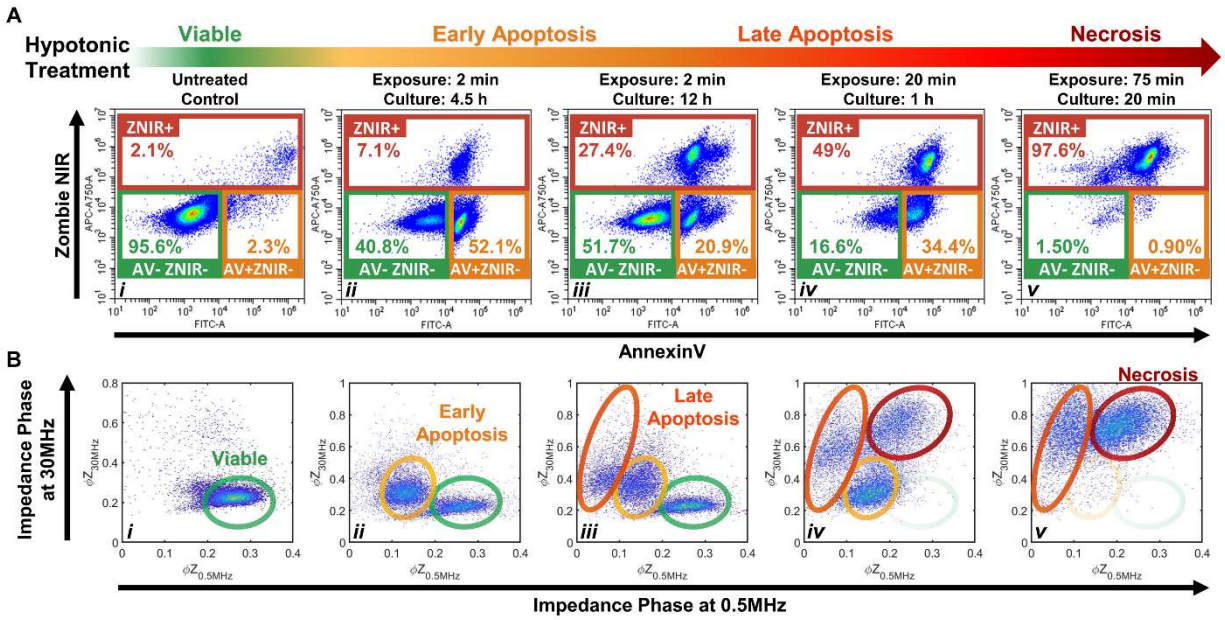

Figure 3.4: *Hypotonic treatment on PDAC T449 to generate positive control subpopulations across the viable to apoptotic and necrotic progression. A – Density scatter plots of Annexin V (AV) versus Zombie Near-Infrared (ZNIR) show that exposing cell cultures to DI water for increasing periods of time induces cells towards apoptosis and necrosis pathways. B – Density scatter plots of impedance phase at 0.5 MHz ($\phi Z_{0.5\ MHz}$) versus impedance phase at 30 MHz ($\phi Z_{30\ MHz}$) show characteristic impedance data clusters corresponding to the respective subpopulations across the viable to apoptotic and necrotic progression for the cell cultures exposed to hypotonic conditions.*

Automated Clustering by Unsupervised Machine Learning

Following the identification of viable, early apoptotic, late apoptotic, and necrotic subpopulations after hypotonic treatment based on their electrical physiology that creates distinct data clusters within the $\phi Z_{0.5\ MHz}$ vs. $\phi Z_{30\ MHz}$ plot, this information on the respective phenotypes is used to quantify proportions of the respective subpopulations after gemcitabine treatment of PDAC cell types. Rather than utilizing manual gates for delineating each cluster, which adds a degree of uncertainty to the accuracy of the clustering process and relies on 2D plots to determine the data contours for each subpopulation, we consider methods that utilize dispersion of the data on a multidimensional level by using multifrequency impedance metrics derived from the data. This holistic clustering approach is based on unsupervised machine learning methods to automate

clustering of data. These methods rely on the specific dispersion of each subpopulation cluster to calculate and catalogue each event within a specific cluster.

Based on the type of dispersions observed in the data, we explore the application of a Gaussian Mixture Model (GMM) for the clustering. GMM algorithms rely on the calculation of probabilities to define the likelihood of a given event to be part of each cluster, so that it is assigned at the end of the algorithm to the cluster with highest probability. As with most unsupervised learning algorithms, GMM requires as input a starting k number of clusters to be identified in the data. Since we observe four data clusters associated with viable, early apoptotic, late apoptotic, and necrotic subpopulations, we assume k = 4. Also, GMM assumes that clusters are dispersed following Gaussian distributions, which seems consistent to our observations (**Figure 3.4B**). The application of this strategy on the impedance cytometry data acquired for the T449 PDAC cell line after each hypotonic treatment is shown in **Figure 3.5**. The data from each hypotonic treatment was merged, so that the four subpopulations are present in the analyzed dataset (**Figure 3.5A**). Data from impedance cytometry with metrics of $\phi Z_{0.5\ MHz}$, $\phi Z_{2\ MHz}$ and $\phi Z_{30\ MHz}$ were used to provide the algorithm with multiparametric information that covers the electrical physiology for cell size (0.5 MHz), membrane integrity (2 MHz) and interior composition (30 MHz). Using this multi-parametric dataset, it is apparent that the GMM algorithm can identify the 4 expected clusters in the data (**Figure 3.5A**).

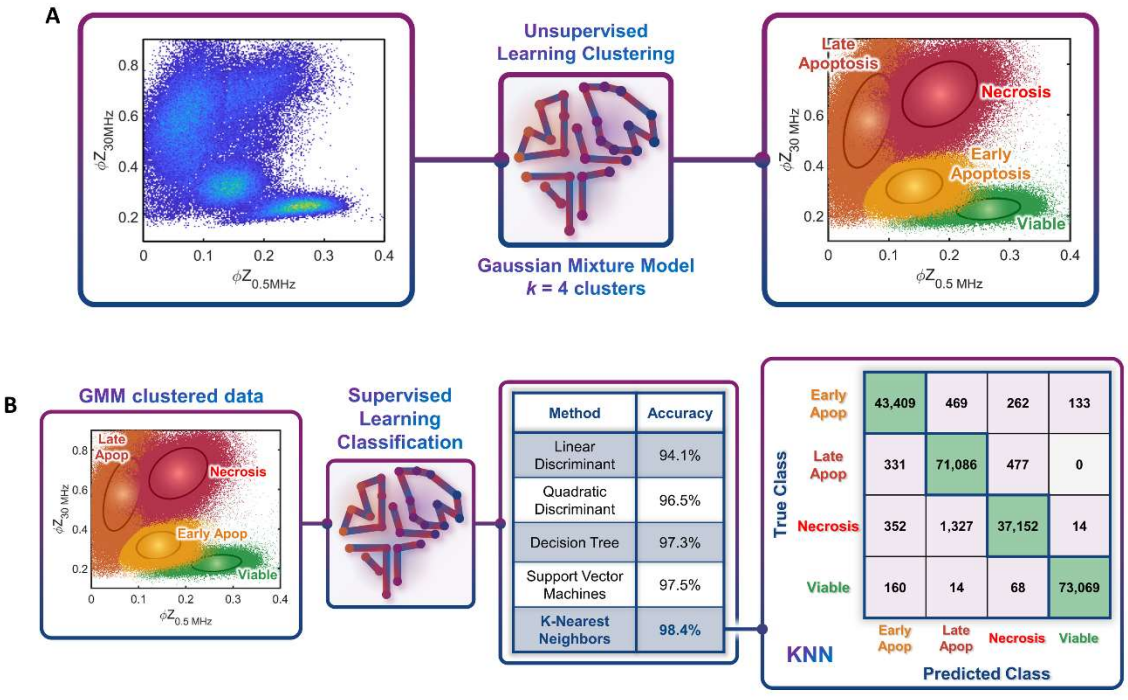

***Figure 3.5**: Machine Learning strategies. A. Unsupervised learning clustering, and B. Supervised learning classification. A – Density scatter plot of impedance phase at 0.5 MHz ($\phi Z_{0.5\ MHz}$) versus impedance phase at 30 MHz ($\phi Z_{30\ MHz}$) for merged data from the different hypotonic treatment samples were processed by the Gaussian Mixture Model (GMM), with k = 4 clusters, to identify various subpopulations across the viable to apoptotic and necrotic progression. B – Utilizing the clustered data, various classification methods were tested, with K-Nearest Neighbors (KNN) presenting the highest accuracy. The confusion matrix for the KNN method shows how the optimal model accurately classifies data.*

Automated Classification by Supervised Machine Learning

The characteristic electrical physiology based on biophysical properties of the four subpopulations (viable, early apoptotic, late apoptotic, and necrotic) is used to assess gemcitabine treated PDAC cell types using supervised machine learning strategies. Supervised learning methods can be used to perform classification tasks of datasets by cataloguing individual events based on their multiple properties. This classification process is reliant on a training step, wherein the algorithm is provided with a known dataset for "learning" the combination of properties that is characteristic of each class present in the data. After the training step, the developed algorithm is tested to assess its overall accuracy. If the algorithm provides a high accuracy, it can then be implemented on unknown datasets, if they share the same list of properties and expected classes. Hence, using the data acquired based on the different hypotonic treatments and the classified clusters identified by the GMM algorithm, we tested different supervised learning algorithms to identify the optimal one for implementation on impedance cytometry data acquired after gemcitabine treatment (**Figure 3.5B**).

Each of the tested algorithms provided an accuracy of at least 94%, with the optimal one being the K-Nearest Neighbors (KNN) algorithm (K = 10; accuracy = 98.4%). In this algorithm, an hyperdimensional distance is calculated between each unknown event and its K nearest neighbors from the known dataset, with the event being classified according to the class with the higher number of K neighbors. With enough iterations performed during the training stage, it is eventually possible to identify the set of properties and conditions that define the hyperparametric boundaries between each class. Hence, for every new unknown event, the KNN algorithm attributes a class to that event, permitting an automated classification process. The high accuracy of the KNN

algorithm can be confirmed by analyzing its confusion matrix. In this matrix, it is possible to observe what were the predicted classes from the algorithm versus the true classes. It is apparent that for most cases, the algorithm correctly classified each event. It is also interesting to note that most errors in classification arise due to misclassification with subpopulations that exhibit a high degree of phenotypic similarity. For instance, there are 0 true "late apoptotic" events that are predicted to be "viable" events, and only 14 events that were predicted to be "late apoptotic" that were in fact "viable" events, since these subpopulation types are clearly distinguishable in phenotype. The capability of the KNN algorithm to identify this difference is a good example of its accuracy and gives us confidence in implementation of this specific strategy to drug treated PDAC samples.

Quantifying the proportions of each apoptotic subpopulation for different tumor types

The trained KNN algorithm is then implemented on impedance cytometry data obtained from untreated and gemcitabine treated PDAC cells (**Figure 3.6**), including cell types with differing drug sensitivity (T449, T366 and T608). For all samples, the four subpopulations are apparent (**Figure 3.6A**), albeit at differing ratios (**Figure 3.6B**). The variations in ratios between the untreated and gemcitabine-treated samples follow the previously determined degrees of sensitivity for each cell line. Specifically, it is possible to confirm that both T449 and T608 are gemcitabine sensitive cell types, presenting significant reductions in their viable fraction (**$p<0.01$ & ****$p<0.0001$, respectively), accompanied by significant increases in their early apoptotic (*$p<0.05$ & ***$p<0.001$, respectively) and late apoptotic fractions (*$p<0.05$ & ****$p<0.0001$, respectively). For T608 PDXs, there is also a significant increase in the necrotic fraction (*$p<0.05$), which we attribute to the lower baseline for their viability, even in the absence of gemcitabine treatment. There are also some noteworthy trends correlating the impedance cytometry and flow cytometry results (**Figure 3.2C-E**). For T449, the observed significant increase in the ZNIR+ events within the flow cytometry data can be correlated to the data cluster in impedance cytometry data associated with the late apoptotic, rather than the necrotic subpopulation. For T608, we can infer that the sharp increase in the proportion of ZNIR+ events in flow cytometry data is closely associated with the significant increase in the late apoptotic fraction determined from impedance cytometry data. For T366, there are no significant decreases in the viable fractions, with the only

significant increase (*p<0.05) occurring for the late apoptotic ratio with gemcitabine treatment. This small increase was also observed in the flow cytometry data (**Figure 3.2D**), but it was associated with an increase (*p<0.05) in the ZNIR+ sub-population. These observations confirm that T366 is the most resistant cell line among the tested ones, with only a small portion of the cells belonging to this cell line undergoing gemcitabine-induced apoptosis. The direct comparison between the estimated ratios for each cell line can be found on **Figure 3.6C**. The ratios of late apoptotic and necrotic subpopulations were merged for impedance cytometry data to allow for comparison with flow cytometry ZNIR+ subpopulations. Comparing the estimated ratios between each technique, it is clear that the ML-based estimations closely match those made based on flow cytometry. In terms of mismatches, previous results (**Figure 3.4**) already anticipated the divergences between quantification of subpopulations, especially in cases where cells are transitioning between flow cytometry gates. More broadly, these results highlight the ability for automated classification of the drug-induced phenotypes by using machine learning to follow the electrical physiology of patient-derived PDAC cells under drug treatment.

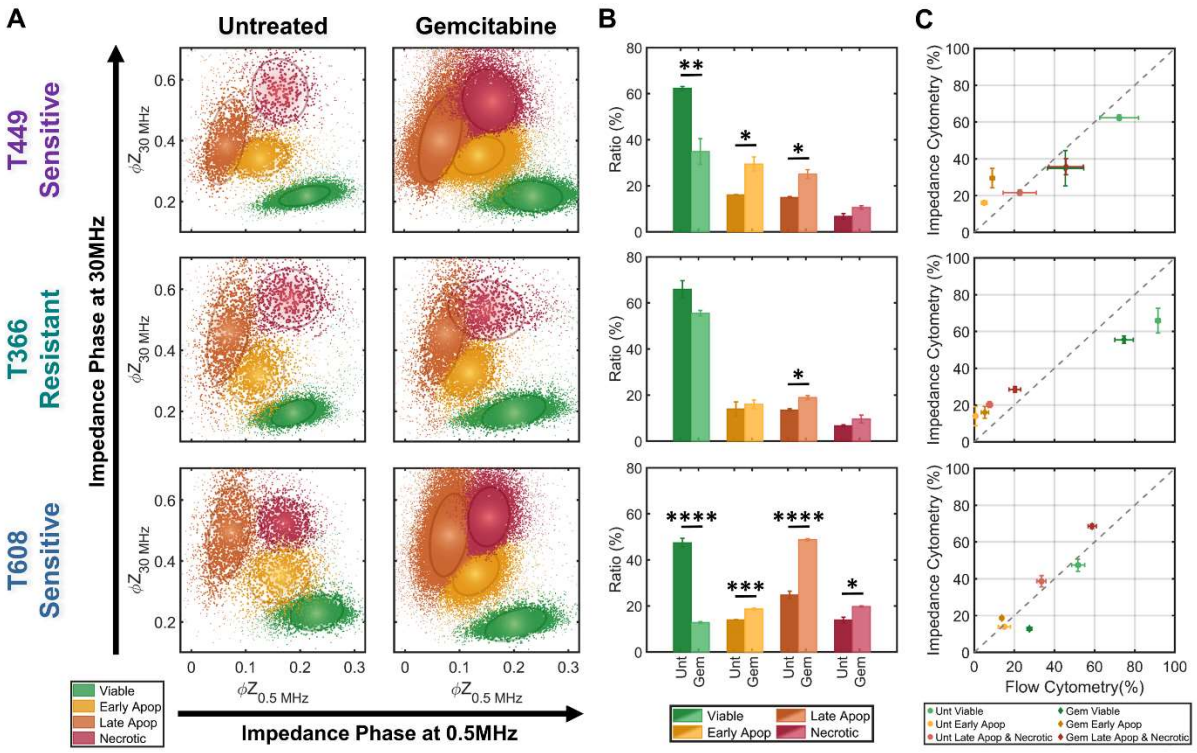

Figure 3.6: *Quantification of subpopulation proportions by supervised learning (KNN method). A - Density scatter plots of impedance phase at 0.5 MHz ($\phi Z_{0.5\ MHz}$) versus impedance phase at 30 MHz ($\phi Z_{30\ MHz}$) for untreated controls and gemcitabine-treated samples for three PDAC cell lines*

*(T449, T366 and T608). The KNN-classified sub-populations are presented: viable (green), early apoptotic (yellow), late apoptotic (orange) and necrotic (red). Ellipses contain 50% of all events per sub-population. B – Ratios for KNN-classified sub-populations for each PDAC cell line (n = 3). Statistical significance: *p ≤ 0.05; **p ≤ 0.01, ***p ≤ 0.001 and ****p ≤ 0.00001. C – Comparison between the estimated subpopulation ratios from flow cytometry versus impedance cytometry for each PDAC cell line (n = 3).*

Classifying the progression of apoptotic stages by impedance metrics

Based on impedance-based identification of the four subpopulations (viable, early apoptotic, late apoptotic, and necrotic) within the gemcitabine treated PDAC samples, we compare each subpopulation across cell lines to delineate the biophysical impedance metrics relevant to their quantification. This is presented for three PDAC cell types of differing gemcitabine sensitivity: T608 (highly sensitive), T449 (moderately sensitive) and T366 (resistant), using the metrics of electrical diameter ($\sqrt[3]{|Z|_{0.5\,MHz}}$) to assess cell size, $\phi Z_{0.5\ \mathrm{MHz}}$ to assess cell membrane state, and $\phi Z_{30\ \mathrm{MHz}}$ to assess internal cellular structure and composition (**Figure 3.7A-C**). To better visualize this comparison, **Figure 3.7D** presents a 3D scatter plot of these impedance metrics for a T608 PDX sample, and **Figure 3.7E** presents a schematic overview of the key phenotypic differences between the subpopulations alongside their associated alterations in impedance metrics. Comparing the necrotic versus viable subpopulations, the reduction in $\phi Z_{0.5\ \mathrm{MH}}$ (**Figure 3.7B**) can be attributed to plasma membrane permeabilization, which causes an increase in conductivity of the cell interior to lead to the observed rise in $\phi Z_{30\ \mathrm{MHz}}$ levels (**Figure 3.7C**), but the known differences in cellular swelling do not cause significant alterations in the estimated electrical diameter of the cells. In fact, single-shell dielectric models (**Figure 3.8**) show that while alterations to the cell size do not result in major changes to the impedance phase of cells (**Figure 3.8B**), the alterations in membrane conductivity (as expected for a compromised plasma membrane) cause clear alterations in $\phi Z_{0.5\ \mathrm{MH}}$ (**Figure 3.8D**), while increases in conductivity of the cell interior (as expected from the uncontrolled intake of ions from the conductive buffer) sharply increase the impedance phase at higher frequencies ($\phi Z_{2\ \mathrm{MH}}$, $\phi Z_{18\ \mathrm{MHz}}$ and $\phi Z_{30\ \mathrm{MH}}$ in **Figure 3.8F**). Considering the apoptotic versus viable subpopulations in the drug-treated samples, statistically significant differences are apparent within all analyzed metrics (**Figure 3.7A-C**). The characteristic formation of membrane blebs under apoptosis would increase the surface area of the

cell and the capacitance alteration can be related to the increase in membrane permittivity. Based on shell-models (**Figure 3.8C**), this increase would increase $\phi Z_{2\ MH}$, while the onset of apoptotic cell shrinkage would reduce $\phi Z_{0.5\ MH}$ (**Figure 3.8B**). Moreover, the start of chromatin condensation and DNA fragmentation, together with Ca^{2+} regulated alterations to the endoplasmic reticulum, would increase the conductivity of the cell interior. This would increase $\phi Z_{2\ MH}$, $\phi Z_{18\ MHz}$ and $\phi Z_{30\ MHz}$ (**Figure 3.8E**), as observed with a good degree of significance (****p<0.0001 & ****p<0.0001, respectively), assuming an intact plasma membrane for apoptotic cells. Furthermore, statistically significant differences in all analyzed metrics are also apparent between subpopulations at the early-stage apoptosis (cross-validated by AV+ZNIR- expression in flow cytometry) versus the late-stage apoptosis (characterized by AV+ZNIR+ expression in flow cytometry, similar to **Figure 3.4iv**). The continuation of the internal fragmentation, including nuclear and organelle degradation, leads to lowering of the insulating intracellular material, thereby causing an increase in internal conductivity that is reflected in a significant increase in $\phi Z_{30\ MHz}$ (**Figure 3.7C**). Furthermore, with the onset of the "secondary necrosis" state during late apoptosis, the plasma membrane becomes progressively permeabilized to lead to alterations similar to those discussed previously for necrosis, i.e., a significant decrease in both $\phi Z_{0.5\ MHz}$ and $\phi Z_{2\ MHz}$ (≤**p<0.01 & ≤**p<0.01, respectively), and a significant increase in $\phi Z_{18\ MHz}$ and $\phi Z_{30\ MHz}$ (≤**p<0.01 & ≤*p<0.05, respectively) due to ion exchange between the intracellular and external media. The transition from early to late apoptosis also leads to the formation and shedding of apoptotic bodies that vary in size, shape and composition during drug-induced cellular disassembly for removing fragmented internal components [26], which would lead to a sharp decrease in cell size, as detected by electrical diameter from our simulations (**Figure 3.8**D) and measured results (**Figure 3.7**A; ≤**p<0.01), especially in comparison to the viable cell subpopulation (≤***p<0.001). Comparing the necrotic and late apoptotic subpopulations, while some phenotypic alterations are common, such as the gradual loss of membrane integrity that leads to significant changes in the impedance metrics, there are also key differences between the two states that can be distinguished based on the machine learning strategies. For instance, the formation of membrane blebs and apoptotic bodies within the late apoptotic subpopulation cause differences in electrical diameter and membrane-related metrics (e.g., $\phi Z_{0.5\ MHz}$, $\phi Z_{2\ MHz}$ or magnitude opacity) versus the necrotic subpopulation.

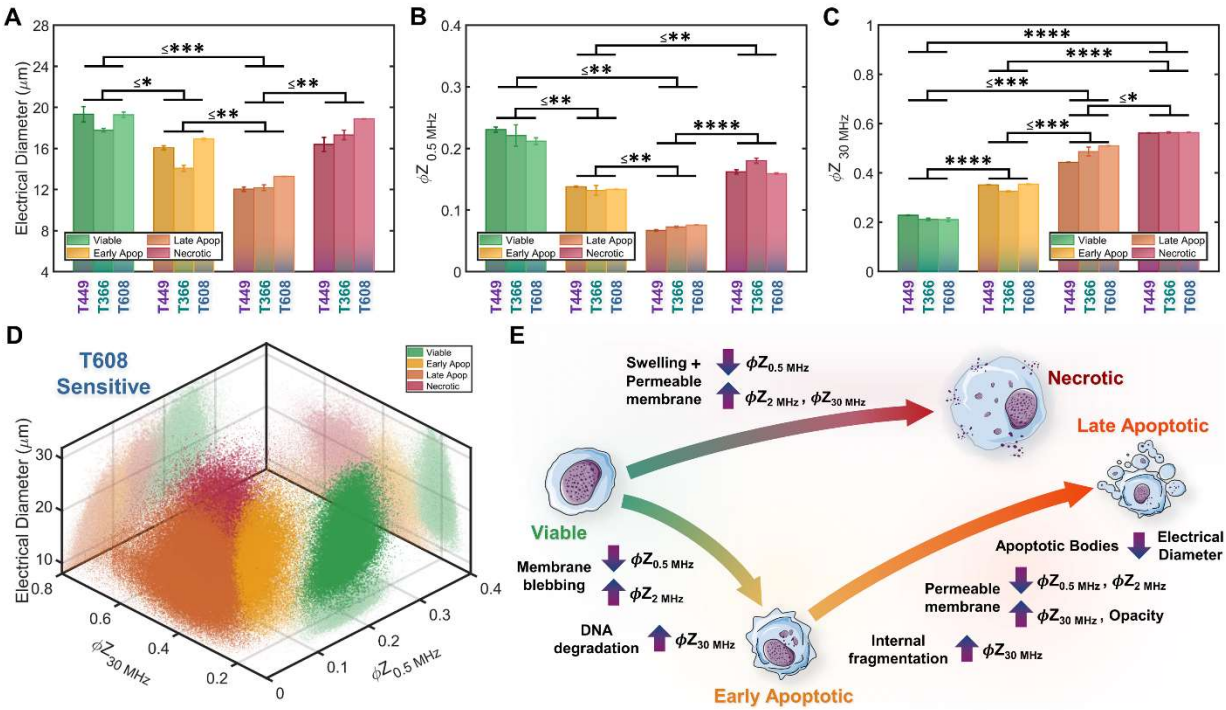

Figure 3.7: *Comparison of biophysical metrics from impedance cytometry: A. Electrical diameter, B. impedance phase at 0.5 MHz ($\phi Z_{0.5\ MHz}$) and C. impedance phase at 30 MHz ($\phi Z_{30\ MHz}$) for each PDAC cell type (n = 3 runs). The biophysical properties of each subpopulation (viable, early apoptotic, late apoptotic, and necrotic) can be identified by characteristic combinations of impedance metrics. Statistical significance is presented as the highest p-value amongst the three cell lines (*p ≤ 0.05, **p ≤ 0.01, ***p ≤ 0.001 and ****p ≤ 0.00001). D – Density scatter plot of impedance phase at 0.5 MHz ($\phi Z_{0.5\ MHz}$) versus impedance phase at 30 MHz ($\phi Z_{30\ MHz}$) versus electrical diameter ($\sqrt[3]{|Z|_{0.5\ MHz}}$)) for a gemcitabine-treated T608 sample. E – Overview of the key biophysical differences between subpopulations and impedance metrics associated with the altered electrical physiology.*

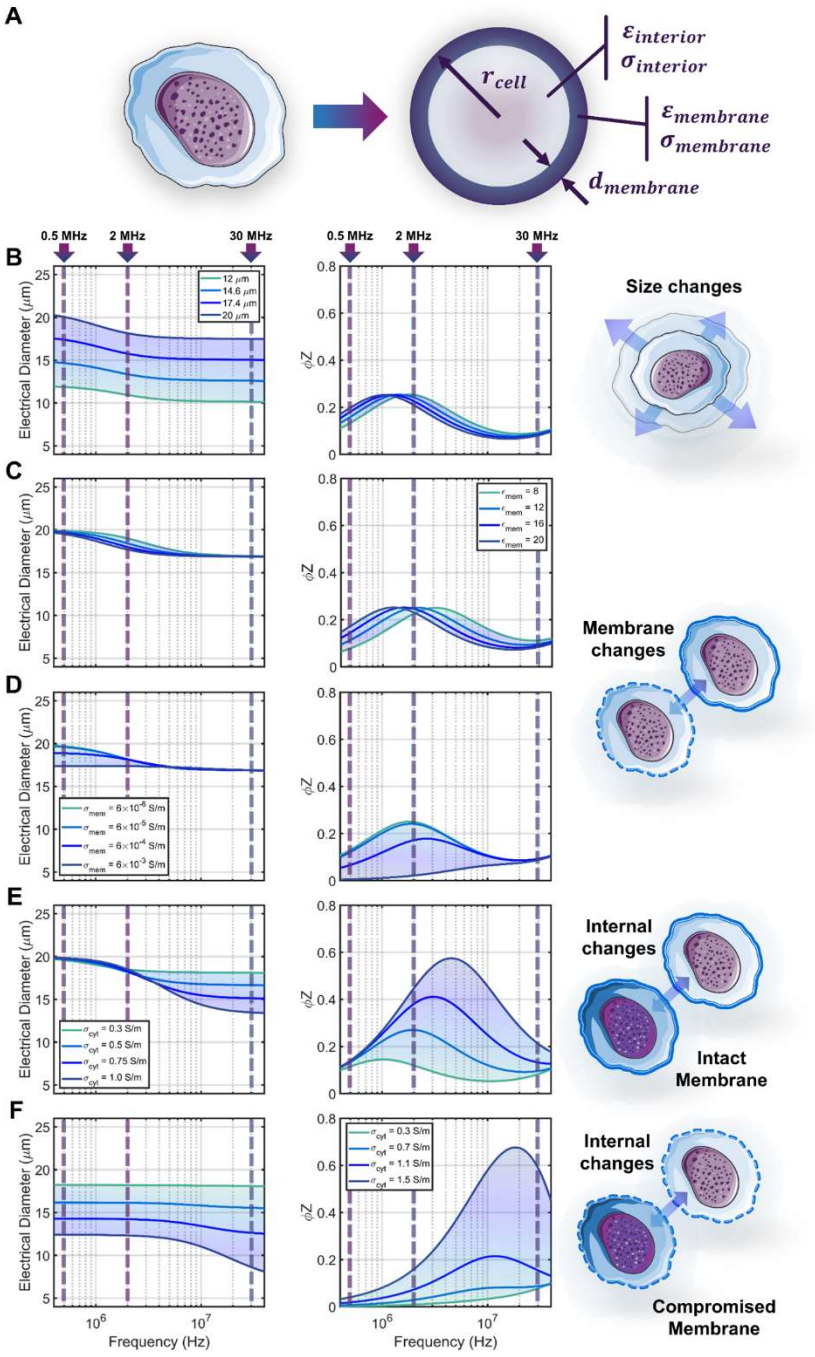

Figure 3.8: *Dielectric shell modelling. A – An equivalent single-shell model of a biological cell in a suspending medium, obtained through Maxwell's mixture theory. Modelled electrical diameter and impedance phase (ϕZ) for a variety of different alterations to the dielectric properties: B – cell size (r_{cell} from 6 to 10 μm), C – membrane permittivity (ε_{mem} from 8 to 20), D – membrane conductivity (σ_{mem} from 6 × 10^{-6} to 6 × 10^{-3}), E – internal conductivity (σ_{int} from 0.3 to 1.0 S/m, assuming ε_{mem} = 14 and σ_{mem} < 1 × 10^{-6} S/m), and F – internal conductivity (σ_{int} from 0.3 to 1.5*

S/m, assuming $\varepsilon_{mem} = 14$ and $\sigma_{mem} = 6 \times 10^{-3}$ S/m). Cells modelled using a single-shell model with the following set of dielectric properties (if not being varied at each individual sub-figure case): $d_{mem} = 10$ nm, $\varepsilon_{mem} = 14$, $\sigma_{mem} < 1 \times 10^{-6}$ S/m, $\varepsilon_{int} = 60$, $\sigma_{int} = 0.5$ S/m, $\varepsilon_{medium} = 80$, $\sigma_{medium} = 1.6$ S/m, $d_{electrode} = 50$ μm, $A_{electrode} = 2.5 \times 10^{-9}$ m^2.

CONCLUSIONS

Modulating drug-induced pancreatic cancer cell death for prevention of an immunosuppressive tumor microenvironment requires single-cell phenotypic analysis tools capable of distinguishing the intensity of apoptosis using drug-treated samples from patient-derived xenograft (PDX) models. Since flow cytometry after standard staining protocols for apoptosis and viability was unable to distinguish cells over the progression of apoptotic states, we consider distinction of cells in the early apoptotic versus late apoptotic and necrotic states based on the biophysical metrics measured by multifrequency impedance cytometry. Machine learning strategies were used to train for recognition of biophysical metrics from each apoptotic phenotype based on positive controls from hypotonic treatment of the pancreatic tumor cells, so that unsupervised learning can enable subpopulation clustering and supervised learning can be applied on gemcitabine treated pancreatic tumor cells to enable classification and pattern prediction. In this manner, the relative intensity of onset of apoptosis under gemcitabine treatment can be distinguished for pancreatic tumors of differing gemcitabine sensitivity based on the cell proportions in the viable, early apoptotic, late apoptotic, and necrotic states. In comparison to viable cells, those in the early apoptotic state exhibit lowered electrical diameter levels due to cell shrinkage, lowered impedance phase at low frequency ($\phi Z_{0.5\ \mathrm{MHz}}$) due to membrane blebbing and a rise in impedance phase at high frequency ($\phi Z_{30\ \mathrm{MHz}}$) due to alterations at the cell interior, such as Ca^{2+} regulated alterations to the endoplasmic reticulum, chromatin condensation and DNA fragmentation. Late apoptotic cells exhibit even sharper drops in electrical diameter and impedance phase at low frequency ($\phi Z_{0.5\ \mathrm{MHz}}$) versus viable and early apoptotic cells, while continuing to exhibit a rise in impedance phase at high frequency ($\phi Z_{30\ \mathrm{MHz}}$). On the other hand, cells at the necrotic state are distinguished from all other phenotypic states based on their much higher impedance phase at high frequency ($\phi Z_{30\ \mathrm{MHz}}$), likely due to uncontrolled ion uptake to the cell interior. Interestingly, the onset of late apoptosis versus early apoptotic and necrotic states can be distinguished by impedance metrics, whereas this was not possible by flow cytometry after the

standard staining protocols. Upon application of these methods to quantify subpopulations after gemcitabine treatment of pancreatic tumor PDXs, we find cells chiefly at the late apoptotic state for the highly drug-sensitive cell types (T608), distributed over the early and late apoptotic state for the moderately drug-sensitive cell types (T449), and for the drug-resistance cell type (T366), the cells remain predominantly viable, with a small proportion detected at the late apoptotic state. This ability to automate phenotypic classification by machine learning strategies, as applied here towards quantifying intensity of apoptosis for modulating drug-induced pancreatic cancer cell death, can form the foundation for future studies with heterogeneous drug-treated samples from multicellular tumor models.

Chapter 3: Supervised learning to distinguish drug-induced transformations of pancreatic cancer cells versus the associated fibroblasts in the tumor microenvironment

The interaction of cancer and cancer associated fibroblasts (CAFs) in the tumor microenvironment results the emergence of drug-resistance of tumors to chemotherapies, which hampers the development of effective chemotherapies to treat cancer. Consequently, there is a tremendous interest in developing methods to quantify drug sensitivity in heterogeneous samples of pancreatic cancer and stromal cells. The availability of tools to indicate the emergence of drug resistance during longitudinal studies on pancreatic cancer cells under their interaction with cancer associated cells in the Tumor Micro Environment (TME), would advance the ability to screen therapies that target this cell-cell interaction, using relevant in vitro models of the TME, which would result in more effective chemotherapies. The value of developing new methods become more evident, considering that distinction of drug sensitivity of cancer versus stromal cells is often not possible purely by EpCAM (epithelial cell adhesion molecule) staining, since the EpCAM expression level of cancer cells can differ for various subpopulations. This suggests a need for developing new methods to quantify and distinguish cancer cells and CAFs. In this chapter we develop a novel supervised machine learning (ML) approach that utilizes the multiple impedance metrics obtained from single-cell cytometry conducted at several simultaneously applied frequencies to distinguish the biophysical properties of co-cultured viable cancer cells and CAFs, in absence and in presence of drug treatment. By employing supervised ML and the measured impendence data, we build models to classify the drug resistant subpopulation within longitudinal studies and isolate them for downstream molecular analysis.

Introduction

The development of chemotherapies to treat cancer is severely hampered by the inefficiency of translating pre-clinical studies into clinical benefit [70, 71]. A great majority (>95%) of oncology drugs that progress through pre-clinical studies fail during human trials [72], highlighting the critical need to improve the accuracy of evaluating pre-clinical drug efficacy based on physiologically-relevant human models. This is especially critical for pancreatic cancer, the third leading cause of cancer deaths, with a 5-year survival rate of <6% [65-67]. No solid tumor is as quickly and inescapably fatal as pancreatic ductal adenocarcinoma (PDAC) [64], which comprises 95% of pancreatic cancers. Intra-tumoral heterogeneity, as created by the interaction and re-programming of cancer and cancer associated cells in the tumor microenvironment (TME), is implicated in the emergence of drug-resistance of tumors to chemotherapies [104]. The availability of cellular and molecular-level markers to indicate the emergence of drug resistance during longitudinal studies on pancreatic cancer cells under their interaction with cancer associated cells in the TME, would advance the ability to screen therapies that target this cell-cell interaction, using relevant in vitro models of the TME [105].

Recapitulating the TME is challenging [106], leading to in vitro tumor models based on spheroids or organoids; PDAC derived from murine and human-induced pluripotent stem cells; and other novel ex vivo systems [107]. These have shown some promise in identifying molecular pathways that correlate with disease progression and for development of drug screens [108-110], by using imaging or cytometry methods to unravel reprogramming due to cell-cell interactions and transcriptomics for single-cell molecular analysis. However, imaging and cytometry methods require fluorescent staining for specificity. This is not compatible with longitudinal studies that aim to repeatedly drug-treat the same sample set to identify the emergence of drug resistance within a subpopulation of viable cancer cells, since the stained sample for analysis after each drug treatment step cannot be included within subsequent drug treatment steps. This is especially problematic for longitudinal analysis conducted with patient-derived tumor biopsies that have limited cell numbers, and the markers to stain for cellular transformations are often unknown. To advance transcriptomic [111] studies aimed at discovering molecular markers of drug resistance with patient-derived biopsies, there is a need for label-free monitoring tools capable of probing the cellular interactions and drug-induced transformations in the TME, for identifying resistant

subpopulations and enabling their selective isolation for spatially resolved transcriptomic information in the TME.

In this chapter, we seek to identify the cellular biophysical properties of the drug resistant pancreatic cancer cell subpopulation using conditions that simulate the emergence of drug resistance in the TME, such as the interaction of pancreatic cancer cells with cancer associated fibroblasts (CAFs). Specifically, we use cancer cells and CAFs that are obtained from patient-derived xenografts (T608), which are highly sensitive to gemcitabine treatment under monoculture but progressively lose drug-sensitivity under co-culture, thereby simulating the cell-cell interactions that lead to the emergence of drug resistance in the TME. For label-free identification of the phenotype of the subpopulation of viable cancer cells and CAFs after drug-treatment under co-culture, we utilize impedance cytometry to identify the biophysical hallmarks of the drug-resistant cancer cell subpopulation. However, since the biophysical properties of T608 cancer cells and CAFs exhibit only small differences yet significant over several subcellular features, there is a need to develop multivariate methods that can distinguish the respective cell types within their single-cell impedance data clusters. For this purpose, we develop a novel supervised machine learning (ML) approach that utilizes the multiple impedance metrics obtained from single-cell cytometry conducted at several simultaneously applied frequencies to distinguish the biophysical properties of co-cultured viable cancer cells and CAFs, in absence and in presence of drug treatment. In this manner, viable cancer cells that exhibit systematic biophysical differences after drug treatment in co-cultures with CAFs, due to characteristic size, membrane capacitance and interior cytoplasmic conductivity, can be used with the supervised ML model to classify the drug resistant subpopulation within longitudinal studies and isolate them for downstream molecular analysis.

Materials and Methods

Patient-Derived Pancreatic Tumor Xenografts and Cells

PDAC tumor and cancer associated fibroblast (CAFs) samples were generated from remnant human tumor surgical pathology specimens collected in collaboration with the University of Virginia Biorepository and Tissue Research Facility, and with the approval of the University of Virginia Institutional Review Board for Health Sciences Research following written informed consent from each patient. Tumors and CAFs were propagated orthotopically on the pancreata of immunocompromised mice. Tumor and CAFs growth characteristics were measured, samples were collected for genotyping, and xenograft lines were established. Cells were transduced with firefly luciferase lentivirus (KeraFAST), selected using puromycin and maintained in RPMI 1640 (Thermo Fisher Scientific) with 10% FBS (Gemini Bioproducts) and 2 mM glutamine (complete medium), with fresh aliquots thawed, propagated, and used for experiments.

Gemcitabine Treatments

Monoculture: T608 cancer cells, were exposed to 1 μg/mL of gemcitabine (University of Virginia clinical pharmacy) for 48 h in complete medium, with control samples being kept under the same time periods. Conditioned medium: monoculture T608 CAFs were treated with 1 μg/mL of gemcitabine and after 12 h, the supernatant was collected, centrifuged, filtered, and then added to monoculture T608 cancer cells. Then cancer cells were exposed to 1 μg/mL of gemcitabine for 48 hr. For the untreated cancer cell, the supernatant from untreated CAFs was collected, centrifuged, filtered, and then added to monoculture cancer cells. Transwell co-culture: T608 cancer cells in the bottom and T608 CAFs on top were separated in a transwell culture with 1 μm inserts were exposed to 1 μg/mL of gemcitabine for 48 h in complete medium. Control samples were kept under the same time periods. Direct co-culture: co-culture sample of T608 cancer cells and T608 CAFs were exposed to 1 μg/mL of gemcitabine for 48 h in complete medium, with control samples being kept under the same time periods.

Sample Preparation

Cell culture media, i.e., RPMI 1640 with 10% FBS and 2 mM glutamine (complete medium), Thermo Fisher Scientific, post gemcitabine treatments, were first aspirated and stored, with the

remaining adherent cells being washed in 1×PBS (Thermo Fisher) and exposed to 0.5% trypsin in 1×PBS for 5 min at 37 ˚C. In order to retrieve both the adherent and non-adherent cells fractions, both the aspirated cell culture medium and trypsinized cells were re-suspended into a total volume of 5 mL DMEM with 10% FBS and 1% pen-strep (Thermo Fisher) and centrifuged at 300 g for 10 min. This sample was then aspirated, the cell pellet (containing both adherent and non-adherent cells) was re-suspended in 1xPBS, 500 mM EDTA (Fisher Scientific), and 0.5% Bovine Serum Albumin (Sigma Aldrich) and filtered through a 100 μm cell strainer. Cells were then counted with a hemocytometer and ~300,000 cells from each sample were then analyzed for flow and impedance cytometry measurements concurrently.

Flow Cytometry

After sample preparation, samples were stained with Annexin V (Thermo Fisher Scientific), Zombie NIRTM (or ZNIR; APC-A750, Biolegend), and EpCAM and immediately analyzed. Flow cytometry was carried out using a CytoFLEX flow cytometer (Beckman Coulter), with data being analyzed using CytExpress (Beckman Coulter). The cell population was first gated based on forward (FSC) versus side (SSC) scatter data, to gate events that were too small to be considered cells; and then gated based on SSC Area versus Height, to gate out doublets events. Data from the FITC and APC-A750 filters were then used to plot the expression of Annexin V and ZNIR, respectively, with cells being gated according to their viability status.

Impedance Cytometry

For impedance cytometry, A syringe pump was used to introduce cells, with co-flowing 7 μm polystyrene beads (Sigma) at ~1.2 x 10^5 beads/mL into the microchannel with patterned electrodes for a detection region 50 μm (width) × 50 μm (height), for measurement at four simultaneous frequencies (0.5, 2, 30 MHz and a probe frequency that is swept in the 2 to 20 MHz range) using an impedance analyzer (Amphasys AG, Switzerland). Acquisition settings were optimized for signal to noise, based on levels of signal modulation, amplification, demodulation the trigger voltage level. Processed signal data were stored as impedance magnitude and phase, exported as CSV files, and processed with custom code written in Python.

Impedance Data Processing and Statistical Analysis

The impedance phase and magnitude of individual cells were normalized by division to those obtained for polystyrene beads to account for any temporal variations during the measurement and to enable quantitative comparison between measurement. Due to normalization, impedance phase is reported in arbitrary units (with respect to impedance phase of beads indexed at zero). Then individual cells populations were gated from reference beads in normalized impedance data at 30 MHz for analyzing the gated cells at each probe frequency (0.5-30 MHz).

All statistical analysis was performed using a custom script in Python. Significance level was defined as $p < 0.05$. Comparisons between any two groups were done using a student's two-tailed t-test. All results are representative of at least three repetitions; with error bars indicating standard deviation between sample triplicates.

Results

Loss of drug sensitivity of pancreatic cancer cells under co-culture with CAFs

PDAC cancer cells and CAFs that are obtained through surgical resection from a patient with pancreatic cancer are propagated in a mouse xenograft as cancer and CAF lines (**Figure 4.1A**). Using the T608 patient line, these cell types are then treated with gemcitabine (1 μg/mL for 48 h), which is known to cause drug-induced apoptosis within monocultures [26] (**Figure 4.1Bi**), but our intent is to explore the cellular phenotypic transformations under co-cultures with CAFs using conditioned media (**Figure 4.1Bii**), transwell plates (**Figure 4.1Biii**) and direct multicellular culture (**Figure 4.1Biv**). The conditioned media transfers secreted bodies from the CAFs over the full range of sizes at the 48-h timepoint wherein the culture is conformal, to the cancer cell culture under drug treatment. The transwell plate culture enables continuous interaction of the secreted factors in the sub-1 μm range over the entire 48 h co-culture period of the drug treatment and the direct co-culture additionally includes the proximal cell-cell interaction cues over the 48-h co-culture period during drug treatment. Our results in **Figure 4.1C** show that while the T608 cancer cells under monoculture exhibit large drops in cell viability under gemcitabine treatment (1 μg/mL for 48 h), there is a steady rise in the subpopulation of viable cancer cells under similar treatment conditions that include CAF factors under conditioned media, transwell and direct co-culture to simulate the intercellular interactions in the TME. For these studies, the effect of gemcitabine on

each cell culture type was measured by flow cytometry to classify and compare percentage of the remaining viable population, using Annexin V to stain apoptotic cells and Zombie Near-Infrared (ZNIR) to stain other non-viable cells (late apoptotic and necrotic), so that the AV- ZNIR- events can be quantified as viable cells.

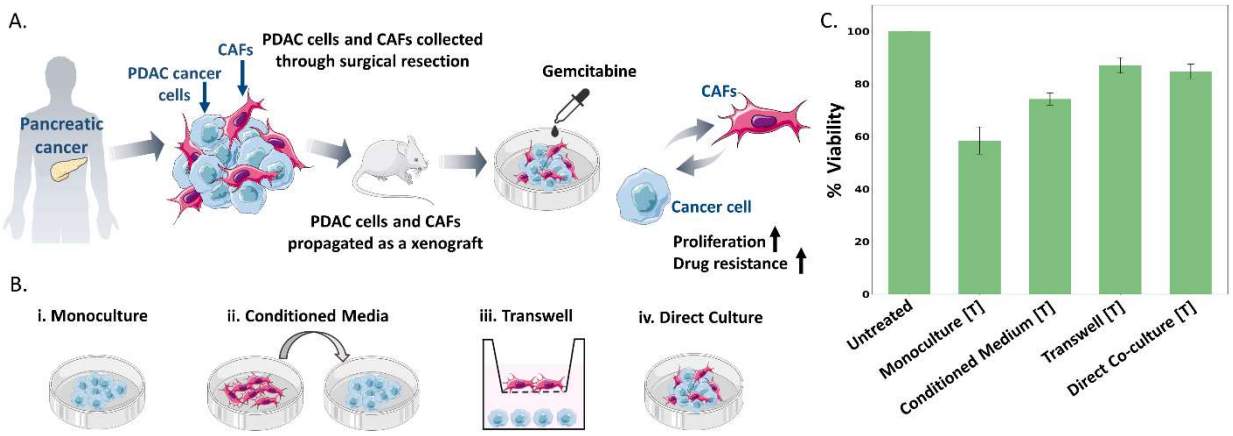

Figure 4.1: *Experimental design (A-B) to study the emergence of drug resistance in T608 cancer cells under co-culture with T608 CAFs, as apparent from the progressive increase in viable cancer cell subpopulation after gemcitabine treatment (1 µg/mL for 48 h) (C).*

Quantification of viable cells can also be accomplished in a label-free manner by impedance cytometry, since non-viable cells with compromised plasma membranes show a low level of impedance phase at low frequencies (e.g., 0.5 MHz) due to electric field penetration through the cell membrane region and a high level of impedance phase at high frequencies (e.g., 18 MHz) due to conductive cell interior regions arising from penetration of the PBS media in absence of phagocytosis within in vitro cultures. This permits delineation of the viable versus non-viable gate based on impedance cytometry, as shown in **Figure 4.2A**. Based on this, quantification of the viable cell subpopulation from impedance cytometry compares well versus the flow cytometry approach based on the AV- ZNIR- events (**Figure 4.2B**), thereby validating application of this label-free approach based on biophysical hallmarks of viable cells.

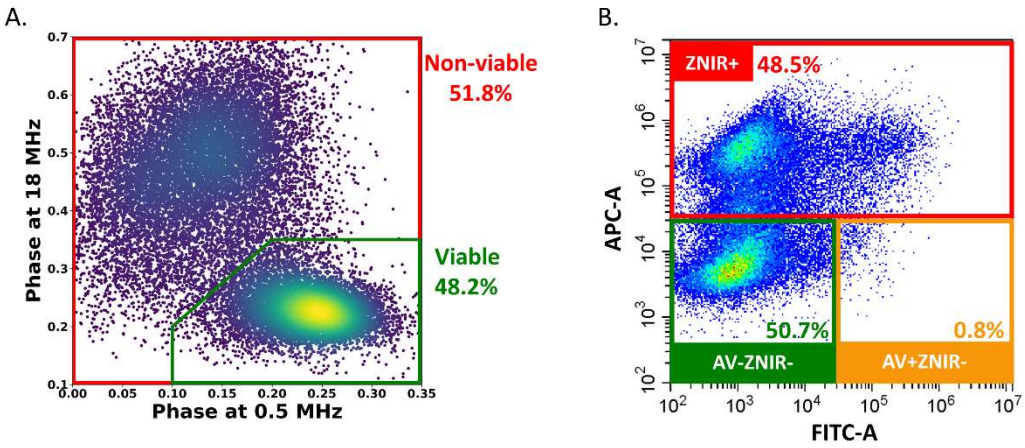

Figure 4.2: *The viable cell subpopulation after drug treatment that is quantified by: A. impedance cytometry based on the gate with low impedance phase at 0.5 MHz ($\phi Z_{0.5\ MHz}$) and high impedance phase at 18 MHz ($\phi Z_{18\ MHz}$) compares well with determination by: B. flow cytometry after fluorescent staining based on the AV- ZNIR- events.*

Impedance metrics to identify biophysical hallmarks of the drug-resistant subpopulation

The progressive increase in the viable cell subpopulation within multicellular cancer cell cultures that include factors from CAFs (**Figure 4.1C**) is consistent with prior work [112] indicating that drug treatment of multicellular cancer cell and CAF cultures reprograms the cancer cells to contribute to tumor cell proliferation, invasion, and metastasis via secretion of various growth factors, cytokines, and chemokines, all of which lead to the emergence of drug resistant phenotypes [113]. Hence, by gating the viable cell subpopulation using impedance cytometry, we seek to quantify the biophysical hallmarks of the viable cancer cells after drug treatment, so that these properties can eventually be used to identify this drug resistant subpopulation in multicellular tumors. **Figure 4.3** compares the biophysical properties of the gated viable cancer cells obtained from cultures of untreated versus drug-treated (1 μg/mL gemcitabine for 48 hours) samples, including the monoculture (**Figure 4.3A-D**), transwell plate culture (**Figure 4.3E-H**) and combination of the respective plots (**Figure 4.3I-L**). The respective comparisons are based on normalized histograms (10,000 cell events) of impedance magnitude opacity ($\frac{|Z|_{2\ MHz}}{|Z|_{0.5\ MHz}}$), impedance phase at 18 MHz ($\phi Z_{18\ MHz}$) and 2 MHz ($\phi Z_{2\ MHz}$), electrical diameter ($\sqrt[3]{|Z|_{0.5\ \mathrm{MHz}}}$) (**Figure 4.3C, G and L**) and forward scattering flow cytometry (FSC) events (**Figure 4.3D and**

H) . Considering drug treated cancer cell monocultures, the remaining viable cancer cells show clear alterations in electrical physiology with respect to viable cells in absence of the drug, based on clear upward shift in the opacity level at 2 MHz (**Figure 4.3A**), downward shift in the $\phi Z_{18\,MHz}$ level (**Figure 4.3B**), and upward shift in the electrical diameter (**Figure 4.3C**), with the latter validated by FSC results (**Figure 4.3D**). Similar trends are apparent under the transwell condition for the remaining viable cells of the untreated versus drug-treated cancer cells, albeit with lower levels of shift versus the monoculture condition in terms of opacity (**Figure 4.3E**), $\phi Z_{18\,MHz}$ (**Figure 4.3F**), electrical diameter (**Figure 4.3G**) and FSC events (**Figure 4.3H**). Based on the combined plots (**Figure 4.3I-L**), the viable cancer cells under the untreated monoculture condition (dashed green) significantly differ in electrical physiology from the remaining viable cancer cells under each of the studied conditions, including under untreated transwell culture (dashed blue), drug-treated monoculture (red line) and drug-treated transwell culture (black line) based on the metrics of opacity (**Figure 4.3I**), $\phi Z_{2\,MHz}$ (**Figure 4.3J**), $\phi Z_{18\,MHz}$ (**Figure 4.3K**), and electrical diameter (**Figure 4.3L**). In each case, the respective metrics of viable cancer cells in the untreated monoculture (dashed green) show a gradual shift under interaction with CAFs in the transwell co-culture system without drug-treatment (dashed blue) and this shift is then successively enhanced upon drug treatment (solid red and solid black), with very minor differences between the viable cells after drug treatment within the monoculture versus trans-well culture system. Based on this trend of shifts within the respective impedance metrics, we suggest that the biophysical properties of viable cancer cells in the untreated monoculture (dashed green) are altered upon interaction of cancer cells with CAFs in the untreated transwell system, thereby creating an altered biophysical phenotype for the viable cancer cells (dashed blue) that resemble the drug resistant subpopulation following drug treatment (black line and red line). This highlights the need to identify viable cancer cells based on their biophysical properties from multicellular samples that include CAFs, under conditions that exclude and include drug-treatment to enable correlations to the drug resistant phenotype.

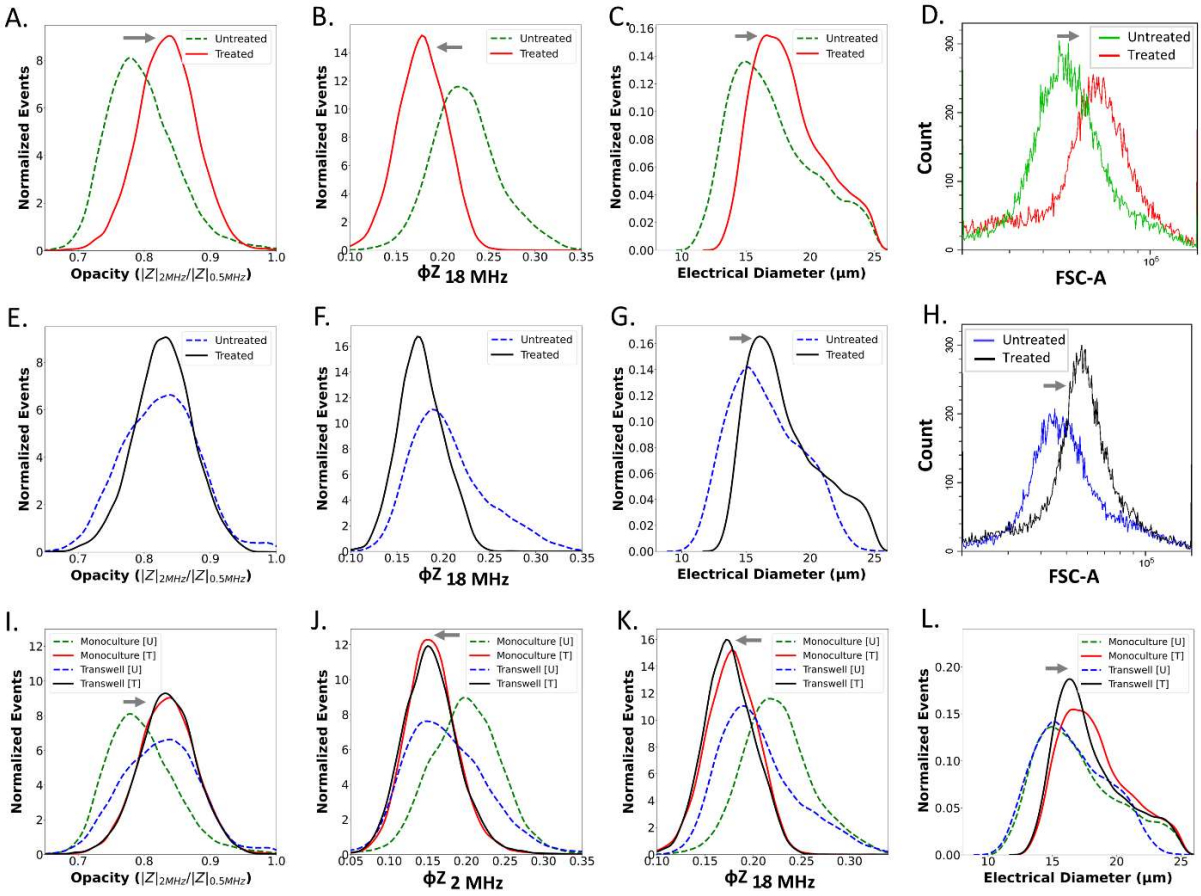

Figure 4.3: *The biophysical properties of viable T608 cancer cells from cultures untreated versus drug-treated (1 μg/mL gemcitabine for 48 hours) samples are compared, including conditions of monoculture (A-D), culture in a transwell plate (E-H), and by combining the respective plots (I-L). The respective comparisons are shown for normalized histograms (10,000 cell events) of impedance magnitude opacity ($\frac{|Z|_{2\ MHz}}{|Z|_{0.5\ MHz}}$) (A, E & I), impedance phase at 18 MHz ($\phi Z_{18\ MHz}$) (B, F & K) and 2 MHz ($\phi Z_{2\ MHz}$) (J), electrical diameter ($\sqrt[3]{|Z|_{0.5\ MHz}}$) (C, G & L) and forward scattering flow cytometry (FSC) events (D & H).*

Gating approaches to classify impedance data from heterogeneous samples

The impedance magnitude and phase metrics of untreated cancer cells and CAFs were measured at multiple frequencies from transwell co-cultures of the respective cell types to identify metrics that could be used to distinguish them from within multicellular tumor samples. Example histograms (**Figure 4.4A-E**), significance plots (**Figure 4.4F-I**) and frequency dispersions (**Figure**

4.4J) of respective cell types are shown for the metrics of $\phi Z_{\,0.5\,MHz}$, opacity ($\frac{|Z|_{\,2\,MHz}}{|Z|_{\,0.5\,MHz}}$), $\phi Z_{\,18\,MHz}$, electrical diameter ($\sqrt[3]{|Z|_{0.5\,\mathrm{MHz}}}$) and FSC (flow cytometry).

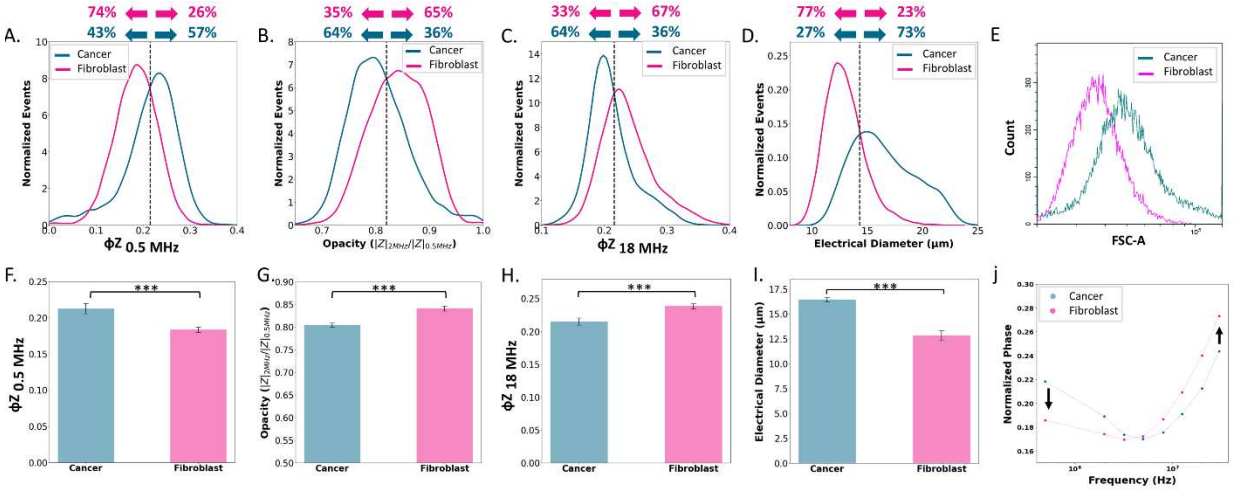

Figure 4.4: *Impedance metrics of cancer cells versus CAFs (fibroblast) after 48 h co-culture to simulate the multicellular tumor prior to drug treatment. The metrics of* $\phi Z_{\,0.5\,MHz}$*, opacity* ($\frac{|Z|_{\,2\,MHz}}{|Z|_{\,0.5\,MHz}}$)*,* $\phi Z_{\,18\,MHz}$*, electrical diameter* ($\sqrt[3]{|Z|_{0.5\,MHz}}$) *and FSC (flow cytometry) are shown as normalized histograms for ~10,000 cell events (A-E) and significance plots from triplicate samples (F-I), as well as based on their multifrequency impedance phase dispersions. For each impedance metric, the proportion of cells on either side of the indicated gate (black dashed line) to separate the respective cell types is indicated (A-D).*

At lower frequencies (0.5 MHz) wherein cell membrane screening by the applied electric field influences the impedance response, fibroblasts exhibit a lower range of ϕZ levels in comparison to those of cancer cells (**Figure 4.4A and F**). On the other hand, at higher frequencies (18 MHz) wherein properties of the cell interior dominate due to electric field passage through the cell membrane to the cytoplasm, the separation in ϕZ levels is in the opposite direction (**Figure 4.4C and H**). This is also apparent based on the frequency dispersion (**Figure 4.4J**). Similarly, differences in impedance magnitude based on opacity at 2 MHz (**Figure 4.4B and G**) and electrical diameter (**Figure 4.4D and I**) are also indicated, with the latter validated based on FSC events from flow cytometry (**Figure 4.4E**). Based on the frequency dispersions of the measured metrics for cancer cells and CAFs, a single-shell model can be constructed to identify the distinguishing biophysical properties. The summarized data from the fits in **Table 4.1** indicates that the major

differences between the respective cell types arise due to cell radius, with additional differences arising due to differing membrane capacitance, and only minor differences in conductivity of the cell interior.

Table 4.1: Dielectric properties of cancer cells vs. CAFs based on fitting of their impedance spectra to a single-shell model. Model fitting parameters: membrane thickness (d_{mem})= 10 nm, membrane conductivity (σ_{mem}) = 1×10^{-8} S/m, cytoplasm permittivity (ε_{int}) = 80, Bead conductivity = 2.7×10^{-3} S/m, Bead permittivity = 2.5, Bead radius (r_{Bead}) = 3.5 µm, medium conductivity (σ_{medium}) = 1.6 S/m, medium permittivity (ε_{medium}) = 80.

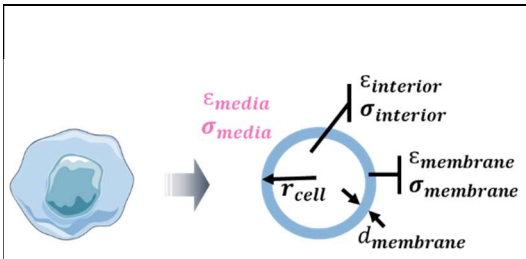	**Cell type**	**Membrane capacitance ($C_{membrane}$) [mF/m^2]**	**Interior conductivity ($\sigma_{cytoplasm}$) [S/m]**	**Cell radius (r_{cell}) [µm]**
	Cancer cells	7.43	0.51	8.5
	CAFs	9.21	0.46	6.6

While the respective impedance metrics exhibit statistically significant differences (***p<0.001) that can possibly be used for the distinction of cancer cells versus CAFs based on electrical physiology, as presented within the shell model of their dielectric properties in **Table 4.1**, the histogram distributions from single-cell data indicate a good degree of overlap. This would impede the ability to accurately quantify the respective cell types from multicellular samples using set gates on a particular set of impedance metrics, as apparent from the large proportion of cells that are not classified in the appropriate category (cancer cells vs. CAFs) based on the indicated manual 1D gate (black dashed line) to separate the respective cell types (the % cells within each gate are indicated at the top of **Figure 4.4A-D**). For instance, based on the indicated 1D gate for $\phi Z_{\,0.5\,MHz}$, (**Figure 4.4A**), only 57% of cancer cells would be accurately distinguished, with the region also including 26% CAFs, and the same gate would accurately distinguish only 74% of the CAFs, with the gate also including 43% cancer cells. Similar arguments apply to the other indicated metrics to highlight the limited classification accuracy of such 1D gates, as well as to 2D gates, as described in **Figure 4.5**.

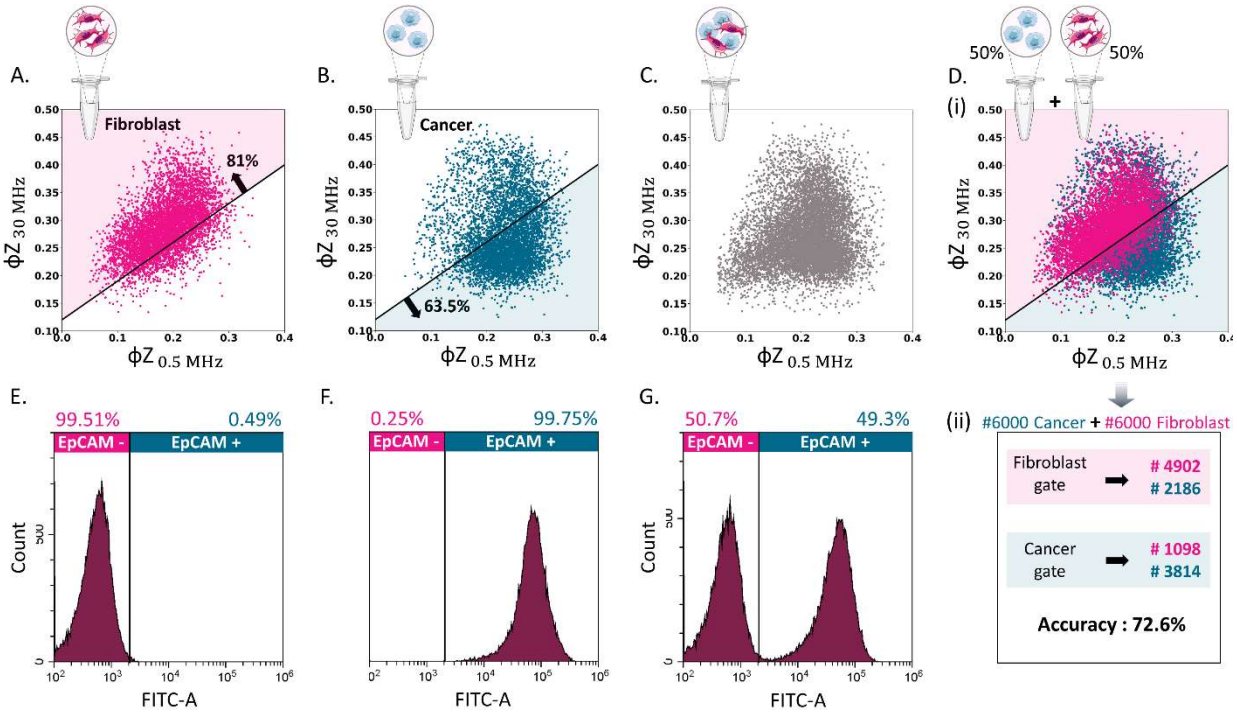

Figure 4.5: *Impedance cytometry analysis displays scatter plot of phase at 30 MHz vs phase at 0.5 MHz for: A. homogeneous sample of CAFs with a 2D gates to separate CAFs (pink shaded area); B. homogeneous sample of cancer cells with a 2D gates to separate cancer cell (blue shaded area); C. heterogeneous sample that impedance cytometry is not able to classify due to the high level of overlap; D.(i) synthetic heterogeneous sample that generated based on 50% cancer cells and 50% CAFs, and the same 2D gates applied to separate the respective cell types (blue shaded area and pink shaded area); D.(ii) based on the 2D gates, 2186 cancer cells are misclassified as CAFs in the pink shaded area, and 1098 CAFs are misclassified as cancer cells in the blue shaded area, thereby giving an accuracy of 72.6%. Flow cytometry after EpCAM staining of: E. homogeneous sample of CAFs; F. homogeneous sample of cancer cells; G. heterogeneous sample that EpCAM is able to classify as 50.7% cancer cells and 49.3% CAFs.*

In Flow cytometry Epithelial Cell Adhesion Molecule (EpCAM), which is a well-established marker for cancer cells, can distinguish the cancer cells vs fibroblast. In a homogeneous sample of CAFs (**Figure 4.5E)** 99.5% of the cells are EpCAM negative and in a homogeneous sample of cancer cells (**Figure 4.5F**) 99.7% of cells are EpCAM positive. Hence, in a heterogeneous sample (**Figure 4.5G**), flow cytometry can classify cancer cells vs CAFs. While for the same

heterogeneous sample, impedance cytometry is not able to distinguish cell types due to the high level of overlap in their impedance metrics (**Figure 4.5C**).

An optimal 2D gate is used to classify homogeneous samples of CAFs in **Figure 4.5A** (pink shaded area) and cancer cells in **Figure 4.5B** (blue shaded area). Then this gate was applied to a synthetic heterogeneous sample that was generated with 50% cancer cells and 50% CAFs (**Figure 4.5D.i**). This gate misclassifies 2186 cancer cells as CAFs (pink shaded area) and misclassifies 1098 CAFs as cancer cells (blue shaded area), thereby giving an accuracy of 72.6% (**Figure 4.5D.ii**). This motivates our exploration of supervised machine learning methods to accurately classify multicellular tumor samples composed of cancer cells and CAFs, using the respective cell types from a transwell culture as training data sets (**Figure 4.6**). In this approach, following transwell co-culture, enables facile cell separation for impedance cytometry of CAFs and cancer cells. Homogeneous samples of cancer cells and CAFs were analyzed by impedance cytometry, then their 12-impedance metrics, including impedance magnitude (|Z|) at 0.5, 2, 18 and 30 MHz; impedance phase (ϕZ) at 0.5, 2, 18 and 30 MHz; electrical diameter; opacity at 2, 18 and 30 MHz, are used to train and test a supervised machine learning model. This model can subsequently be applied to any multicellular tumor to recognize the data points corresponding to each cell type (**Figure 4.6C**). This procedure can subsequently be carried out for drug treated PDAC samples.

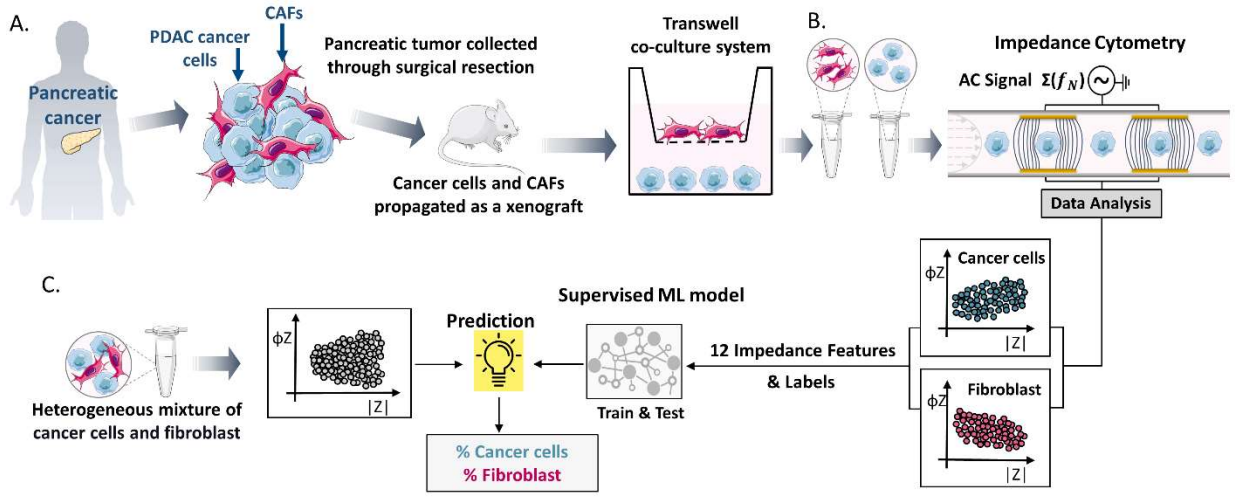

Figure 4.6: *Schematics of the process of developing a predictive model to distinguish cancer versus CAFs in homogeneous samples. A. The patient derived pancreatic tumor is propagated as a xenograft to allow for expansion of cancer cells and CAFs. B. After transwell co-culture in absence of drug treatment, the respective cell types are separated and analyzed by impedance*

cytometry. C. This data is used as the training set to construct a supervised machine learning model for application towards classifying impedance data from multicellular tumor samples.

Supervised learning to distinguish untreated multicellular tumors of cancer cells and CAFs based on impedance metrics

In this manner, impedance data from cancer cells and CAFs obtained from 4 different transwells are merged to make a more realistic data set for training and testing different machine learning (ML) models (**Figure 4.7C**), using 12 different impedance features and 14000 data points per cell type for training. Since these impedance features have different ranges, we scaled them prior to feeding them to ML models for standardization. Next, we trained different models (**Fig. Figure 4.7D**: Logistic Regression, Decision Tree, AdaBoost, Support vector machine, k nearest neighbor, and Gaussian Naive Bayes) to classify the cancer cells and fibroblast. Each potential model is validated using a stratified 5-fold cross-validation (CV) approach to ensure that the different cell lines are similarly represented in each fold. We used the accuracy of predictions to compare the different models, which ranged from 84 to 94%. Among different models, the support vector machine model (SVM) achieved the highest accuracy in predicting the appropriate cell type (93.7%). In the SVM algorithm, the model aims to find the hyperplane in the n-dimensional feature space that best separates the two classes. The high accuracy of the SVM algorithm can be confirmed by analyzing its confusion matrix (**Figure 4.7E**). In this matrix, it is possible to observe what were the predicted classes from the model versus the true classes. The model correctly classified most of the cancer cells and CAFs. This capability of the trained SVM model to identify cancer and CAFs with high accuracy gives us the confidence to use the model for any heterogeneous samples.

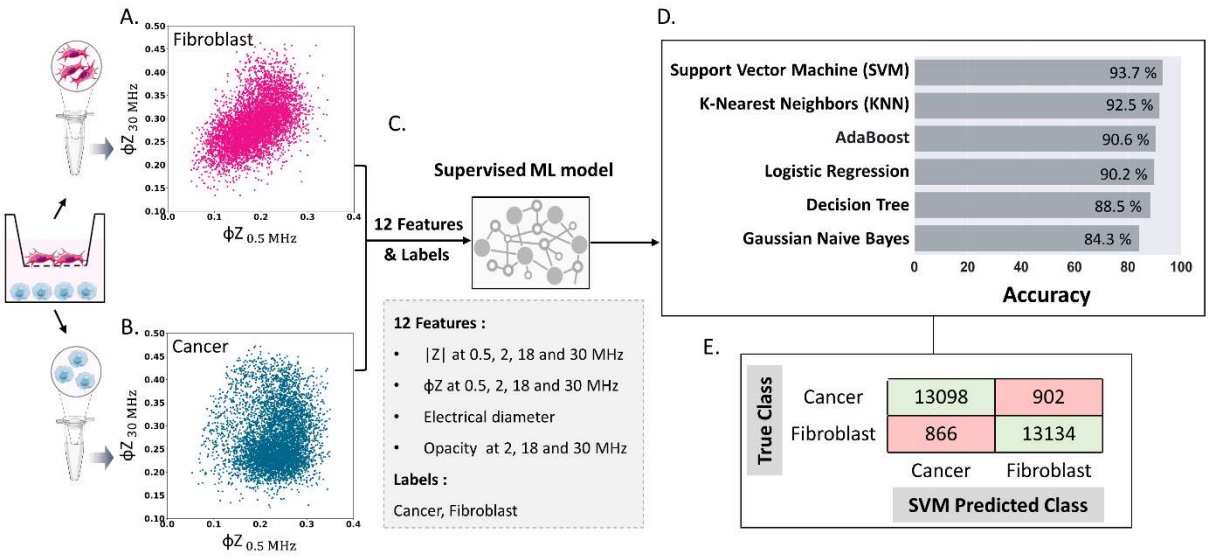

Figure 4.7: *The impedance data set obtained from homogeneous samples after transwell co-culture (14000 data points per cell type from 4 different transwell plate) for CAFs (A) and cancer cells (B) is used to train a supervised ML model based on 12 impedance features and two labels (C). The classification accuracy of different ML models is determined (D), so that the SVM model with the highest accuracy can be used to construct a confusion matrix to assess how well this optimal model accurately classifies data.*

Validation of the trained model was performed on heterogeneous samples generated by mixing the cancer cells and CAFs with differing ratios (cancer cells at 70% down to 5%). The impedance data from these heterogeneous samples (**Figure 4.8A.i-v**) is classified by the SVM model (**Figure 4.8B.i-v**) and assessed by flow cytometry after EpCAM staining (**Figure 4.8C.i-v**). The label-free classification by the SVM model (**Figure 4.8B** closely corresponds with those after EpCAM staining (**Figure 4.8C**) over the entire measured range of cancer cell proportions.

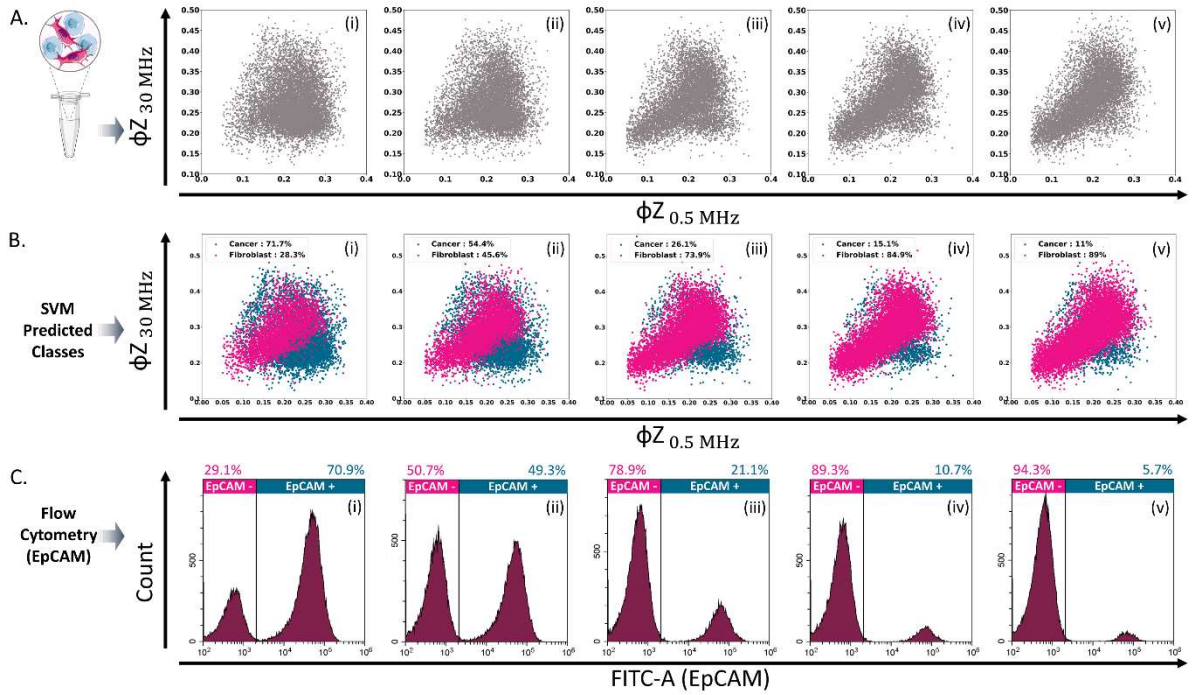

Figure 4.8: *Assessing classification of impedance data clusters from heterogeneous samples with varying proportions of cancer cells (70% to 5%) to CAFs. A. Scatter plots of* $\phi Z_{30\,MHz}$ *versus* $\phi Z_{0.5\,MHz}$ *are classified by: B. SVM predicted classes; and C. Flow cytometry analysis after EpCAM staining.*

While there are some deviations of the classification from SVM predictions versus from EpCAM staining are apparent at the lowest cancer cell proportion, we need to recognize the possible errors from EpCAM staining of heterogeneous samples, as shown in **Figure 4.9**. For instance, there is a proportion of cancer cells that is often not classified as EpCAM positive, as apparent from misclassification of a homogeneous cancer sample (100% cancer cells) as 93% cancer cells (**Figure 4.9A**). Similarly, the same gate can cause inaccuracies in thresholding that lead to a homogeneous fibroblast sample (100% CAFs) as 96.5% cancer cells (**Figure 4.9B**), with some of the CAFs picking up some of the EpCAM staining.

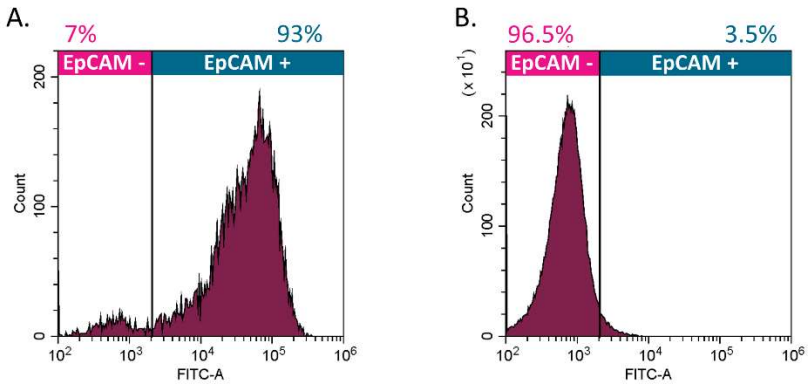

Figure 4.9: *Inaccuracies during flow cytometry to classify homogeneous samples of: A. cancer cells; B. CAFs, wherein the determined proportions are less than 100%.*

Supervised learning to distinguish drug-treated multicellular tumors of cancer cells and CAFs based on impedance metrics

The application of the supervised machine learning model approach was explored for classifying the remaining viable cancer cells after drug treatment of heterogeneous samples that includes CAFs, so that the drug resistant subpopulation can be accurately quantified based on biophysical properties without the need to stain the samples. **Figure 4.10** shows alteration in biophysical properties of CAFs after gemcitabine treatment (1 µg/mL for 48 hours). So, after gemcitabine treatment, impedance metrics of both cancer cells and CAFs will change. Hence, we need to train supervised models based on treated samples of cancer cells and CAFs.

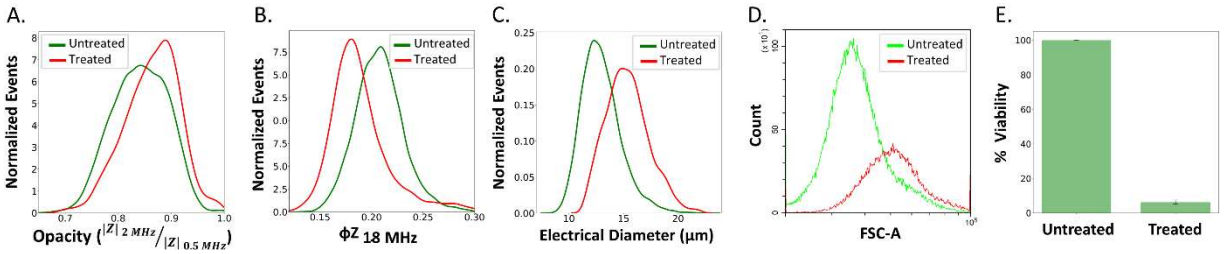

Figure 4.10: *The biophysical properties of untreated CAFs versus remaining viable CAFs after gemcitabine treatment (1 µg/mL for 48 hours) (A-C), with the electrical diameter validated based on forward scattering cytometry (FSC) (D), viability of CAFs after gemcitabine treatment (1 µg/mL for 48 hours) (E).*

The supervised machine learning approach is along similar lines as used for the untreated sample, with the drug treated sample in the transwell co-culture system separated for impedance

analysis of CAFs (**Figure 4.11A**) and cancer cells (**Figure 4.11B**). The remaining viable cells are gated based on procedures outlined in **Figure 4.2**, so that 12 impedance metrics (**Figure 4.11C**) can be used to train various supervised ML models (**Figure 4.11D**) for recognizing viable cancer cells and CAFs from within heterogeneous samples. Among different models, the (SVM) achieved the highest accuracy in predicting the cell types (94.3%). The high accuracy of the SVM algorithm can be confirmed by analyzing its confusion matrix (**Figure 4.11E**).

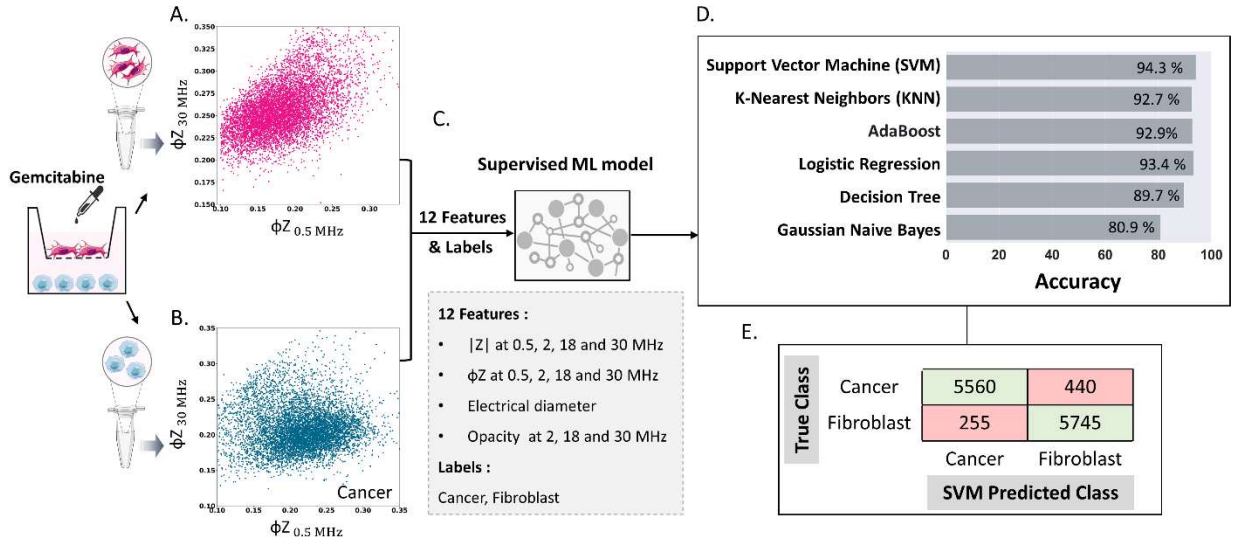

Figure 4.11: *Impedance cytometry data from drug-treated CAFs (A) and cancer cells (B) after transwell co-culture are used over 12 metrics (C) to train a supervised ML model that can distinguish the remaining viable cells of each type in a multicellular tumor after drug treatment. Based on results from various tested ML models (D), the SVM model the highest accuracy is used to construct the confusion matrix (E).*

The remaining viable population of CAFs after gemcitabine treatment (1 µg/mL for 48 hours), express higher level of EpCAM compared to untreated CAFs (**Figure 4.12Aii and Figure 4.12Bii**). So, it is not easy to classify the cancer vs CAFs with high precision by flow cytometry after gemcitabine treatment. Hence to validate the trained SVM model, we used synthetic heterogeneous drug-treated samples that are generated based on new data set from treated transwell co-culture.

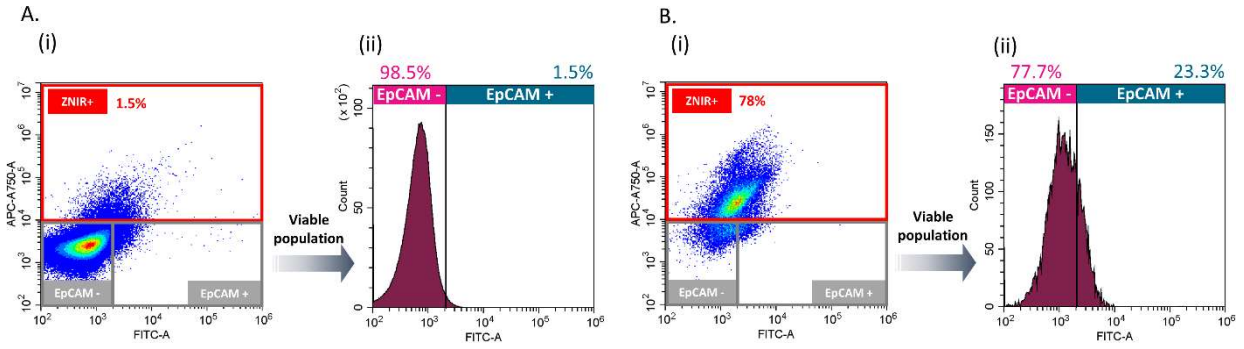

Figure 4.12: *Flow cytometry density scatter plots of EpCAM versus Zombie Near-Infrared (ZNIR) for: A(i) untreated CAFs and B(i) gemcitabine treated CAFs (1 µg/mL for 48 h). Histogram EpCAM on remaining viable population of CAFs: A(ii) before and B(ii) after treatment, show that viable treated CAFs express higher level of EpCAM compared to untreated samples.*

Following gemcitabine treatment, a great majority of CAFs are affected by the drug within a heterogeneous sample, leading to typical CAF viability in the 10% range (**Figure 4.10E**), while cancer cells exhibit high levels of viability due to emerging drug resistance. Hence, the synthetic heterogeneous drug-treated samples are generated by gating the viable subpopulations within drug-treated transwell samples and merging the data to have high proportions of cancer cells (68% in **Figure 4.13A** and 85% in **Figure 4.13B**), CAFs constituting the rest. These samples are used to validate the ability of the trained SVM model to classify the viable subpopulation as either cancer cells or CAFs (**Figure 4.13A.ii** and **Figure 4.B.ii**), with the biophysical quantification assessed by the confusion matrix (**Figure 4.13A.iii** and **Figure 4.13B.iii**). Based on this, it is apparent that the trained SVM model can predict the respective classes to high accuracy (95%), based on 66.5% cancer cells and 33.5% CAFs in **Figure 4.13A.iii** and 81.4% cancer cells and 18.6% CAFs in **Figure 4.13B.iii**.

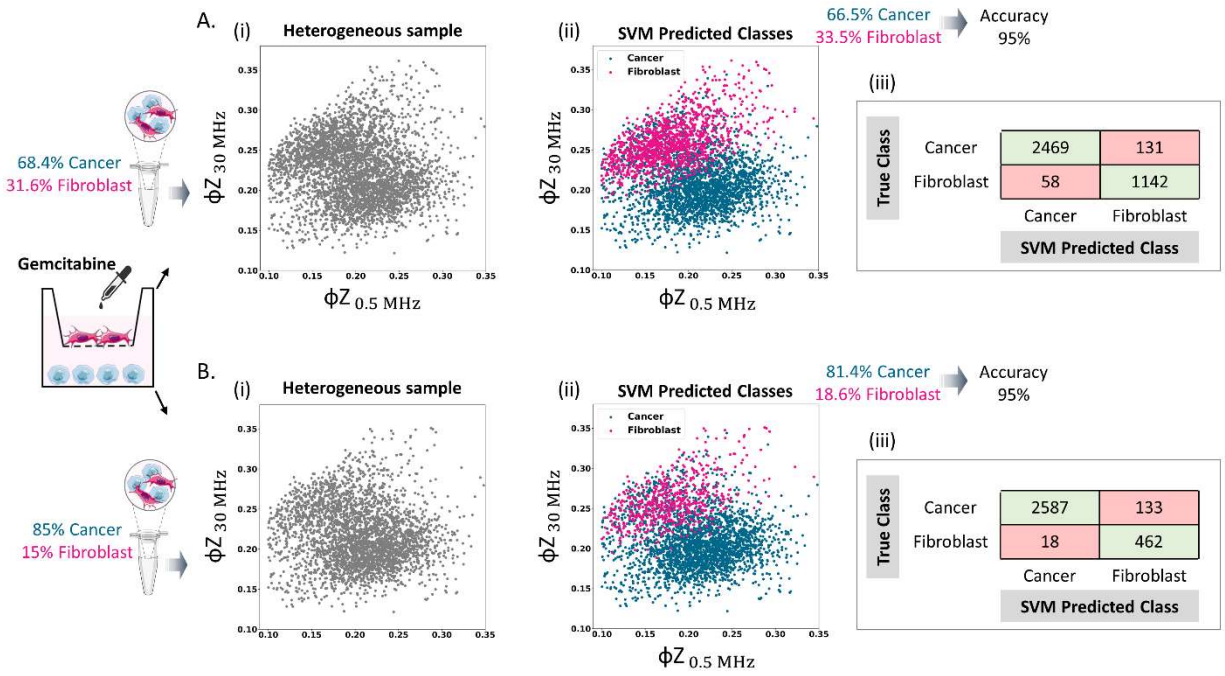

Figure 4.13: *Application of the SVM model to heterogeneous drug-treated samples with varying proportions of cancer cells to CAFs (A.i and B.i) to classify the viable subpopulation as either cancer cells or CAFs (A.ii & B.ii), with the confusion matrix of SVM (A.iii & B.iiii).*

CONCLUSIONS

Pancreatic cancer cells (T608) under drug treatment (1 μg/mL for 48 h) show a steep drop in viability down to 50% levels in monocultures but exhibit increasing proportions of viable cells (>85%) that remain under drug treatment within transwell and direct co-cultures with CAFs. Since label-free cell phenotypic monitoring is needed within longitudinal studies on drug treatment with patient derived tumors to identify the drug resistant subpopulation, we explore the application of impedance cytometry that can quantify biophysical properties with single-cell sensitivity at high throughput. We show that the viable cancer cells after drug treatment within co-cultures with CAFs exhibit systematic biophysical differences in cell size, membrane capacitance and interior cytoplasmic conductivity versus viable cancer cells in monoculture before drug treatment, but exhibit biophysical similarities to viable cancer cells in co-culture with CAFs in absence of drug treatment. Hence, we explore the application of impedance metrics in conjunction with supervised ML models to identify viable cancer cells versus viable CAFs in heterogeneous multicellular tumor samples for quantifying the drug resistant subpopulation, by training the model using transwell co-cultures of the respective cell types. The support vector machine (SVM) model shows the highest

level of accuracy, as validated by flow cytometry analysis after EpCAM staining for heterogeneous samples with varying proportions of cancer cells (70% to 5%) in transwell co-culture with CAFs in absence of gemcitabine. Similarly, in the presence of gemcitabine, the SVM model is able to classify viable cancer cells versus CAFs, as validated using synthetic heterogeneous mixtures of the respective cell types to determine the confusion matrix. We envision that these characteristic biophysical properties of remaining cancer cells after drug treatment can be used to quantify the drug resistant subpopulation within longitudinal studies and isolate them for downstream molecular analysis.

Future work

Chapter 1

In Chapter 1 of the dissertation, standard particles based on modified RBCs were developed and used to enable the mapping of measured phenomenological properties (impedance metrics of magnitude and phase) of unknown RBC phenotypes to their biophysical properties (membrane capacitance and cytoplasmic conductivity), without the need for extensive fitting of the data to dielectric shell models that involve several fitting parameters. This type of mapping would enable more reliable inline distinction of the unknown RBC phenotypes from each other based on their characteristic biophysical properties, as well as enable their dielectrophoretic separation based on the computed crossover frequency from their biophysical dispersion. This will be applied to distinction and separation of diseased RBCs, such as for sickle cell diseased RBCs, to benchmark intrapatient and interpatient variations in sickle cell disease [114]. Another application is to extend this mapping to cells that may differ in size and shape versus RBCs. For instance, size alterations would alter impedance metrics (phase, and opacity) per **Figure 5.1**, thereby requiring a method to normalize impedance metrics (opacity and phase) based on cell size. Size normalization would, for instance, allow us to distinguish the biophysical properties of unknown modifications to macrophages and cancer cells to enable their separation from a heterogeneous mixture.

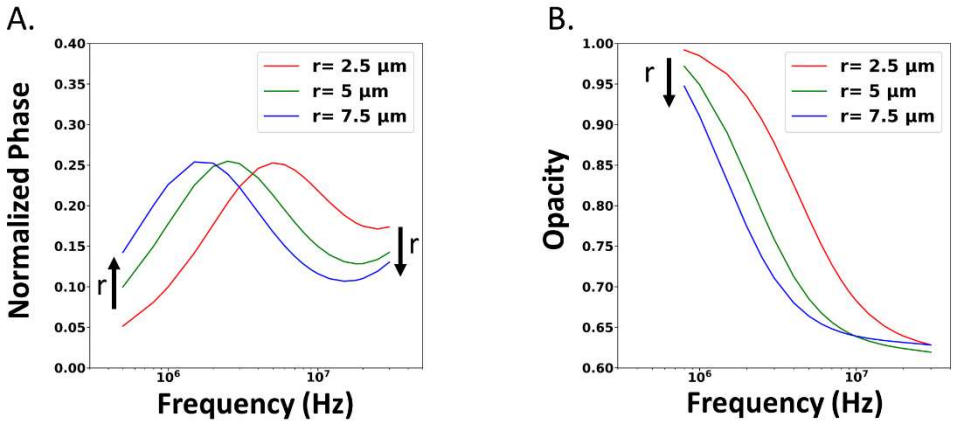

Figure 5.1: *Modelled impedance phase (ϕZ) and opacity for alteration to cell size (r_{cell} from 2.5 to 7.5 µm)*

Chapter 2

In Chapter 2, we presented the ability to use unsupervised learning for data clustering and supervised learning for data classification into phenotypes over the progression of apoptosis, from viable to early to late apoptosis and onward to secondary necrosis. In future work, we seek to apply this towards apoptotic bodies (ABs) secreted from pancreatic cancer cells under drug treatment. Specifically, based on a recently published article from our group [26] we suggest that the temporal profile of secreted from the culture can serve as a marker for drug sensitivity and be used to detect the emergence of drug resistance. In this work, we analyzed ABs secreted by 608 cancer cells under monoculture after gemcitabine treatment (1µg/ml, 48 h) using impedance cytometry. While drug sensitivity can be predicted based on the rise in numbers of ABs in the culture media below a size cut-off (< 5 µm), the shape of the ABs within distinct size ranges can be stratified based on their impedance phase levels using multi-shell dielectric models. By fitting the high frequency impedance phase distribution to three distinct AB subtypes, we infer that the events at low impedance phase levels (<0.3) obtained from < 2.6 µm particles can be attributed to spherical-shaped particles and the events at high impedance phase levels (>0.5) obtained from > 2.6 µm particles can be attributed to oblate-shaped particles, while the third subpopulation of low impedance phase levels (<0.3) obtained from the broadly sized particle events > 2.6 µm is attributed to arise from spherical and prolate-shaped particles (**Figure 5.2**)

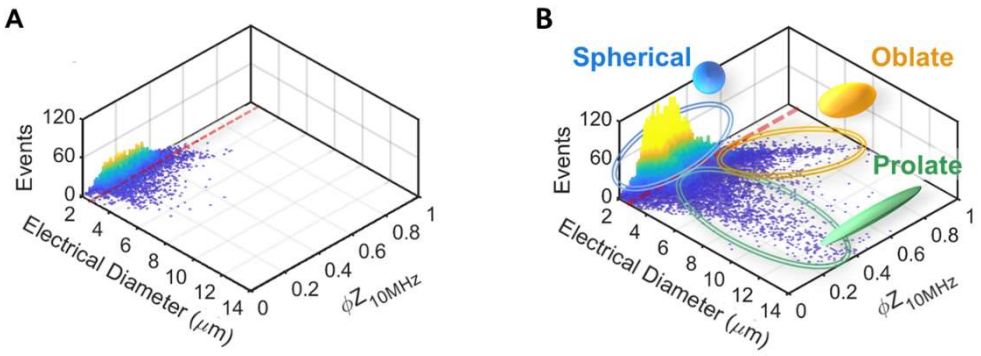

Figure 5.2: *Impedance cytometry of culture media supernatants from the T608 PDAC cell line. Density 3D distributions of electrical diameter versus impedance phase at 10 MHz ($\phi Z_{10\ MHz}$) for A. untreated and B. 1 µg/mL gemcitabine treated.*

This prior work was done at one drug concentration and one timepoint that was optimized to ensure apoptosis (1µg/ml, 48 h), but it is of interest to correlate the temporal profile of these ABs

to the onset of apoptosis based on the numbers of ABs of various sizes, shapes and composition. To accomplish this, future work can involve training of a supervised model, so automated clustering and classification of each AB type can occur. We will vary the dose and duration of drug treatment for the drug sensitive T608 cells and drug resistant T366 cells. Also, we will explore serially increasing the gemcitabine concentration, while periodically removing the floating dead cells from the culture, so that drug resistant subpopulations can be created over extended culture periods (>1 month). The temporal profile of the secreted ABs will be studied to identify the hallmarks associated with the emergence of drug resistant phenotypes.

Chapter 3

In Chapter 3, we showed that the drug sensitive T608 cancer cells gradually become less sensitive or resistant to gemcitabine in the presence of cancer associated fibroblasts (CAFs) that are used to simulate the multicellular tumor microenvironment. In future work, we would like to perform this experiment within 3D co-culture systems with differing levels of CAFs in the culture. To simulate the tumor microenvironment, the level of hypoxia in the culture will be varied (20% O_2 down to 0.1%) to study alterations in drug sensitivity. Additionally, using GFP expressing cancer cells that lose fluorescence under drug-induced apoptosis, live-cell imaging within the incubator jacket will be correlated to the cytometry profile of secreted apoptotic bodies. In this manner, the interaction of cancer and CAFs, as well as its relationship to drug sensitivity alterations will be explored.

Publications

Publications associated with work done during pursuit of degree

1. *"Supervised learning on impedance cytometry data for distinction of pancreatic cancer versus associated fibroblast cells",*

   Armita Salahi, Carlos Honrado, Sara J. Adair, John H. Moore, Todd W. Bauer, Nathan S. Swami, (ready to submit)

2. *"Automated biophysical classification of apoptotic pancreatic cancer cell subpopulations using machine learning"*

   Carlos Honrado, **Armita Salahi**, Sara J. Adair, John H. Moore, Todd W. Bauer, Nathan S. Swami. Small, 2022 (Submitted)

3. *"Single-cell assessment of the modulation of macrophage activation by ex vivo intervertebral discs using impedance cytometry"*

   Armita Salahi, Aditya Rane, Li Xiao, Carlos Honrado, Xudong Li, Li Jin, Nathan S. Swami. Biosensors and Bioelectronics, 2022 (Submitted)

4. *"Modified Red Blood Cells as Multimodal Standards for Benchmarking Single-Cell Cytometry and Separation Based on Electrical Physiology"*

   Armita Salahi, Carlos Honrado, Aditya Rane, Federica Caselli, Nathan S Swami. Analytical Chemistry, 2022

5. *"Apoptotic Bodies in the Pancreatic Tumor Cell Culture Media Enable Label-Free Drug Sensitivity Assessment by Impedance Cytometry"*

   Carlos Honrado, Sara J Adair, John H Moore, **Armita Salahi**, Todd W Bauer, Nathan S Swami. Advanced Biology, 2021

6. *"Self-aligned sequential lateral field non-uniformities over channel depth for high throughput dielectrophoretic cell deflection"*

   XuHai Huang, Karina Torres-Castro, Walter Varhue, **Armita Salahi**, Ahmed Rasin, Carlos Honrado, Audrey Brown, Jennifer Guler, Nathan S Swami. Lab on a Chip, 2021

7. *"Label-free quantification of cell cycle synchronicity of human neural progenitor cells based on electrophysiology phenotypes"*

   Carlos Honrado, Nadine Michel, John H Moore, **Armita Salahi**, Veronica Porterfield, Michael J McConnell, Nathan S Swami. ACS sensors, 2020

8. *"Quantifying bacterial spore germination by single-cell impedance cytometry for assessment of host microbiota susceptibility to Clostridioides difficile infection"*

John H Moore, **Armita Salahi**, Carlos Honrado, Christopher Warburton, Cirle A Warren, Nathan S Swami. Biosensors and Bioelectronics, 2020

9. *"Self-aligned microfluidic contactless dielectrophoresis device fabricated by single-layer imprinting on cyclic olefin copolymer"*

   Armita Salahi, Walter B Varhue, Vahid Farmehini, Alexandra R Hyler, Eva M Schmelz, Rafael V Davalos, Nathan S Swami. Analytical and bioanalytical chemistry, 2020

10. *"Electrophysiology-based stratification of pancreatic tumorigenicity by label-free single-cell impedance cytometry"*

    John S McGrath, Carlos Honrado, John H Moore, Sara J Adair, Walter B Varhue, **Armita Salahi**, Vahid Farmehini, Bernadette J Goudreau, Sarbajeet Nagdas, Edik Blais, Todd W Bauer, Nathan S Swami. Analytica chimica acta, 2020

11. *"On-chip impedance for quantifying parasitic voltages during AC electrokinetic trapping"*

    Vahid Farmehini, Walter Varhue, **Armita Salahi**, Alexandra R Hyler, Jaka Čemažar, Rafael V Davalos, Nathan S Swami. IEEE Transactions on Biomedical Engineering, 2019

12. *"Crystallization of high aspect ratio HKUST-1 thin films in nanoconfined channels for selective small molecule uptake"*

    Stephanie Guthrie, Luke Huelsenbeck, **Armita Salahi**, Walter Varhue, Natalie Smith, Xiaohan Yu, Lucy U Yoon, Joshua J Choi, Nathan Swami, Gaurav Giri. Nanoscale Advances, 2019

13. *"Frequency-selective electrokinetic enrichment of biomolecules in physiological media based on electrical double-layer polarization"*

    Ali Rohani, Bankim J Sanghavi, **Armita Salahi**, Kuo-Tang Liao, Chia-Fu Chou, Nathan S Swami. Nanoscale, 2017

Selected Conferences

- MicroTas 2021: *"Supervised learning on impedance cytometry data for drug sensitivity distinction of cancer versus fibroblast cells"*
- MicroTas 2021: *"Drug-induced modulation of macrophage activation by ex vivo herniated discs measured by impedance cytometry"*
- MicroTas 2020: *"Red blood cells as model particles with modulated subcellular electrophysiology for impedance cytometry"*

- AES 2018: *"Single-shot microfabrication of multilayer aligned contactless dielectrophoresis devices by imprinting"*

Patents and Awards

- US Application Patent: *AUTOMATED CLASSIFICATION OF BIOLOGICAL SUBPOPULATIONS USING IMPEDANCE PARAMETERS*
- US Application Patent: *SYSTEM AND METHOD FOR MODIFIED RED BLOOD CELLS AS MULTIMODAL STANDARDS FOR BENCHMARKING SINGLE-CELL CYTOMETRY AND SEPARATION*
- US Application Patent: *BACTERIAL SPORE GERMINATION ASSAY OF MICROBIOTA DISRUPTION*
- Virginia Cancer Center Fellowship (2021)
- Sture G. Olsson Fellowship in Engineering (2020)

Bibliography

1. Morgan, H. and N.G. Green, *AC electrokinetics: colloids and nanoparticles*. 2003: Research Studies Press.
2. Maxwell, J.C., *A Treatise on Electricity and Magnetism: Vol. 1 (1881)*. 2008: Clarendon Press.
3. Hanai, T., N. Koizumi, and A. Irimajiri, *A method for determining the dielectric constant and the conductivity of membrane-bounded particles of biological relevance.* Biophysics of structure and mechanism, 1975. **1**(4): p. 285-294.
4. Huang, Y., et al., *Differences in the AC electrodynamics of viable and non-viable yeast cells determined through combined dielectrophoresis and electrorotation studies.* Physics in Medicine & Biology, 1992. **37**(7): p. 1499.
5. Irimajiri, A., T. Hanai, and A. Inouye, *A dielectric theory of "multi-stratified shell" model with its application to a lymphoma cell.* Journal of theoretical biology, 1979. **78**(2): p. 251-269.
6. Spencer, D. and H. Morgan, *High-speed single-cell dielectric spectroscopy.* ACS sensors, 2020. **5**(2): p. 423-430.
7. Pohl, H.A., *The motion and precipitation of suspensoids in divergent electric fields.* Journal of applied Physics, 1951. **22**(7): p. 869-871.
8. Pethig, R., *Dielectrophoresis: Status of the theory, technology, and applications.* Biomicrofluidics, 2010. **4**(2): p. 022811.
9. Morgan, H., et al., *Single cell dielectric spectroscopy.* Journal of Physics D: Applied Physics, 2006. **40**(1): p. 61.
10. Perkins, T.J. and P.S. Swain, *Strategies for cellular decision-making.* Mol Syst Biol, 2009. **5**: p. 326.
11. Kleparnik, K. and F. Foret, *Recent advances in the development of single cell analysis--a review.* Anal Chim Acta, 2013. **800**: p. 12-21.
12. Cros, J., et al., *Tumor Heterogeneity in Pancreatic Adenocarcinoma.* Pathobiology, 2018. **85**(1-2): p. 64-71.
13. Cossarizza, A., et al., *Guidelines for the use of flow cytometry and cell sorting in immunological studies.* European journal of immunology, 2019. **49**(10): p. 1457-1973.
14. Wlodkowic, D., J. Skommer, and Z. Darzynkiewicz, *Cytometry in cell necrobiology revisited. Recent advances and new vistas.* Cytometry Part A, 2010. **77**(7): p. 591-606.
15. Cheung, K.C., et al., *Microfluidic impedance-based flow cytometry.* Cytometry Part A, 2010. **77**(7): p. 648-666.
16. Sun, T. and H. Morgan, *Single-cell microfluidic impedance cytometry: a review.* Microfluidics and Nanofluidics, 2010. **8**(4): p. 423-443.

17. Fernandez, R.E., et al., *Microbial analysis in dielectrophoretic microfluidic systems.* Analytica chimica acta, 2017. **966**: p. 11-33.
18. Honrado, C., et al., *Single-cell microfluidic impedance cytometry: from raw signals to cell phenotypes using data analytics.* Lab on a Chip, 2021. **21**(1): p. 22-54.
19. Honrado, C., et al., *Label-Free Quantification of Cell Cycle Synchronicity of Human Neural Progenitor Cells Based on Electrophysiology Phenotypes.* Acs Sensors, 2020. **6**(1): p. 156-165.
20. Honrado, C., et al., *Dielectric characterization of Plasmodium falciparum-infected red blood cells using microfluidic impedance cytometry.* Journal of The Royal Society Interface, 2018. **15**(147): p. 20180416.
21. Petchakup, C., et al., *Label-free leukocyte sorting and impedance-based profiling for diabetes testing.* Biosensors and Bioelectronics, 2018. **118**: p. 195-203.
22. Petchakup, C., et al., *Label-free quantitative lymphocyte activation profiling using microfluidic impedance cytometry.* Sensors and Actuators B: Chemical, 2021. **339**: p. 129864.
23. McGrath, J., et al., *Electrophysiology-based stratification of pancreatic tumorigenicity by label-free single-cell impedance cytometry.* Analytica chimica acta, 2020. **1101**: p. 90-98.
24. De Ninno, A., et al., *High-throughput label-free characterization of viable, necrotic and apoptotic human lymphoma cells in a coplanar-electrode microfluidic impedance chip.* Biosensors and Bioelectronics, 2020. **150**: p. 111887.
25. Moore, J.H., et al., *Quantifying bacterial spore germination by single-cell impedance cytometry for assessment of host microbiota susceptibility to Clostridioides difficile infection.* Biosensors and Bioelectronics, 2020. **166**: p. 112440.
26. Honrado, C., et al., *Apoptotic Bodies in the Pancreatic Tumor Cell Culture Media Enable Label-Free Drug Sensitivity Assessment by Impedance Cytometry.* Advanced Biology, 2021: p. 2100438.
27. Gong, L., et al., *Direct and Label-Free Cell Status Monitoring of Spheroids and Microcarriers Using Microfluidic Impedance Cytometry.* Small, 2021: p. 2007500.
28. Huang, X., et al., *Self-aligned sequential lateral field non-uniformities over channel depth for high throughput dielectrophoretic cell deflection.* Lab on a Chip, 2021. **21**(5): p. 835-843.
29. Gascoyne, P.R. and S. Shim, *Isolation of circulating tumor cells by dielectrophoresis.* Cancers, 2014. **6**(1): p. 545-579.
30. Li, M. and R.K. Anand, *High-throughput selective capture of single circulating tumor cells by dielectrophoresis at a wireless electrode array.* Journal of the American Chemical Society, 2017. **139**(26): p. 8950-8959.

31. Adams, T.N., et al., *Label-free enrichment of fate-biased human neural stem and progenitor cells.* Biosensors and Bioelectronics, 2020. **152**: p. 111982.
32. Rohani, A., et al., *Label-free quantification of intracellular mitochondrial dynamics using dielectrophoresis.* Analytical chemistry, 2017. **89**(11): p. 5757-5764.
33. Su, Y.-H., et al., *Dielectrophoretic monitoring and interstrain separation of intact Clostridium difficile based on their S (Surface)-layers.* Analytical chemistry, 2014. **86**(21): p. 10855-10863.
34. Liu, Y. and M.A. Hayes, *Differential Biophysical Behaviors of Closely Related Strains of Salmonella.* Frontiers in microbiology, 2020. **11**: p. 302.
35. Shi, L., et al., *Rapid and label-free isolation of small extracellular vesicles from biofluids utilizing a novel insulator based dielectrophoretic device.* Lab on a Chip, 2019. **19**(21): p. 3726-3734.
36. Moore, J.H., et al., *Conductance-based biophysical distinction and microfluidic enrichment of nanovesicles derived from pancreatic tumor cells of varying invasiveness.* Analytical chemistry, 2019. **91**(16): p. 10424-10431.
37. Gawad, S., L. Schild, and P. Renaud, *Micromachined impedance spectroscopy flow cytometer for cell analysis and particle sizing.* Lab on a Chip, 2001. **1**(1): p. 76-82.
38. Haandbæk, N., et al., *Characterization of single yeast cell phenotypes using microfluidic impedance cytometry and optical imaging.* Acs Sensors, 2016. **1**(8): p. 1020-1027.
39. Patel, S., et al., *Microfluidic separation of live and dead yeast cells using reservoir-based dielectrophoresis.* Biomicrofluidics, 2012. **6**(3): p. 034102.
40. Hansen, C.E. and W.A. Lam, *Clinical implications of single-cell microfluidic devices for hematological disorders*. 2017, ACS Publications.
41. Liu, J., et al., *Electrical impedance characterization of erythrocyte response to cyclic hypoxia in sickle cell disease.* ACS sensors, 2019. **4**(7): p. 1783-1790.
42. Levy, E., et al., *Dielectric response of cytoplasmic water and its connection to the vitality of human red blood cells: I. Glucose concentration influence.* The Journal of Physical Chemistry B, 2016. **120**(39): p. 10214-10220.
43. Gordon, J.E., Z. Gagnon, and H.-C. Chang, *Dielectrophoretic discrimination of bovine red blood cell starvation age by buffer selection and membrane cross-linking.* Biomicrofluidics, 2007. **1**(4): p. 044102.
44. Gagnon, Z., et al., *Bovine red blood cell starvation age discrimination through a glutaraldehyde-amplified dielectrophoretic approach with buffer selection and membrane cross-linking.* Electrophoresis, 2008. **29**(11): p. 2272-2279.

45. Qiang, Y., et al., *In vitro assay for single-cell characterization of impaired deformability in red blood cells under recurrent episodes of hypoxia.* Lab on a Chip, 2021.
46. Milani, K.J., T.G. Schneider, and T.F. Taraschi, *Defining the morphology and mechanism of the hemoglobin transport pathway in Plasmodium falciparum-infected erythrocytes.* Eukaryotic cell, 2015. **14**(4): p. 415-426.
47. Tomaiuolo, G., *Biomechanical properties of red blood cells in health and disease towards microfluidics.* Biomicrofluidics, 2014. **8**(5): p. 051501.
48. Lee, K.C., et al., *Toward deep biophysical cytometry: prospects and challenges.* Trends in Biotechnology, 2021.
49. Wu, P.-H., et al., *A comparison of methods to assess cell mechanical properties.* Nature methods, 2018. **15**: p. 491-498.
50. Girardo, S., et al., *Standardized microgel beads as elastic cell mechanical probes.* Journal of Materials Chemistry B, 2018. **6**(39): p. 6245-6261.
51. Doberstein, S.K., et al., *Fluorescent erythrocyte ghosts as standards for quantitative flow cytometry.* Cytometry, 1995. **20**(1): p. 14-8.
52. Cheung, K., S. Gawad, and P. Renaud, *Impedance spectroscopy flow cytometry: On-chip label-free cell differentiation.* Cytometry Part A, 2005. **65**(2): p. 124-132.
53. Carlos, H., et al., *A neural network approach for real-time particle/cell characterization in microfluidic impedance cytometry.* Analytical and bioanalytical chemistry, 2020. **412**(16): p. 3835-3845.
54. Dong, X., et al., *Formulation and drug loading features of nano-erythrocytes.* Nanoscale research letters, 2017. **12**(1): p. 1-13.
55. Abay, A., et al., *Glutaraldehyde–a subtle tool in the investigation of healthy and pathologic red blood cells.* Frontiers in physiology, 2019. **10**: p. 514.
56. Cottet, J., et al., *MyDEP: a new computational tool for dielectric modeling of particles and cells.* Biophysical journal, 2019. **116**(1): p. 12-18.
57. Salmanzadeh, A., et al., *Sphingolipid metabolites modulate dielectric characteristics of cells in a mouse ovarian cancer progression model.* Integr Biol (Camb), 2013. **5**(6): p. 843-52.
58. Chan, K.L., et al., *Electrorotation of liposomes: verification of dielectric multi-shell model for cells.* Biochim Biophys Acta, 1997. **1349**(2): p. 182-96.
59. Elmore, S., *Apoptosis: a review of programmed cell death.* Toxicologic pathology, 2007. **35**(4): p. 495-516.

60. Bergsmedh, A., et al., *Horizontal transfer of oncogenes by uptake of apoptotic bodies.* Proceedings of the National Academy of Sciences, 2001. **98**(11): p. 6407-6411.
61. Poon, I.K., et al., *Apoptotic cell clearance: basic biology and therapeutic potential.* Nature Reviews Immunology, 2014. **14**(3): p. 166-180.
62. Méry, B., et al., *In vitro cell death determination for drug discovery: A landscape review of real issues.* Journal of cell death, 2017. **10**: p. 1179670717691251.
63. Samm, N., et al., *The role of apoptosis in the pathology of pancreatic cancer.* Cancers, 2011. **3**(1): p. 1-16.
64. Rahib, L., et al., *Projecting cancer incidence and deaths to 2030: the unexpected burden of thyroid, liver, and pancreas cancers in the United States.* Cancer research, 2014. **74**(11): p. 2913-2921.
65. Herman, J.M., et al., *Analysis of fluorouracil-based adjuvant chemotherapy and radiation after pancreaticoduodenectomy for ductal adenocarcinoma of the pancreas: results of a large, prospectively collected database at the Johns Hopkins Hospital.* Journal of clinical oncology: official journal of the American Society of Clinical Oncology, 2008. **26**(21): p. 3503.
66. Neoptolemos, J.P., et al., *A randomized trial of chemoradiotherapy and chemotherapy after resection of pancreatic cancer.* New England Journal of Medicine, 2004. **350**(12): p. 1200-1210.
67. Jemal, A., et al., *Cancer statistics, 2009.* CA Cancer J Clin, 2009. **59**(4): p. 225-49.
68. Amrutkar, M. and I.P. Gladhaug, *Pancreatic cancer chemoresistance to gemcitabine.* Cancers, 2017. **9**(11): p. 157.
69. Thomas, D. and P. Radhakrishnan, *Tumor-stromal crosstalk in pancreatic cancer and tissue fibrosis.* Molecular cancer, 2019. **18**(1): p. 1-15.
70. Wilding, J.L. and W.F. Bodmer, *Cancer cell lines for drug discovery and development.* Cancer Res, 2014. **74**(9): p. 2377-84.
71. Kopetz, S., R. Lemos, and G. Powis, *The promise of patient-derived xenografts: the best laid plans of mice and men.* Clin Cancer Res, 2012. **18**(19): p. 5160-2.
72. Plenge, R.M., E.M. Scolnick, and D. Altshuler, *Validating therapeutic targets through human genetics.* Nat Rev Drug Discov, 2013. **12**(8): p. 581-94.
73. Friedman, A.A., et al., *Precision medicine for cancer with next-generation functional diagnostics.* Nature Reviews Cancer, 2015. **15**(12): p. 747-756.
74. Cotter, T.G., *Apoptosis and cancer: the genesis of a research field.* Nature Reviews Cancer, 2009. **9**(7): p. 501-507.

75. Carneiro, B.A. and W.S. El-Deiry, *Targeting apoptosis in cancer therapy.* Nature reviews Clinical oncology, 2020. **17**(7): p. 395-417.
76. Van Cruchten, S. and W. Van Den Broeck, *Morphological and biochemical aspects of apoptosis, oncosis and necrosis.* Anatomia, histologia, embryologia, 2002. **31**(4): p. 214-223.
77. Castedo, M., et al., *Cell death by mitotic catastrophe: a molecular definition.* Oncogene, 2004. **23**(16): p. 2825-2837.
78. Chen, X., et al., *Cell death in pancreatic cancer: From pathogenesis to therapy.* Nature Reviews Gastroenterology & Hepatology, 2021. **18**(11): p. 804-823.
79. Trauzold, A., et al., *CD95 and TRAIL receptor-mediated activation of protein kinase C and NF-κB contributes to apoptosis resistance in ductal pancreatic adenocarcinoma cells.* Oncogene, 2001. **20**(31): p. 4258-4269.
80. Weinlich, R., et al., *Necroptosis in development, inflammation and disease.* Nature reviews Molecular cell biology, 2017. **18**(2): p. 127-136.
81. Galluzzi, L., et al., *Necroptosis: mechanisms and relevance to disease.* Annual Review of Pathology: Mechanisms of Disease, 2017. **12**: p. 103-130.
82. Arumugam, T., et al., *Epithelial to mesenchymal transition contributes to drug resistance in pancreatic cancer.* Cancer research, 2009. **69**(14): p. 5820-5828.
83. AbuHammad, S. and M. Zihlif, *Gene expression alterations in doxorubicin resistant MCF7 breast cancer cell line.* Genomics, 2013. **101**(4): p. 213-220.
84. Puspita, N.A. and A. Bedford, *Morphological Changes of Cisplatin-resistant Human Breast Cancer MCF-7 Cell Line.* International Journal of Integrated Health Sciences, 2017. **5**(1): p. 8-14.
85. Pasqualato, A., et al., *Quantitative shape analysis of chemoresistant colon cancer cells: correlation between morphotype and phenotype.* Experimental Cell Research, 2012. **318**(7): p. 835-846.
86. Zhu, X., et al., *miR-186 regulation of Twist1 and ovarian cancer sensitivity to cisplatin.* Oncogene, 2016. **35**(3): p. 323-332.
87. Buscail, L., B. Bournet, and P. Cordelier, *Role of oncogenic KRAS in the diagnosis, prognosis and treatment of pancreatic cancer.* Nature Reviews Gastroenterology & Hepatology, 2020. **17**(3): p. 153-168.
88. Spencer, D.C., et al., *A fast impedance-based antimicrobial susceptibility test.* Nature communications, 2020. **11**(1): p. 1-11.

89. Schütt, J., et al., *Nanocytometer for smart analysis of peripheral blood and acute myeloid leukemia: a pilot study.* Nano Letters, 2020. **20**(9): p. 6572-6581.
90. Ahuja, K., et al., *Toward point-of-care assessment of patient response: a portable tool for rapidly assessing cancer drug efficacy using multifrequency impedance cytometry and supervised machine learning.* Microsystems & nanoengineering, 2019. **5**(1): p. 1-11.
91. D'Orazio, M., et al., *Electro-optical classification of pollen grains via microfluidics and machine learning.* IEEE Transactions on Biomedical Engineering, 2021.
92. Feng, Y., et al., *Neural network-enhanced real-time impedance flow cytometry for single-cell intrinsic characterization.* Lab on a Chip, 2022. **22**(2): p. 240-249.
93. Stokes, J.B., et al., *Inhibition of focal adhesion kinase by PF-562,271 inhibits the growth and metastasis of pancreatic cancer concomitant with altering the tumor microenvironment.* Molecular cancer therapeutics, 2011. **10**(11): p. 2135-2145.
94. Walters, D.M., et al., *Inhibition of the growth of patient-derived pancreatic cancer xenografts with the MEK inhibitor trametinib is augmented by combined treatment with the epidermal growth factor receptor/HER2 inhibitor lapatinib.* Neoplasia, 2013. **15**(2): p. 143-IN10.
95. Huang, P. and W. Plunkett. *Induction of apoptosis by gemcitabine*. in *Seminars in oncology*. 1995.
96. Van Engeland, M., et al., *Annexin V-affinity assay: a review on an apoptosis detection system based on phosphatidylserine exposure.* Cytometry: The Journal of the International Society for Analytical Cytology, 1998. **31**(1): p. 1-9.
97. Walker, N., et al., *Patterns of cell death.* Methods and achievements in experimental pathology, 1988. **13**: p. 18-54.
98. Fink, S.L. and B.T. Cookson, *Apoptosis, pyroptosis, and necrosis: mechanistic description of dead and dying eukaryotic cells.* Infection and immunity, 2005. **73**(4): p. 1907-1916.
99. Kerr, J.F., A.H. Wyllie, and A.R. Currie, *Apoptosis: a basic biological phenomenon with wideranging implications in tissue kinetics.* British journal of cancer, 1972. **26**(4): p. 239-257.
100. Atkin-Smith, G.K. and I.K. Poon, *Disassembly of the dying: mechanisms and functions.* Trends in cell biology, 2017. **27**(2): p. 151-162.
101. Silva, M.T., *Secondary necrosis: the natural outcome of the complete apoptotic program.* FEBS letters, 2010. **584**(22): p. 4491-4499.
102. Majno, G. and I. Joris, *Apoptosis, oncosis, and necrosis. An overview of cell death.* The American journal of pathology, 1995. **146**(1): p. 3.

103. Selzner, N., et al., *Water induces autocrine stimulation of tumor cell killing through ATP release and P2 receptor binding.* Cell Death & Differentiation, 2004. **11**(2): p. S172-S180.
104. Dauer, P., et al., *Microenvironment in determining chemo-resistance in pancreatic cancer: Neighborhood matters.* Pancreatology, 2017. **17**(1): p. 7-12.
105. Gioeli, D., et al., *Development of a multicellular pancreatic tumor microenvironment system using patient-derived tumor cells.* Lab on a Chip, 2019. **19**(7): p. 1193-1204.
106. Wu, M. and M.A. Swartz, *Modeling tumor microenvironments in vitro.* Journal of biomechanical engineering, 2014. **136**(2).
107. Villasante, A. and G. Vunjak-Novakovic, *Tissue-engineered models of human tumors for cancer research.* Expert opinion on drug discovery, 2015. **10**(3): p. 257-268.
108. Boj, S.F., et al., *Organoid models of human and mouse ductal pancreatic cancer.* Cell, 2015. **160**(1-2): p. 324-338.
109. Huang, L., et al., *Ductal pancreatic cancer modeling and drug screening using human pluripotent stem cell–and patient-derived tumor organoids.* Nature medicine, 2015. **21**(11): p. 1364-1371.
110. Hirschhaeuser, F., et al., *Multicellular tumor spheroids: an underestimated tool is catching up again.* Journal of biotechnology, 2010. **148**(1): p. 3-15.
111. Aldridge, S. and S.A. Teichmann, *Single cell transcriptomics comes of age.* Nature Communications, 2020. **11**(1): p. 1-4.
112. Richards, K.E., et al., *Cancer-associated fibroblast exosomes regulate survival and proliferation of pancreatic cancer cells.* Oncogene, 2017. **36**(13): p. 1770-1778.
113. Monteiro, M.V., et al., *Stratified 3D microtumors as organotypic testing platforms for screening pancreatic cancer therapies.* Small Methods, 2021. **5**(5): p. 2001207.
114. Dieujuste, D., Y. Qiang, and E. Du, *A portable impedance microflow cytometer for measuring cellular response to hypoxia.* Biotechnology and Bioengineering, 2021. **118**(10): p. 4041-4051.